CRANFIELD UNIVERSITY

Zeshan Malick

COMPUTATIONAL MODELLING OF CAVITY ARRAYS WITH HEAT TRANSFER USING IMPLICIT LARGE EDDY SIMULATIONS

SCHOOL OF ENGINEERING

PhD THESIS

CRANFIELD UNIVERSITY

SCHOOL OF ENGINEERING

PhD THESIS

November 2004 - January 2010

Zeshan Malick

Computational Modelling of Cavity Arrays with Heat Transfer using Implicit Large Eddy Simulations

Supervisors: Prof. Dimitris Drikakis and Dr. Evgeniy Shapiro

January 2010

This thesis is submitted in (100%) fulfilment of the requirements for the PhD

Abstract

This PhD programme was sponsored by the United Kingdom Atomic Energy Authority (UKAEA). The aim of this study is to conduct advanced computational modelling of a cooling device used in the fusion process which recycles waste energy.

The development of efficient, water cooled tiles, that can sustain heat loads of approximately 20 MW (in quasi-steady state conditions) is the motivation of the current work. The information presented here will contribute to thermal-mechanical analysis, to be conducted at the Joint European Torus (JET) in future years.

The devices known as "Hypervapotrons" have been used successfully at JET to provide a ion dump that dissipates residual energy from the fusion process. A capability to model the flow structure and heat transfer, across a large number of geometric and material options is provided within. Differences in geometry, result in changes to the flow structure and heat transfer rates. The desire to optimise such designs relies upon the fundamental understanding of the flow field within the main section, where the geometry may be defined as a cavity array.

The benchmark case of a lid driven cavity flow was used for the validation of the flow field solution. Solutions using high resolution methods in the formulation provided a good comparison with established experimental data. Therefore, validation of incompressible, Implicit Large Eddy Simulations (ILES) for a wall bounded, three dimensional, turbulent flow is provided within. The sensitivity of the high order reconstruction in conjunction with the characteristics based scheme (Drikakis & Rider,

2005), to resolve turbulent flow structure is provided here. The solution response to grid resolution and a regularised velocity profile at the upper lid surface is also detailed. The investigation provided insight and confidence in the turbulence modelling approach which is relatively recent. It was also demonstrated through the lid driven case (and later in the Hypervapotron cases) that high order reconstruction was a simulation prerequisite, based on grid resolutions used within. Additional validation was also provided against numerical and analytical solutions for the Conjugate Heat Transfer (CHT) and scalar temperature field. Where appropriate both unsteady and steady problems based on a composite, three layer medium are detailed to provide preliminary validation for the implementation of the temperature scalar and conjugate boundary conditions.

Unfortunately, it was not feasible to solve the coupled problem with an explicit solver as used in this study. However, it is suggested that the initial stages of thermal boundary layer development may be observed leading to the locations of incipient boiling.

Two different Reynolds numbers were considered for the Hypervapotron "Standard" geometry, Re=12000 and Re=18000. The different flow structures show that the cavity aspect ratio of the Standard design promotes lower flow speeds at the cavity base, since two or three counter rotating vortices coexist inside the cavities depending on Reynolds number. A detailed analysis on the impact of the number of repeating units within the computational domain is also provided. Results are presented of ensemble averaged quantities based on the Reynolds decomposition.

The temperature distribution present in the solid, fluid and its interface for the thermally developing case is achieved. In addition the total and decomposed heat fluxes are presented for the Hypervapotron (Standard design) which provides similar comparison with recent Reynolds Averaged Navier-Stokes (RANS) simulations.

Acknowledgements

I would like to thank the UKAEA for funding this PhD programme and accommodating me during my brief visit at the JET facility, Culham, Oxfordshire.

My sincere gratitude and thanks are extended to Professor Dimitris Drikakis and Dr Evgeniy Shapiro; whilst I have conducted this study I have been very fortunate to be in your company. I would like to thank Professor Drikakis (1st supervisor) for giving me the opportunity to complete a deep rooted ambition, his guidance and encouragement are valued dearly. Equally I would like to thank Dr Evgeniy Shapiro for his commitment to my academic development; I have been inspired by you, thank you.

During my PhD I have enjoyed both my subject matter and my social adventures. I would like to thank everybody who has ever helped me on my journey. In particular, Ioannis Kokkanakis, Zacharias Zachariadis and Marco Hahn for their friendship and support. Also, I would like to thank my friend George Skoufias for allowing me to sleep on a comfortable sofa, on an ad-hoc basis, at short notice on several occasions.

Many thanks go to my father Mohammed Tayyab Malick and beloved sister Naveed Wood for their help when I needed it. I would also like to thank Hayley Louise Garner for her love and patience during the time that I have known her. Finally I would like to thank my mother, Ulviye Malick for her support, both financial and emotional, over the last ten years during my time within Higher Education.

Contents

List of Figures

List of Tables

Abbreviations

AC	Artificial Compressibility
BCS	Real time duration of boundary conditions subroutine
CBS	Characteristics Based Scheme
CFD	Computational Fluid Dynamics
CHF	Critical Heat Flux
CHT	Conjugate Heat Transfer
DFT	Discrete Fourier Transform
DNS	Direct Numerical Simulation
FMG-FAS	Full Multigrid Full Approximation Storage Algorithm
HLLC	Harten-Lax-van Leer Contact
HPC	High Performance Computing
ILES	Implicit Large Eddy Simulation
Inv-X	Real time duration of inviscid flux calculations in x direction
Inv-Y	Real time duration of inviscid flux calculations in y direction
Inv-Z	Real time duration of inviscid flux calculations in z direction
IPS	Number of Processors
IVP	Initial Value Problem
JET	Joint European Torus
LDA	Laser Doppler Anemometry
LES	Large Eddy Simulation
MAST	Mega Amp Spherical Tokamak
MILES	Monotonically Integrated Large Eddy Simulation
N	Number of Nodes
NBH	Neutral Beam Heating
PDE	Partial Differential Equations
R-K	Runge-Kutta
RANS	Reynolds Averaged Navier-Stokes
RHS	Right Hand Side
SGS	Sub Grid Stress
SWP	Real time duration of sweep subroutine
TGL	Taylor Görtler-Like
UKAEA	United Kingdom Atomic Energy Authority
Vis-X	Real time duration of viscid flux calculations in x direction
Vis-Y	Real time duration of viscid flux calculations in y direction
Vis-Z	Real time duration of viscid flux calculations in z direction

Nomenclature

Roman Symbols

a, b, c, d ..... Arbitrary coefficients

f ..... Forcing term

F ..... Fourier number

G ..... Non-dimensional mass flux

K ..... Auxiliary function

L ..... Non-dimensional length

N ..... Number of grid points

p ..... Non-dimensional pressure

Q ..... Non-dimensional total (integral) heat flux

S ..... Non-dimensional control surface

s ..... Artifical speed of sound

t ..... Non-dimensional time

T ..... Non-dimensional temperature

u ..... Non-dimensional u velocity component

v ..... Non-dimensional v velocity component

V ..... Non-dimensional volume

w ..... Non-dimensional w velocity component

W ..... Width dimension in hybrid lid driven cavity case

x ..... Non-dimensional Cartesian x coordinate

y ..... Non-dimensional Cartesian y coordinate

z ..... Non-dimensional Cartesian z coordinate

Subscript Symbols

C_p ..... Specific heat capacity

C_1, C_2 ..... Arbitrary constants

G_{ideal} ..... Ideal mass flux (non-dimensional)

H_{chan} ..... Height of channel in hybrid lid driven cavity arrangement

k_{sf} ..... Ratio of solid and fluid thermal conductivity constants (non-dimensional)

L_x ..... Non-dimensional domain length in x Cartesian direction

L_y ..... Non-dimensional domain length in y Cartesian direction

L_z ..... Non-dimensional domain length in z Cartesian direction

L_β ..... Internal channel length in Chang & Kwak (1984) (non-dimensional)

P_{ent} ..... Non-dimensional entrance pressure

P_p ..... Periodic pressure component

$Q_{Left,Right}$ ..... Left and right wall heat fluxes in hybrid lid driven case

S_i ..... Non-dimensional set of face elements (due to multiblock grids)

T_w ..... Non-dimensional wall temperature

T_f ..... Non-dimensional temperature of fluid

T_s ..... Non-dimensional temperature of solid

$T_{sl,su}$ ..... Non-dimensional temperature at lower (outer) or upper wall surfaces

T_W ..... Wall interface temperature

t_{av} ..... Non-dimensional time averaging window

T_f ..... Non-dimensional temperature of fluid

T_s ..... Non-dimensional temperature of solid

u_i ..... Non-dimensional velocity of a point in space

U_b ..... Non-dimensional (bulk) velocity

$x_{0,1}$ ..... x coordinate location at far left and right of domain

$z_{0,1}$ ..... z coordinate location at near and far end walls

Superscript Symbols

a^* ..... Speed of sound

L^* ..... Length

n^* ..... Wall normal direction

p^* ..... Pressure

t^* ..... Time

T^* ..... Temperature

u^* ..... u velocity component

u^n ..... Non-dimensional velocity of a fixed point in time

u' ..... Non-dimensional fluctuating u velocity component

v^* ..... v velocity component

v' ..... Non-dimensional fluctuating v velocity component

w^* ..... w velocity component

w' ..... Non-dimensional fluctuating w velocity component

x^* ..... Cartesian x coordinate

y^* ..... Cartesian y coordinate

z^* ..... Cartesian z coordinate

Double Denoted Symbols

$c^{1,2}_{sl,f,su}$ ..... Constants in one dimensional three layer composite model

l^*_c ..... Reference length

p^*_c ..... Reference pressure

t^*_c ..... Reference time

T^*_c ..... Reference temperature

T^*_f ..... Temperature of fluid

T^*_s ..... Temperature of solid

u_c^* ..... Reference velocity

x_c^* ..... Reference Cartesian x length

y_c^* ..... Reference Cartesian y length

y_τ^* ..... Viscous length scale

z_c^* ..... Reference Cartesian z length

Greek Symbols

α^* ..... Thermal diffusivity

α_f^* ..... Thermal diffusivity of fluid

α_s^* ..... Thermal diffusivity of solid

α_{sf} ..... Ratio of solid and fluid thermal diffusion constants (non-dimensional)

β ..... Artificial compressibility parameter (non-dimensional)

ϵ ..... Random number ranging from 0 to 1

ζ ..... Coordinate (direction) of computational space

η ..... Coordinate (direction) of computational space

θ ..... Arbitrary angle

$\lambda_{0,1,2}$ ..... Eigenvalue

λ_n ..... Constant in conjugate heat transfer validation case

μ ..... Non-dimensional dynamic viscosity

ν ..... Non-dimensional kinematic viscosity

ν^* ..... Kinematic viscosity

ν_c^* ..... Reference kinematic viscosity

ξ ..... Coordinate (direction) of computational space

ρ ..... Non-dimensional density

ρ^* ..... Density

ρ_c^* ..... Reference density

τ ..... Non-dimensional pseudo time

τ_a ..... Timescale for advection

τ_c ..... Timescale for conduction

τ_f ..... Timescale for flow establishment

τ_{ij} ..... Non-dimensional shear stress tensor components

τ_w ..... Non-dimensional wall shear stress

τ_w^* ..... Wall shear stress

Vector Quantities

$\mathbf{D}$ ..... Shear stress vector

$\mathbf{E_I}$ ..... Curvilinear inviscid flux vector

$\mathbf{E_I^c}$ ..... Cartesian inviscid flux vector

$\mathbf{E_l}$ ..... Linear drop component of pressure vector

$\mathbf{E_p}$ ..... Periodic pressure component vector

$\mathbf{E_u}$ ..... Convective flux vector

$\mathbf{E_V}$ ..... Curvilinear viscid flux vector

$\mathbf{E_V^c}$ ..... Cartesian viscid flux vector

$\mathbf{n}$ ..... Normal vector

$\mathbf{u}$ ..... Velocity vector

$\mathbf{U}$ ..... Solution vector, i.e. $\mathbf{U} = \left(\frac{p}{\beta}, u, v, w, T_f\right)^T$

$\mathbf{U^n}$ ..... Solution vector at fixed point in time

$\mathbf{U_r}$ ..... Real time solution vector, i.e. $\mathbf{U_r} = (0, u, v, w, T_f)^T$

$\mathbf{V_L}$ ..... Left state of intercell characteristic variables

$\mathbf{V_R}$ ..... Right state of intercell characteristic variables

Mathematical Operators

J ..... Jacobian of the curvilinear coordinate transformation

$< . >$ ..... Ensemble averaged quantity

∇ ..... Divergence operator

Chapter 1

Introduction

1.1 Nuclear Fusion and Plasma Heating at JET

The UKAEA was established in 1954 as a statutory corporation to oversee the development of nuclear energy programmes within the United Kingdom. The UKAEA operates UK and European fusion power research programmes at the Culham Science Centre, Oxford. This includes the world's most powerful fusion research experiment, the JET facility.

Nuclear fusion is the energy producing process which takes place continuously in the sun and stars. At the temperatures required for the fusion reaction, (over $1,000,000$ K) the fuel changes its state from gas to plasma. In a plasma, the electrons are separated from the atomic nuclei (ions). Magnetic fields may be used to isolate the plasma from the vessel walls. Currently, the most promising magnetic confinement systems are toroidal, the most advanced being the Tokamak. JET is currently one of the largest Tokamaks in the world.

Various techniques exist to accelerate and increase the temperature of the plasma. The JET facility at Culham achieves enhanced plasma conditioning via a procedure

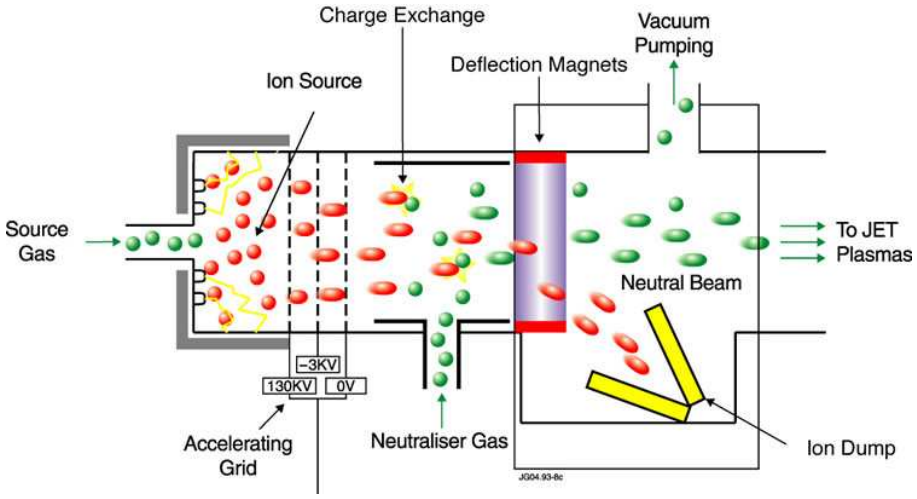

Figure 1.1: Neutral beam heating at JET, image provided by the UKAEA.

known as Neutral Beam Heating (NBH), for a review see Speth (1989). The NBH procedure injects a high speed, high energy, neutral beam into the plasma. The neutral beams are produced in two distinct phases. Firstly, a beam of energetic ions is produced from the source gas by applying an accelerating voltage of up to 140,000 volts known as the acceleration stage. A second stage ensures the accelerated beams are neutralised before injection into the plasma. The neutralised beam is injected directly into the plasma field and the remaining still ionised parts are directed on to high heat flux elements, known as "Hypervapotrons". Hypervapotrons provide an ion dump that is capable of dissipating large quantities of heat energy during beam heating, see Figure [1.1] for an illustration of the process.

1.2 Hypervapotron Devices

The rapid development of the entire fusion process at large is constantly increasing the need for secondary devices, such as the Hypervapotron, to operate for longer durations and under more vigorous working conditions. Ion dumps used in the fusion process experience exposure to extremely high temperatures during beam activation.

The experience of using Hypervapotron elements without failure for several years has demonstrated the reliability of such devices as discussed in Falter & Thompson (1995).

The performance of Hypervapotron beam-stopping elements under different operational conditions has received some attention from Cattadori *et al.* (1993b) and Tivey *et al.* (1987). These investigations revealed the operating limits of the devices and demonstrated the power handling capabilities of such a heat sink. Hypervapotrons provide an effective means to dissipate significant heat energy in short pulsing and this has motivated investigations into the performance of the high heat flux devices at longer durations, see Milnes *et al.* (2005).

Hypervapotrons are water cooled tiles which have been developed at JET. Despite the eccentric name and its seemingly advanced application, the Hypervapotron is a remarkably simple cooling device that is characterised by a distinct channel flow arrangement. The channel walls are ribbed and these ribs or fins play a key role in the heat and momentum transfer in the mainstream flow, thus affecting the overall heat transfer characteristic of the device.

It has been suggested by Boyd (1985) that the Hypervapotron technique, which involves fins placed transverse to the fluid flow in the device, "is one of the most intriguing fin enhancement techniques predicated on the idea of allowing a portion (the base) of the fin to operate at a temperature greater than the Critical Heat Flux (CHF), while the remaining portion operates near the onset of stable nucleate boiling".

This remarkable concept allows increased efficiency for the cooling device and therefore is a desired characteristic within the Hypervapotron main section. However, the ability to keep heat fluxes low enough so that nucleate boiling occurs where resulting heat transfer coefficients are highest is the ultimate design consideration

and may not be achieved solely by changes in geometric parameters.

Although several options exist to increase the critical heat flux of the cooling device, the shape and geometry remain the most appealing parameters to consider. Both the cavity size and channel diameter are under consideration here and it remains to find the most efficient geometry based on existing designs used at the JET facility.

A recent study by Chen *et al.* (2008) considers the use of a refrigerant (R134a) in the study of heat transfer characteristics within Hypervapotron devices. The steady state and transient thermal-hydraulic characterisation of full scale ITER divertor plasma facing components conducted by Tincani *et al.* (2008) involved both experimental and numerical work to establish the draining, drying and steady state characteristics of the flow and heat transfer using a multi-phase one dimensional network flow solver RELAP5.

Very few numerical studies based on established three dimensional solutions are available. However, simulations conducted using the Neptune multi-phase flow solver have been considered by Pascal-Ribot *et al.* (2007). Within that study, attempts to model the two phase flow development for two seconds of time were made. An important point to highlight is that previous information relating to the flow field present in Hypervapotrons under operational conditions was extremely limited, see Pascal-Ribot *et al.* (2005) and Falter & Baxi (1992).

For such reasons it was required for validation to occur against the cavity and channel flow arrangements (available in the relevant literature) using the applied formulations, thus ensuring confidence in the numerical model and more importantly the results obtained from these simulations.

A broad spectrum of data including transient data is available for rectangular open and closed cavity flows which provided a robust validation source for the flow solver.

1.2.1 Cavity Flows

Experimental apparatus and rigs have been utilised to achieve further understanding into the topic of open cavity flows. The most relevant are those which involve the consideration of the convective flow due to the interaction between the channel inertia and cavity flow.

Various experimental reports seek to establish a relationship of the Nusselt number in terms of the Reynolds and Prandtl numbers, see Richards *et al.* (1987), Betts & Bokhari (2000) and Chatellier *et al.* (2004). These correlations have been used to establish the range of the parameters effecting open cavity flows with heat transfer e.g. aspect ratios, flow field regimes and temperature distributions, however many do not consider water as the working fluid. An analytical model has been derived for the heat transfer characteristics with cavities made from different wall materials including copper. The thickness of the approaching boundary layer and its impact have also been observed, as well as an apparent transition from laminar to turbulent flow, as in Richards *et al.* (1987).

Investigations of convection in a channel with an open cavity below, see Brown & Lai (2002), have been conducted. Another example is Manca *et al.* (2006) where the forced convection and local heat transfer coefficient for rectangular cavities over a range of Reynolds number and variants of aspect ratio were studied.

A more simple problem is the benchmark case of a viscous incompressible fluid flow within a lid driven cavity. However, many studies in this region have been conducted with heat transfer although most only consider low Reynolds numbers, as in, Prasad & Koseff (1996) and Poujol (2000). Contrary to this, the problem has been studied at turbulent Reynolds numbers extensively without heat transfer by Leriche & Gavrilakis (2000), Verstappen *et al.* (1994) and Deshpande & Milton (1998).

Benchmark data for turbulent fluctuations have been recorded via Laser-Doppler Anemometry (LDA) experiments in Prasad & Koseff (1989). This provides data on two centrelines in a turbulent, three dimensional, lid driven cavity with a Reynolds number of 10000.

The lid driven cavity is an idealisation of a number of fluid mechanics problems. The flow field exhibits several phenomena which may be of interest at a design stage where shear flows are enclosed and generate recirculation. It is thought that the case is particularly relevant to the problem in hand since much of the flow dynamics that appear in a lid driven cavity also are found between the fins in Hypervapotron main sections. Many turbulent flows that have been investigated have an external body force applied on the fluid, for example a mean pressure gradient in flow through a plane channel or flows with heat transfer where buoyancy forces exist. However, for a lid driven cavity flow energy is transferred to the fluid via the moving lid and this shear motion leads to a primary captive vortex and secondary flow structures in the domain.

1.2.2 Ribbed Channels

Turbulent flow over cavity arrangements also referred to as rib roughened channels, is defined as a flow in a channel where transverse ribs with differing height, width and spacing are introduced. This is considered to be a useful model to study heat and mass transfer in Hypervapotrons.

Experimental data for a ribbed channel is also limited, see Billy *et al.* (2003), however, attention has been given to turbulent properties and flow structure along a ribbed surface in previous studies by Kyung-Soo (2000) and more recently by Cui *et al.* (2003).

Although several numerical studies have been conducted for flow over cavities and

ribbed roughened surfaces, many solve the RANS equations, with relatively simple turbulence models, without explicitly resolving the boundary layer. Here a "law of the wall" technique is adopted with a specified roughness correlation. In general, the computed mean velocities compare well with experimental results. However, large discrepancies are seen from calculated and measured turbulent properties in the separated flow and near wall regions. In these cases it is suggested that the law of the wall and pitfalls of the turbulence models contribute to the lack of accuracy.

It has been found through RANS studies that the Reynolds and Grashof numbers control the flow pattern and formation of recirculating cells for a fixed aspect ratio. Also, the aspect ratio has an influence on the orientation of recirculation zones, see Leong & Lai (1997). It has been noted that at low Reynolds numbers the heat transfer rate approaches that of free convection.

Large Eddy Simulations (LES) of flow and heat transfer in rib-roughened channels have appeared in the relevant literature less frequently. A useful study was carried out by Ciofalo & Collins (1992). Here the Smagorinsky model with Van Driest damping near the walls was implemented to model sub-grid scale effects. The rib height was 1/4.8 of the channel height and the pitch-to-height ratio was 7:2. The mean flow rate and the turbulence in the core flow region was greater in magnitude when compared with experimental data and $\kappa-\epsilon$ type modelling.

Explicit LES simulations have also been conducted recently where open cavity flows have been investigated. The studies have taken the form of, flows past cavities, see Yao *et al.* (2001), flows through channels with rib roughness, for example Cui *et al.* (2003), flows through channels with periodic grooving, as in Kyung-Soo (2000) and fully developed flow found in a ribbed duct considered by Lohsz *et al.* (2005).

Since the flow field in the Hypervapotron is assumed to be fully developed, the streamwise periodic channel flow arrangement has a particular significance to the

modelling and analysis of the problem. Several numerical investigations regarding periodic plane channel flows have been conducted, including benchmark cases for a turbulent Reynolds number, see Moser *et al.* (1999), and using Implicit LES by Fureby & Grinstein (2002).

The transient flow field within a periodically grooved duct has been established by Acharya *et al.* (1993), the investigation demonstrated the suitability of periodic boundary conditions when modelling large groups of cavities with heat transfer. However, in order to preserve mass flux in the modelling of periodic channel flows, the system must be subject to an algorithm adjustment in order to provide a suitable pressure drop in the domain Patankar *et al.* (1977a). This is termed as pressure forcing and enables the mass flux in a periodic channel to be conserved Lenormand & Sagaut (2000). The numerical correction has also been employed by Deschamps (1988) in the context of an incompressible flow. Similarly the bulk temperature drop in the heated channel case must also be maintained Patankar *et al.* (1977b), the latter temperature forcing technique has been applied by Acharya *et al.* (1993) and others.

Direct Numerical Simulation (DNS) was undertaken by Miyake *et al.* (2001) of rough-wall heat transfer in a turbulent channel flow. Two dimensional ribs (k-type) were considered. The major effect of the roughness element was to enhance the turbulent mixing and heat transfer. However, it was shown that the mixing was controlled by large scale motions in the logarithmic layer. A similar investigation by Stalio & Nobile (2003) shows the effect of riblets for flow manipulation and heat transfer.

The use of cavity arrays with heat transfer within industrial settings is becoming consistently more frequent, however the particulars of the geometry may differ significantly from the Hypervapotron designs and seldom are conditions, fluid and material properties similar to that under consideration here.

1.3 Numerical Methods and Implicit Large Eddy Simulations

Despite more than a century of research into turbulent motion, a generic closure or universal turbulence model has not been discovered. Turbulence provides for the rapid transport of heat and momentum to and from surfaces and is an issue for most flows of practical importance. A perplexing feature of turbulence is the vast range of spatial scales that contribute to the flow dynamics. In the majority of cases the range of scales is overwhelming the computational resources currently available. Many experimental and theoretical studies have increased our physical understanding of turbulent phenomenon, however, currently we fail to accurately and reliably predict turbulent flows in many cases.

The strong rotational nature of turbulent motion means that the problem is truly three dimensional. The time dependent, three dimensional Navier-Stokes equations include all the physics of a (Newtonian) turbulent flow. The scales present in a turbulent motion are ordinarily far larger than even the smallest molecular length scale. The ratio of smallest to largest scales rapidly decreases with an increasing Reynolds number. The number of grid points required to capture all scales of motion present in a turbulent flow may be estimated by the relation:

$$N \ \alpha \ \left(\frac{u_c^* l_c^*}{\nu^*}\right)^{\frac{9}{4}} = Re^{\frac{9}{4}} \tag{1.1}$$

where u_c^* and l_c^* are the characteristic velocity and length scale of the largest eddies in the turbulent flow. A turbulent eddy can be thought of as a local swirling motion where the characteristic dimension is the local turbulence scale. Eddies overlap in space; large ones carrying smaller ones. A cascading process is established whereby the larger eddies pass kinetic energy to the smaller ones, and the smaller to the even

smaller and so on until finally the smallest eddies dissipate into heat through the action of molecular viscosity. Thus it can be stated that turbulence is a dissipative mechanism and turbulent flows are always dissipative Wilcox (1998).

This lack of understanding of turbulence imposes limits on the development of technological industries at large, hence, further understanding of the physics of a turbulent motion is the motivation for considerably improving modelling techniques and numerical methods for turbulent fluid flows. Currently the three mainstream approaches to simulating a turbulent flow are presented in the literature; DNS, LES and RANS. The accuracy and computational efficiency of each approach is different.

The DNS approach delivers a complete transient and spatially accurate solution of the Navier-Stokes equations. Since all scales of motion are resolved, DNS is the only approach where accuracy is invariably retained. However the grid resolution requirements and thus, the computational cost, increases with the Reynolds number rapidly making DNS a viable option only for low Reynolds number flows. For example, it requires 10^{16} grid points and several thousand years to directly simulate the flow around an aircraft for one second of flight time on a supercomputer of 10^{12} Flops, see Moin & Kim (1997). Although this reference may be 13 years old; according to Moore's Law the introduction of transistors doubles approximately every two years. This rate suggests, typically, for a flow scenario such as flow past a full aircraft geometry the RANS equations are the only practical means of computing the flow for the forseeable future. RANS is a time-averaging approach where turbulence consists of random fluctuations of the flow variables. All variable quantities are expressed as the sum of mean and fluctuating parts and the Navier-Stokes equations are averaged over a time interval. RANS simulations are widespread in steady-state computations where turbulence is stationary, see Leschziner (2000) and Leschziner & Drikakis (2002). Further within unsteady flows, the timescale associated with the organised unsteady motion exists and must be well separated from the time-scale of

turbulent motion.

The function of turbulence modelling in RANS is to approximate the unknown Reynolds stresses which are a result of the time averaging process in order to close the system. The closure relations are commonly based on empirical and experimental correlations of shear stress parameters in the flow. In reviews such as Leschziner (2000) and Leschziner & Drikakis (2002) the performance of a number of turbulence models has been considered. It has also been shown that the linear eddy-viscosity models often fail to accurately predict complex flows involving separation, free shear layers and vortical structures. Previous studies have shown that the numerical accuracy depends not only on the turbulence model employed, but also on the discretisation of the advective terms, see Drikakis & Durst (1994).

In LES the Navier-Stokes equations are filtered. The filtering operation decomposes the flow field solution into the sum of a filtered (resolved, large scales) component and a residual, Sub Grid-Scale (SGS) component. Models for the effects of the unresolved small scales on the flow are known as SGS models. The evolution of the filtered component representing the large scales is described by the filtered Navier-Stokes equations. The equations are presented in a standard form, with the momentum equation containing the SGS stress tensor that arises from the unresolved residual motions. The system can be closed by an eddy-viscosity model that relates the unknown correlations represented by the SGS stress tensor with a sub-grid viscosity. LES can be regarded as intermediate between DNS and RANS with respect to accuracy and computational time efficiency.

Conventional LES also incorporates SGS modelling. There are two main branches of conventional (explicit) SGS modelling; these are functional and structural models. Drawbacks of such models include commutation and aliasing errors, limitations with regard to compressible flows and masking of the SGS terms by the truncation error. When deriving the LES equations it was assumed that differentiation commutes

with convolution, see Ghosal & Moin (1995), Fureby & Tabor (1997). However, this is not the case at wall boundaries and for variable filter widths. The former requires consideration of a finite domain, which introduces commutation errors in the spatial derivatives. If the finite domain changes in time, additional errors in the temporal derivatives arise. A variable filter kernel could solve the problems at solid boundaries by reducing the filter width in order to resolve small scales, however this procedure violates the above commutation assumption and introduces new errors, which can be removed by correction terms. Currently there are no available methods to tackle these correction terms. Some previous work conducted has focused on filters that can eliminate these terms, see Vasilyev *et al.* (1998),Ven (1995).

The discretisation of the Navier-Stokes equations involves the derivative terms being substituted with numerical approximations, this implicitly introduces higher order dissipation and dispersion terms Margolin & Rider (2002). The success of high resolution methods to compute turbulent flows depends upon the balance of truncation errors introduced by wave speed dependent terms. The dissipation terms are responsible for the numerical diffusion, especially near discontinuities. The dispersion terms are responsible for generating oscillations, again, near discontinuities.

For the past decade it has been observed that high-resolution methods in LES numerically augment the solution, effectively modelling the SGS tensor Fureby & Grinstein (2002), Drikakis (2003). The concept to utilise this inherent characteristic as an implicit way to numerically model complex turbulent flows is an evolving area of research referred to as ILES or Monotonically Integrated LES (MILES).

A classical LES approach separating scales by filtering is well suited to unbounded flows, but in the case of a bounded flow, the scales are not easily separated Drikakis & Rider (2005). Here, close to boundaries, turbulence manifests itself in the form of coherent structures which cannot be described by eddy-viscosity modelling. As a result eddies close to wall boundaries still need to be resolved. It is arguments

such as these that have been the motivation for a new, more versatile approach to turbulence modelling within a LES framework.

The MILES concept introduced by Boris & Book (1976) has received relatively less attention than explicit LES modelling approaches. However the emergence of this class of numerical approach is fast developing Grinstein *et al.* (2007). Not all implicit SGS modelling will work, the numerical scheme has to be constructed so the leading truncation errors effectively model the SGS tensor. Hence non-linear discretisation is required in order to control the SGS term impact, as required in areas of the flow domain where sharp changes in flow field variables exist.

The physical requirements for non-linear implicit SGS models include adaptiveness to local flow physics and sharp velocity-gradient capturing. ILES is a very simple and robust approach to solving turbulent flows. Essentially the most impressive feature of the method is that it reduces the requirement to introduce an explicit model for unresolved scales. The mathematical justification is relatively recent and is fundamentally based on the modified equations Margolin & Rider (2002).

1.3.1 Validation of ILES in a Wall Bounded Flow

Implicit SGS modelling has been previously implemented using local monotonicity preservation in conjunction with various different numerical schemes; Flux Corrected Transport Fureby & Grinstein (1999), Piecewise Parabolic Methods Woodward (1986) and Godunov type Riemann solvers have been successfully used to achieve highly accurate solutions of turbulent flow problems. The solutions obtained for channel flows Fureby & Grinstein (2002) and benchmark problems such as the transition and turbulence decay in a Taylor-Green vortex have shown ILES to be a highly accurate solution approach Hahn & Drikakis (2005) whilst being significantly less complex than conventional SGS models.

It has been noted that this kind of modelling approach (ILES) with consistent and stable numerics converges to a solution with comparable accuracy of a DNS solver whilst being significantly less computationally demanding Grinstein & Fureby (2004). The behaviour of ILES for flows where more complex fluid dynamics exist is yet to be investigated. The ILES approach has not been utilised for open cavity flows previously, nor does it benefit from widespread participation.

Important information and comparative analysis of solutions achieved with ILES against other explicit LES models can be acquired through previous studies conducted for channel and cavity flow arrangements. Further, lid driven cavity flows have received considerable attention in the context of LES, RANS and experimental investigations. Commonly the case is used for validation purposes for Computational Fluid Dynamics (CFD) codes since the boundary conditions are well posed making the lid driven case a benchmark model.

DNS Leriche & Gavrilakis (2000), Explicit LES Zang *et al.* (1993) and RANS Ghia *et al.* (1982) simulations of this kind also exist. The development of incompressible formulations has been extended within based on an artificial compressibility pressure coupling in conjunction with ILES to resolve low speed, three dimensional, turbulent flows, with accuracy.

Validation is provided for high resolution, ILES formulations in a wall bounded application for a turbulent, low Reynolds number. The impact of the high order reconstruction in conjunction with the CBS (Characteristics Based Scheme), first proposed by Drikakis *et al.* (1994), is investigated. Here the advective terms are solved using a Riemann solver that incorporates high order reconstruction methods.

The impact of the high order scheme provides greater accuracy in calculation of the advection terms of the governing equation. Within the thesis the effect on results using first, second and third order reconstructions are reported.

1.3.2 Analysis of Fluid Flow and Heat Transfer in Hypervapotrons used at JET

The testing of Hypervapotron elements has previously been conducted at the JET fusion facility. However, the Hypervapotron device is inherently hard to rig for experiment due to its unconventional internal dimensions. Simulations are now becoming an integral part of the design process for these high heat flux elements.

It is suggested that the flow field may be sufficiently resolved using the methods detailed within. By taking advantage of parallel computing techniques, fine grids can be used in the three dimensional model.

Computational modelling of the device has enabled information to be gained relating to the wall heat fluxes which were previously not achieved through several studies, conducted by the UKAEA, using finite elements analysis. Information that has previously been unavailable such as, flow structure, velocities and temperature distributions for the Standard design at different Reynolds number are invaluable information at the current time.

Both cavity size and channel height are parameters that have been subject to previous investigation, see Figures [1.2]-[1.3]. The shape of the cavity base has introduced additional complications to the mathematical model which are further discussed in the forthcoming chapters.

Information developed in this thesis is the first of detailed ILES simulations conducted using a finite volume method relating the flow field and heat transfer in Hypervapotrons.

The designs currently used at JET are the "Standard" and "Mega Amp Spherical Tokamak (MAST)" configurations, differences between the designs are noted as the channel height, cavity height and wall thickness.

Table 1.1 describes the design of the cavity arrangements using three characteristic dimensions. All fins and cavities are 3mm wide, in the direction of the flow. A three dimensional schematic of the designs can be found in Appendix A.

HV design	*A*	*B*	*C*
Standard	6mm	8mm	6mm
MAST	5mm	4mm	17.6mm

Table 1.1: Basic dimensions of the Standard and MAST designs.

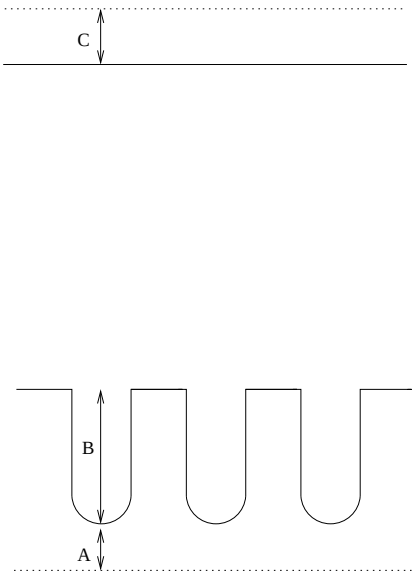

Figure 1.2: Two dimensional schematic of the Standard design.

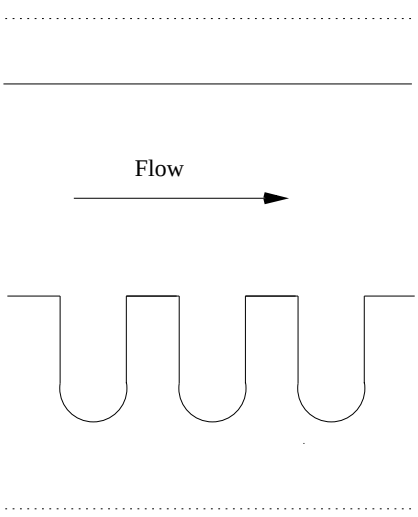

Figure 1.3: Two dimensional schematic of the MAST design.

1.4 Summary of Aims and Objectives

The main aim of the thesis is to *shed the light on the flow structure and heat transfer processes within the main duct section of the Hypervapotron devices using CHT ILES modelling.* In order to achieve this aim the following objectives were set out:

- Development and validation of ILES artificial compressibility based solver for liquid flow modelling.
- Development and validation of the conjugate heat transfer solver.
- Analysis of the transient flow and heat transfer in the Standard design with fixed temperature boundary conditions in the fluid domain.
- Analysis of the transient flow and heat transfer in the CHT ILES model of the Standard design.

1.5 Outline of the Thesis Organisation

The present thesis is composed of six chapters. Each chapter relies on the knowledge of the previous chapter.

Chapter 2

This chapter is devoted to the governing equations and numerical methods that have been implemented in order to gain the data for the following sections. The chapter outlines the governing equations and the narration highlights the justification for such models and methods. Several different concepts are outlined here such as the high resolution methods.

The governing equations are presented in the form of generalised curvilinear coordinates. The post-processed parameters are also presented here. The procedure used to calculate all the turbulent and mean flow quantities is also outlined here.

Chapter 3

Chapter 3 addresses the first objective via the investigation of turbulent flow in a cubical, lid driven cavity. The AC-ILES formulation is shown to provide a good comparison with an experimental study of the flow field against the LDA measurements of Prasad & Koseff (1989). This provided the validation of the numerical methods for the fluid flow solver. The formulation was benchmarked against the lid driven case. The presence of recirculations and flow unsteadiness is typical to that seen within the cavities of the main duct section of Hypervapotron devices.

Chapter 4

Chapter 4 addresses the second objective. It presents validation for the conjugate heat transfer model using analytic solutions and comparisons with the published literature. Numerical heat transfer including the conjugate solid-fluid model and analytical agreement with the solver is presented.

Comparisons against a hybrid lid driven cavity is presented also where a laminar steady state solution of the computational model is achieved. Data has been compared with another numerical investigation where the focus is on the heat transfer from wall boundaries.

Chapter 5

Chapter 5 addresses the last two objectives. It is dedicated to the simulation of Hypervapotron configurations at sub boiling temperatures. Computational amendments required including pressure forcing for the periodically developed problem is derived.

Detailed analysis of the flow properties and heat transfer within the main duct section of the Standard design is presented.

Chapter 6

The main findings of the simulations including the validation cases is discussed. Also the flow field solution for the Hypervapotron cases based on current grids is summarised. In addition the entire work is critically evaluated to establish the major challenges and issues with this study. Finally, further work and proposals based on the current methodology as well as other available methods completes the thesis.

Chapter 2

Governing Equations and Computational Methodology

2.1 Governing Equations

Within this chapter the governing equations for the flow and temperature fields are outlined. The model of the Hypervapotron has to meet the conservation of mass, momentum and energy.

2.1.1 Conservation of Mass

The conservation of mass states that the rate of change of mass within a control volume, is equal to the mass flow rate out of the control surface. Assuming the flow is incompressible and variation in density is negligible, the continuity equation reduces to the incompressibility constraint given by the divergence of velocity equal to zero:

$$\nabla \cdot \mathbf{u}^* = \frac{\partial u^*}{\partial x^*} + \frac{\partial v^*}{\partial y^*} + \frac{\partial w^*}{\partial z^*} = 0 \tag{2.1}$$

Note, here and throughout the thesis the superscript "*" is used to denote the quantities with dimensions. Quantities without the "*" superscript are non-dimensional.

2.1.2 Conservation of Momentum

Conservation of momentum is based on Newton's second law. It states that the time rate of change of (linear) momentum in a control volume, is equal to the sum of the net rate of momentum flowing out of its control surface and all external forces acting upon the control surface and volume.

The forces that are considered in this model are pressure forces and viscous stresses acting on the control surface. Introducing stress and strain rate tensors for the Newtonian fluid, making appropriate assumptions and applying Stokes's hypothesis, the constitutive equations for an isentropic fluid are determined. These may be introduced into the momentum equation, which is written in the conventional notation as:

$$\frac{\partial u^*}{\partial t^*} + \mathbf{u}^* \cdot \nabla \mathbf{u}^* = -\frac{1}{\rho^*}\nabla p^* + \nu^* \nabla^2 \mathbf{u}^* \tag{2.2}$$

This may be written in expanded form (with Cartesian coordinates) as:

$$\frac{\partial u^*}{\partial t^*} + \frac{\partial (u^*)^2}{\partial x^*} + \frac{\partial u^* v^*}{\partial y^*} + \frac{\partial u^* w^*}{\partial z^*} = -\frac{1}{\rho^*}\frac{\partial p^*}{\partial x^*} + \nu^* \left(\frac{\partial^2 u^*}{\partial x^{*2}} + \frac{\partial^2 u^*}{\partial y^{*2}} + \frac{\partial^2 u^*}{\partial z^{*2}} \right) \tag{2.3}$$

$$\frac{\partial v^*}{\partial t^*} + \frac{\partial u^* v^*}{\partial x^*} + \frac{\partial (v^*)^2}{\partial y^*} + \frac{\partial v^* w^*}{\partial z^*} = -\frac{1}{\rho^*}\frac{\partial p^*}{\partial y^*} + \nu^* \left(\frac{\partial^2 v^*}{\partial x^{*2}} + \frac{\partial^2 v^*}{\partial y^{*2}} + \frac{\partial^2 v^*}{\partial z^{*2}} \right) \tag{2.4}$$

$$\frac{\partial w^*}{\partial t^*} + \frac{\partial u^* w^*}{\partial x^*} + \frac{\partial v^* w^*}{\partial y^*} + \frac{\partial (w^*)^2}{\partial z^*} = -\frac{1}{\rho^*}\frac{\partial p^*}{\partial z^*} + \nu^* \left(\frac{\partial^2 w^*}{\partial x^{*2}} + \frac{\partial^2 w^*}{\partial y^{*2}} + \frac{\partial^2 w^*}{\partial z^{*2}} \right) \tag{2.5}$$

2.1.3 Conservation of Energy

In order to compute the heat transfer rate an additional equation for the temperature scalar was introduced into the system.

Assuming constant density, negligible radiation, external work and viscous energy dissipation; the thermal energy balance results in an advection-diffusion equation for the temperature scalar T_f^* in the flow:

$$\frac{\partial T_f^*}{\partial t^*} + \mathbf{u}^* \cdot \nabla T_f^* = \frac{k_f^*}{\rho^* c_p^*} \nabla^2 T_f^* = \alpha_f^* \nabla^2 T_f^* \tag{2.6}$$

Here α_f^* is the thermal diffusivity of the fluid. The subscripts "f" and "s" are introduced here to differentiate between the thermal transport coefficients and temperature of fluid and solid medias. Again we may write this in expanded form (with Cartesian coordinates) as:

$$\frac{\partial T_f^*}{\partial t^*} + u^* \frac{\partial T_f^*}{\partial x^*} + v^* \frac{\partial T_f^*}{\partial y^*} + w^* \frac{\partial T_f^*}{\partial z^*} = \alpha_f^* \left(\frac{\partial^2 T_f^*}{\partial x^{*2}} + \frac{\partial^2 T_f^*}{\partial y^{*2}} + \frac{\partial^2 T_f^*}{\partial z^{*2}} \right) \tag{2.7}$$

In the solid domain, the conventional heat transfer equation is solved, given by:

$$\frac{\partial T_s^*}{\partial t^*} = \alpha_s^* \nabla^2 T_s^* \tag{2.8}$$

Which is expanded in Cartesian coordinates as:

$$\frac{\partial T_s^*}{\partial t^*} = \alpha_s^* \left(\frac{\partial^2 T_s^*}{\partial x^{*2}} + \frac{\partial^2 T_s^*}{\partial y^{*2}} + \frac{\partial^2 T_s^*}{\partial z^{*2}} \right) \tag{2.9}$$

2.1.4 Dimensionless Formulation

Now the procedure of making the system of equations non-dimensional is outlined. The non-dimensional form of equations enables the reader to assess the relative importance of terms very quickly within the governing equations.

Quantities are defined by replacement of all dimensional variables with their corresponding non-dimensional form. The non-dimensional variables can be acquired through considering the characteristic reference values (which are dimensional).

All variables denoted by c indicate the reference quantity. Each variable for space, velocity, time, pressure and temperature is required to develop the non-dimensional system of equations:

$$x = \frac{x^*}{l_c^*}, y = \frac{y^*}{l_c^*}, z = \frac{z^*}{l_c^*} \tag{2.10}$$

$$u = \frac{u^*}{u_c^*}, v = \frac{v^*}{u_c^*}, w = \frac{w^*}{u_c^*} \tag{2.11}$$

$$t = \frac{t^*}{\frac{l^*{}_c}{u^*{}_c}}, p = \frac{p^*{}_c}{\rho^*{}_c u^{*2}{}_c} \tag{2.12}$$

We also require non-dimensional temperature, by defining T_c^* as a reference temperature and $\triangle T^*$ as the reference temperature difference the non-dimensional temperature in fluid and solid is defined as:

$$T_{f,s} = \frac{T_{f,s}^* - T_c^*}{\triangle T^*} \tag{2.13}$$

The reader should note that only the non-dimensional system of equations is com-

puted and the entire numerical solver was based on coding of the non-dimensional equations.

All boundary conditions and case results are also presented (where appropriate) as non-dimensional quantities from here on. Finally, the non-dimensional system of equations in the fluid may be expressed as:

$$\begin{cases} \nabla \cdot \mathbf{u} = 0 \\ \frac{\partial \mathbf{u}}{\partial t} + \mathbf{u} \cdot \nabla \mathbf{u} = \nabla p + \frac{1}{Re} \nabla^2 \mathbf{u} \\ \frac{\partial T_f}{\partial t} + \mathbf{u} \cdot \nabla T_f = \frac{1}{RePr} \nabla^2 T_f \end{cases} \tag{2.14}$$

Here the Reynolds $Re = u_c^* l_c^* / \nu^*$ and Prandtl $Pr = \nu^* / \alpha^*$ numbers have been introduced using the reference quantities for the fluid.

Since the conventional heat equation is solved in the solid domain the conjugate problem necessitates the application of the same non-dimensional treatment for both fluid and solid regions.

By using the characteristic fluid timescale to make non-dimensional the heat transfer equation in the solid, one arrives at:

$$\frac{\partial T_s}{\partial t} = \frac{\alpha_{sf}}{RePr} \nabla^2 T_s \tag{2.15}$$

Where α_{sf} denotes the ratio of the solid and fluid thermal diffusivities:

$$\alpha_{sf} = \frac{\alpha_s^*}{\alpha_f^*} \tag{2.16}$$

2.2 Numerical Approach

2.2.1 Artificial Compressibility

In the case of compressible equations and in particular within gas dynamics the equations have a strong coupling through the density variable in both the momentum and continuity equations. Further the pressure variable introduced by the equation of state in this case fully closes the system.

The incompressible form of the Navier-Stokes equations presents a difficulty with regard to coupling of the equations.

Several different incompressible methods exist. Many schemes exist for the vorticity and stream function formulations, vorticity-vector potential or vorticity-velocity formulations may be used to compute two and three dimensional flows.

Frequently incompressible formulations attempt to gain a stronger coupling between the momentum and continuity equations by introducing additional terms to the system. The most widely used formulations, pressure-Poisson proposed by Baker (1983) and Roache (1998) and other projection formulations developed are all suitable for low speed incompressible flow problems. A review of many approaches is documented in Drikakis & Rider (2005).

The results documented are simulations that originate from a variant of the incompressible Navier-Stokes equations, namely the Artificial Compressibility formulation, with an additional equation for the temperature scalar present. The Artificial Compressibility (AC) technique was originally developed by Chorin (1967) and later extended for unsteady flows by Merkle & Athavale (1987) and others.

Some of the benefits of using AC over other methods can be summarised quickly. The AC method results in hyperbolic and hyperbolic-parabolic equations for inviscid

and viscous incompressible flows, respectively. Commonly such forms of the equations may be computed using implicit and explicit solvers, where the latter is easily applied to sequential and parallel codes. Discretisation schemes and solvers developed in conjunction with the AC formulation for incompressible flows have many similarities with the methods developed for compressible flows. The computational experience and developments gained from compressible flows can easily be transferred to incompressible flows, for example Riemann solvers that allow propagation of information throughout the computational domain.

The coupling is achieved between the momentum and continuity equations by adding a pressure derivative in pseudo time to the latter. For unsteady problems pseudo time velocity derivatives need to be added to the momentum equation and for multi-scalar problems, pseudo time scalar derivatives also must be added to the scalar transport equations, see Shapiro & Drikakis (2005).

The pseudo time velocity is required for coupling and solving the governing equations in pseudo time, τ. The artificial compressibility parameter β is introduced as a coefficient to the new pressure derivative. This parameter provides relaxation which induces convergence in the system of equations. Introducing this coupling the non-dimensional system becomes:

$$\begin{cases} \frac{\partial p}{\partial \tau} = -\beta \nabla \cdot \mathbf{u} \\ \\ \frac{\partial \mathbf{u}}{\partial \tau} = -\frac{\partial \mathbf{u}}{\partial t} - \left(\mathbf{u} \cdot \nabla \mathbf{u} + \nabla p - \frac{1}{Re} \nabla^2 \mathbf{u} \right) \\ \\ \frac{\partial T_f}{\partial \tau} = -\frac{\partial T_f}{\partial t} - \left(\mathbf{u} \cdot \nabla T_f - \frac{1}{RePr} \nabla^2 T_f \right) \\ \\ \frac{\partial T_s}{\partial \tau} = -\frac{\partial T_s}{\partial t} + \frac{\alpha_{sf}}{RePr} \left(\nabla^2 T_s \right) \end{cases} \tag{2.17}$$

For each real time step, t, the solution of the system is obtained by iterating in pseudo time, τ, until convergence is achieved. Thus, the incompressibility (divergence free) condition is satisfied at every time step. One may also make an analogy with the equations of motion for a compressible low Mach number flow to suggest that the artificial compressibility factor is equal to the speed of sound squared, i.e. $s = \sqrt{\beta}$. The artificial compressibility method requires the parameter β to be determined in order to gain suitable convergence in both steady and transient flows.

In order to identify a optimal value for β, consideration of the relationship between the pseudo pressure waves and vorticity spreading an internal channel flow was considered by Chang & Kwak (1984). Based on this analysis it was found that interactions of the pseudo-sound waves and viscous effects, can be decoupled provided:

$$\beta >> \left(\left(1 + \frac{L_\beta}{Re}\right)^2\right) - 1 \tag{2.18}$$

Here L_β was the internal channel length. The value of $\beta = 1$ was used throughout the simulations presented for all cases studied within this thesis.

2.2.2 Curvilinear Coordinates

In order to provide a solution of the governing equations on stretched grids we start with the conservative form of the equations in Cartesian space. We describe the fluid flow and heat transfer in the fluid, by letting $\mathbf{U} = \left(\frac{p}{\beta}, u, v, w, T_f\right)^T$ and $\mathbf{U_r} = (0, u, v, w, T_f)^T$ be the solution vectors and define a more numerically convenient set of equations:

$$\frac{\partial \mathbf{U}}{\partial \tau} = -\frac{\partial \mathbf{U}_r}{\partial t} + \frac{\partial \mathbf{E_V^c}}{\partial x} + \frac{\partial \mathbf{F_V^c}}{\partial y} + \frac{\partial \mathbf{G_V^c}}{\partial z} - \frac{\partial \mathbf{E_I^c}}{\partial x} - \frac{\partial \mathbf{F_I^c}}{\partial y} - \frac{\partial \mathbf{G_I^c}}{\partial z} \tag{2.19}$$

Where the inviscid and viscous fluxes are given by:

$$\begin{cases} \mathbf{E_I^c} &= (u, u^2+p, uv, uw, uT_f)^T \\ \mathbf{F_I^c} &= (v, uv, v^2+p, vw, vT_f)^T \\ \mathbf{G_I^c} &= (w, uw, vw, w^2+p, wT_f)^T \\ \mathbf{E_V^c} &= \left(0, \frac{1}{Re}\frac{\partial u}{\partial x}, \frac{1}{Re}\frac{\partial v}{\partial x}, \frac{1}{Re}\frac{\partial w}{\partial x}, \frac{1}{RePr}\frac{\partial T_f}{\partial x}\right)^T \\ \mathbf{F_V^c} &= \left(0, \frac{1}{Re}\frac{\partial u}{\partial y}, \frac{1}{Re}\frac{\partial v}{\partial y}, \frac{1}{Re}\frac{\partial w}{\partial y}, \frac{1}{RePr}\frac{\partial T_f}{\partial y}\right)^T \\ \mathbf{G_V^c} &= \left(0, \frac{1}{Re}\frac{\partial u}{\partial z}, \frac{1}{Re}\frac{\partial v}{\partial z}, \frac{1}{Re}\frac{\partial w}{\partial z}, \frac{1}{RePr}\frac{\partial T_f}{\partial z}\right)^T \end{cases} \tag{2.20}$$

By considering an arbitrary curvilinear system, with coordinates:

$$\xi(x, y, z) \tag{2.21}$$

$$\eta(x, y, z) \tag{2.22}$$

$$\zeta(x, y, z) \tag{2.23}$$

The corresponding Jacobian of the transformation is given by:

$$J = \left|\frac{\partial(x, y, z)}{\partial(\xi, \eta, \zeta)}\right| = x_\xi(y_\eta z_\zeta - y_\zeta z_\eta) + x_\eta(y_\zeta z_\xi - y_\xi z_\zeta) + x_\zeta(y_\xi z_\eta - y_\eta z_\xi) \tag{2.24}$$

For the structured grids, the transformation to the curvilinear system is implicitly given by the indexing i.e. $(\xi, \eta, \zeta) = (i, j, k)$. Therefore the system of (2.19) can be written in curvilinear coordinates as:

$$\frac{\partial J\mathbf{U}}{\partial \tau} = -\frac{\partial J\mathbf{U}_r}{\partial t} + \frac{\partial \mathbf{E_V}}{\partial \xi} + \frac{\partial \mathbf{F_V}}{\partial \eta} + \frac{\partial \mathbf{G_V}}{\partial \zeta} - \frac{\partial \mathbf{E_I}}{\partial \xi} - \frac{\partial \mathbf{F_I}}{\partial \eta} - \frac{\partial \mathbf{G_I}}{\partial \zeta} \tag{2.25}$$

The inviscid, $(\mathbf{E_I}, \mathbf{F_I}, \mathbf{G_I})$, and viscous, $(\mathbf{E_V}, \mathbf{F_V}, \mathbf{G_V})$, fluxes are expressed through their Cartesian counterparts as:

$$\begin{cases} \mathbf{E_I} = J\left(\mathbf{E_I^c}\frac{\partial\xi}{\partial x} + \mathbf{F_I^c}\frac{\partial\xi}{\partial y} + \mathbf{G_I^c}\frac{\partial\xi}{\partial z}\right) \\ \mathbf{F_I} = J\left(\mathbf{E_I^c}\frac{\partial\eta}{\partial x} + \mathbf{F_I^c}\frac{\partial\eta}{\partial y} + \mathbf{G_I^c}\frac{\partial\eta}{\partial z}\right) \\ \mathbf{G_I} = J\left(\mathbf{E_I^c}\frac{\partial\zeta}{\partial x} + \mathbf{F_I^c}\frac{\partial\zeta}{\partial y} + \mathbf{G_I^c}\frac{\partial\zeta}{\partial z}\right) \\ \mathbf{E_V} = J\left(\mathbf{E_V^c}\frac{\partial\xi}{\partial x} + \mathbf{F_V^c}\frac{\partial\xi}{\partial y} + \mathbf{G_V^c}\frac{\partial\xi}{\partial z}\right) \\ \mathbf{F_V} = J\left(\mathbf{E_V^c}\frac{\partial\eta}{\partial x} + \mathbf{F_V^c}\frac{\partial\eta}{\partial y} + \mathbf{G_V^c}\frac{\partial\eta}{\partial z}\right) \\ \mathbf{G_V} = J\left(\mathbf{E_V^c}\frac{\partial\zeta}{\partial x} + \mathbf{F_V^c}\frac{\partial\zeta}{\partial y} + \mathbf{G_V^c}\frac{\partial\zeta}{\partial z}\right) \end{cases} \tag{2.26}$$

Similarly, the conservation of the temperature in the solid in curvilinear form is written as:

$$\frac{\partial JT_s}{\partial\tau} = -\frac{\partial JT_s}{\partial t} + \frac{\partial E_T}{\partial\xi} + \frac{\partial F_T}{\partial\eta} + \frac{\partial G_T}{\partial\zeta} \tag{2.27}$$

The scalar Cartesian viscous fluxes E_T^c, F_T^c, G_T^c for solid temperature are given by:

$$\begin{cases} E_T^c &= \frac{\alpha_{sf}}{RePr}\frac{\partial T}{\partial x} \\ F_T^c &= \frac{\alpha_{sf}}{RePr}\frac{\partial T}{\partial y} \\ G_T^c &= \frac{\alpha_{sf}}{RePr}\frac{\partial T}{\partial z} \end{cases} \tag{2.28}$$

The above Cartesian fluxes are transformed into the curvilinear system by the same transformation as given in Equation (2.26) for fluid flow equations.

2.2.3 Inviscid Fluxes Approximation

In a finite volume solver as used within the current formulations, the Riemann problem arises at cell interfaces and may provide poor accuracy within the domain. The Riemann problem is an initial value problem (IVP) which is defined by initial value piecewise constant data.

The solution between the cell interfaces is modelled using Riemann solvers often in conjunction with high resolution methods for more advanced interface solutions. This in turn increases the overall accuracy of the numerical scheme. Several Riemann solvers have been developed and solutions dependent on the eigenstructure tend to be the most accurate.

Popular schemes such as Roe's scheme Roe (1997), HLLC Toro *et al.* (2001) and Osher' scheme Engquist & Osher (1981) frequently appear in the literature. An important concept behind the Riemann problem is associated with the characteristic wave speeds in a flow problem. A useful review and derivation of several Riemann solvers may be found in Toro (1999).

Over the recent years several attempts to fully capture the flow physics of CFD problems have resulted in methods, or additions to schemes, known as high resolution methods. Such methods have been adopted most rigorously in high-speed flows and in shock interaction problems.

High resolution methods achieve this by applying a non-linear finite differencing stencil via a Riemann solver dependent upon the local flow solution whilst preserving monotonicity. This is opposed to methods that use the same differencing stencil throughout the domain regardless of the flow field solution.

A high resolution method involves averaging for cell interface values and reconstruction of the cell centred data. Following this the Riemann solver is applied and finally

the data is again re-averaged at the cell interface. An important concept behind the Riemann problem is associated with the characteristic wave speeds in a flow problem and the left and right states adjacent to the interface.

A useful review and derivation of several Riemann solvers may be found in Toro (1999). The Riemann solver used within the current investigations is the Characteristics Based Scheme (with high order reconstruction for inter cell variables). In the numerical reconstruction of the advective fluxes one can employ dimensional splitting.

In this work, dimensional splitting is used only for analytically deriving characteristics-based formulae for the inter cell variables, which in turn are used to calculate the advective fluxes.

The time integration is obtained for the complete system of equations after adding all the discretised fluxes (inviscid and viscous), using an explicit time integration. In order to derive characteristics based reconstructions we consider the one dimensional counterpart of (2.25), e.g., with respect to the ξ-direction:

$$\frac{\partial \mathbf{U}}{\partial \tau} + \frac{\partial \xi}{\partial x}\frac{\partial \mathbf{E_I^c}}{\partial \xi} + \frac{\partial \xi}{\partial y}\frac{\partial \mathbf{F_I^c}}{\partial \xi} + \frac{\partial \xi}{\partial z}\frac{\partial \mathbf{G_I^c}}{\partial \xi} = 0 \tag{2.29}$$

We divide the above equation by $\sqrt{\left(\frac{\partial \xi}{\partial x}\right)^2 + \left(\frac{\partial \xi}{\partial y}\right)^2 + \left(\frac{\partial \xi}{\partial z}\right)^2}$ and introduce the notation:

$$K = \sqrt{\left(\frac{\partial \xi}{\partial x}\right)^2 + \left(\frac{\partial \xi}{\partial y}\right)^2 + \left(\frac{\partial \xi}{\partial z}\right)^2} \tag{2.30}$$

The system is used solely for the CBS reconstruction of the advective flux in $\xi-$direction and a similar procedure can be used for the fluxes in the other two directions. The procedure is outlined here for the fluid flow equations only for sim-

plicity. The inviscid flux procedure for the temperature in fluid will be mentioned separately:

$$\begin{cases} \frac{1}{\beta K}\frac{\partial p}{\partial \tau} + \widetilde{x}\frac{\partial u}{\partial \xi} + \widetilde{y}\frac{\partial v}{\partial \xi} + \widetilde{z}\frac{\partial w}{\partial \xi} = 0 \\ \frac{1}{K}\frac{\partial u}{\partial \tau} + (u\widetilde{x} + v\widetilde{y} + w\widetilde{z})\frac{\partial u}{\partial \xi} + \left(\widetilde{x}\frac{\partial u}{\partial \xi} + \widetilde{y}\frac{\partial v}{\partial \xi} + \widetilde{z}\frac{\partial w}{\partial \xi}\right)u + \frac{\partial p}{\partial \xi}\widetilde{x} = 0 \\ \frac{1}{K}\frac{\partial v}{\partial \tau} + (u\widetilde{x} + v\widetilde{y} + w\widetilde{z})\frac{\partial v}{\partial \xi} + \left(\widetilde{x}\frac{\partial u}{\partial \xi} + \widetilde{y}\frac{\partial v}{\partial \xi} + \widetilde{z}\frac{\partial w}{\partial \xi}\right)v + \frac{\partial p}{\partial \xi}\widetilde{y} = 0 \\ \frac{1}{K}\frac{\partial w}{\partial \tau} + (u\widetilde{x} + v\widetilde{y} + w\widetilde{z})\frac{\partial w}{\partial \xi} + \left(\widetilde{x}\frac{\partial u}{\partial \xi} + \widetilde{y}\frac{\partial v}{\partial \xi} + \widetilde{z}\frac{\partial w}{\partial \xi}\right)w + \frac{\partial p}{\partial \xi}\widetilde{z} = 0 \end{cases} \tag{2.31}$$

Where:

$$(\widetilde{x}, \widetilde{y}, \widetilde{z})^T = \left(\frac{1}{K}\frac{\partial \xi}{\partial x}, \frac{1}{K}\frac{\partial \xi}{\partial y}, \frac{1}{K}\frac{\partial \xi}{\partial z}\right)^T \tag{2.32}$$

The advective and viscous fluxes are discretised on the cell centres using the inter cell values, e.g. the inviscid flux derivative in the $\xi-$direction can be defined as:

$$\left(\frac{\partial \mathbf{E_I}}{\partial \xi}\right)_{i,j,k} = \frac{(\mathbf{E_I})_{i+\frac{1}{2},j,k} - (\mathbf{E_I})_{i-\frac{1}{2},j,k}}{\Delta \xi} \tag{2.33}$$

Once the intercell fluxes have been determined, the actual system equations which is numerically integrated are the conservative equations (2.25). In order to formulate the approximate Riemann solver for the problem, we note that the system (2.31) can also be written in matrix-form:

$$\frac{1}{K}\frac{\partial \mathbf{U}}{\partial \tau} + \mathbf{A}\frac{\partial \mathbf{U}}{\partial \xi} = 0 \tag{2.34}$$

Here the matrix $\mathbf{A}$ is given by:

$$\mathbf{A} = \begin{pmatrix} 0 & \widetilde{x} & \widetilde{y} & \widetilde{z} \\ \widetilde{x} & \lambda_0 + \widetilde{x}u & u\widetilde{y} & u\widetilde{z} \\ \widetilde{y} & \widetilde{x}v & \lambda_0 + \widetilde{y}v & v\widetilde{z} \\ \widetilde{z} & \widetilde{x}w & w\widetilde{y} & \lambda_0 + \widetilde{z}w \end{pmatrix} \tag{2.35}$$

Where λ_0 denotes velocity normal to the cell face:

$$\lambda_0 = u\widetilde{x} + v\widetilde{y} + w\widetilde{z} \tag{2.36}$$

The eigenvalues of this matrix are given by λ_0 and $\lambda_\pm$ where:

$$\lambda_\pm = \lambda_{1,2} = \tfrac{1}{2}\lambda_0 \pm s \tag{2.37}$$

The corresponding artificial speed of sound s is defined by:

$$s = \frac{\sqrt{\lambda_0^2 + 4\beta}}{2} \tag{2.38}$$

Following the same derivation procedure as for the original CBS scheme (Drikakis & Durst (1994)), the following solution for the reconstructed variables at the cell face is obtained $(\widetilde{p}, \widetilde{u}, \widetilde{v}, \widetilde{w})^T$.

$$\begin{cases} \widetilde{p} = \frac{1}{\lambda_+ - \lambda_-}\left(p_-\lambda_+ - p_+\lambda_- + \lambda_+\lambda_-\left(R_+ - R_-\right)\right) \\ \widetilde{u} = u_0 + \frac{\widetilde{x}}{(\lambda_+ - \lambda_-)}\left(p_+ - p_- - \lambda_+ R_+ + \lambda_- R_-\right) \\ \widetilde{v} = v_0 + \frac{\widetilde{x}}{(\lambda_+ - \lambda_-)}\left(p_+ - p_- - \lambda_+ R_+ + \lambda_- R_-\right) \\ \widetilde{w} = w_0 + \frac{\widetilde{z}}{(\lambda_+ - \lambda_-)}\left(p_+ - p_- - \lambda_+ R_+ + \lambda_- R_-\right) \end{cases} \tag{2.39}$$

Here R_+ and R_- are the auxiliary functions:

$$\begin{cases} R_+ = \widetilde{x}\,(u_0 - u_+) + \widetilde{y}\,(v_0 - v_+) + \widetilde{z}\,(w_0 - w_+) \\ \\ R_- = \widetilde{x}\,(u_0 - u_-) + \widetilde{y}\,(v_0 - v_-) + \widetilde{z}\,(w_0 - w_-) \end{cases} \tag{2.40}$$

Here the variables $\mathbf{V_{0,\pm}} = (p, u, v, w)^T_{0,\pm}$ are taken either from the left side of the face or right side of the face depending on the sign of the local eigenvalues:

$$\begin{cases} \mathbf{V_0} = \frac{\mathbf{V_L}+\mathbf{V_R}}{2} - \mathrm{sign}\,(\lambda_0)\,\frac{\mathbf{V_R}-\mathbf{V_L}}{2} \\ \mathbf{V}_- = \mathbf{V_R} \\ \mathbf{V}_+ = \mathbf{V_L} \end{cases} \tag{2.41}$$

where $\mathbf{V_{L,R}}$ denotes the data on the left and right side of the cell face respectively.

Temperature behaves effectively as a passive scalar, hence the reconstructed value for the temperature corresponds to the eigenvalue λ_0:

$$\widetilde{T_f} = T_{f0} \tag{2.42}$$

Similarly one may derive the formulas for the other two directions separately. For an in depth review and derivation of the Characteristics Based Scheme (CBS) please see Drikakis & Rider (2005). The approximate Riemann solver operates on the piecewise-constant representation of the variables.

The order of accuracy of the inviscid flux approximation can be increased using a higher order interpolation to reconstruct cell face values $\mathbf{V_{L,R}}$ instead of using the piecewise-constant approximation. The calculation of primitive variables is implemented for the characteristics based scheme using second and third order interpolation. The derivation of the different orders of interpolation is reviewed in Drikakis & Rider (2005).

Consider the one dimensional stencil shown in Figure [2.1], an equidistant grid in computational space and define two states, left and right, for the intercell variables, as follows:

$$\mathbf{V}_{L,i+1/2} = a\mathbf{V}_i - b\mathbf{V}_{i-1} + c\mathbf{V}_{i+1} + d\mathbf{V}_{i+2} \tag{2.43}$$

for the left state, and

$$\mathbf{V}_{R,i+1/2} = a\mathbf{V}_{i+1} - b\mathbf{V}_{i+2} + c\mathbf{V}_i + d\mathbf{V}_{i-1} \tag{2.44}$$

for the right state.

The coefficients a, b, c and d are to be determined. The derivation of first, second and third order reconstruction is presented here and the resulting ILES formulations have been used throughout the cases presented within the following chapters.

Consider the derivative of the characteristic variable at the cell centre for the case of a positive eigenvalue, the result will be analogous if a negative eigenvalue is considered:

$$\left(\frac{\partial \mathbf{V}}{\partial \xi}\right)_i = \mathbf{V}_{L,i+1/2} - \mathbf{V}_{L,i-1/2} \quad = \tag{2.45}$$

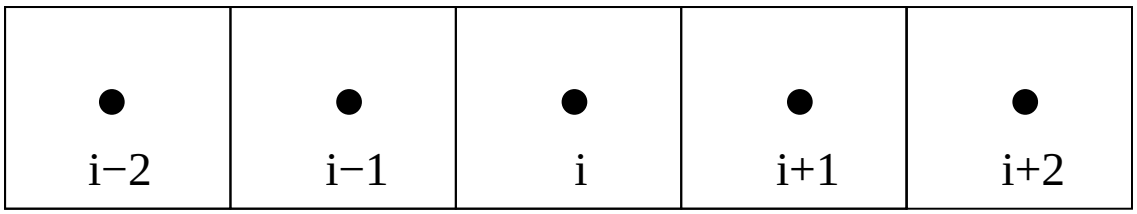

Figure 2.1: One dimensional stencil for deriving the high order reconstruction

$$a\mathbf{V}_i - b\mathbf{V}_{i-1} + c\mathbf{V}_{i+1} + d\mathbf{V}_{i+2} - \quad = \tag{2.46}$$

$$(a\mathbf{V}_{i-1} - b\mathbf{V}_{i-2} + c\mathbf{V}_i + d\mathbf{V}_{i+1}) \tag{2.47}$$

$$(a-c)\mathbf{V}_i - (a+b)\mathbf{V}_{i-1} + b\mathbf{V}_{i-2} \tag{2.48}$$

$$+(c-d)\mathbf{V}_{i+1} + d\mathbf{V}_{i+2} \tag{2.49}$$

By developing all variables in a Taylor series expansion around the cell centre i, (2.45) yields:

$$\left(\frac{\partial \mathbf{V}}{\partial \xi}\right)_i = (a-c)\mathbf{V}_i - \tag{2.50}$$

$$(a+b)\left[\mathbf{V}_i - \mathbf{V}^{(1)} + \mathbf{V}^{(2)} - \mathbf{V}^{(3)} + \mathbf{V}^{(4)}\right] \tag{2.51}$$

$$+b\left[\mathbf{V}_i - 2\mathbf{V}^{(1)} + 4\mathbf{V}^{(2)} - 8\mathbf{V}^{(3)} + 16\mathbf{V}^{(4)}\right] \tag{2.52}$$

$$+(c-d)\left[\mathbf{V}_i + \mathbf{V}^{(1)} + \mathbf{V}^{(2)} + \mathbf{V}^{(3)} + \mathbf{V}^{(4)}\right] \tag{2.53}$$

$$+d\left[\mathbf{V}_i + 2\mathbf{V}^{(1)} + 4\mathbf{V}^{(2)} + 8\mathbf{V}^{(3)} + 16\mathbf{V}^{(4)}\right] \tag{2.54}$$

Here the superscripts denote order of derivatives and the denominators in the Taylor series expansion, these can be omitted and may be considered as an integral part of the unknown coefficients which are yet to be determined.

The grid spacing is considered to be equal to one since we are working in the computational space, therefore equation (2.50) is written as:

$$(\frac{\partial \mathbf{V}}{\partial \xi})_i = (a-b+c+d)^{(1)} + [c-a+3(b+d)]^{(2)} \tag{2.55}$$

$$+[c+a+7(d-b)]\mathbf{V}^{(3)} + [c-a+15(b+d)]\mathbf{V}^{(4)} \tag{2.56}$$

This achieves a first order upwind scheme when:

$$a = 1 \quad \text{and} \quad b = c = d = 0 \tag{2.57}$$

The left and right states of the variables at the cell face are accordingly defined by:

$$\mathbf{V}_{L,i+1/2} = \mathbf{V}_i \quad , \quad \mathbf{V}_{R,i+1/2} = \mathbf{V}_{i+1} \tag{2.58}$$

The second order scheme may be obtained for:

$$a = b = 1 \quad \text{and} \quad c = d = 0 \tag{2.59}$$

For satisfying the Courant Friedrichs Lewy (CFL) like restriction, i.e. having the coefficient of the first-order derivative equal to one i.e.:

$$3b - a = 0 \tag{2.60}$$

On eliminating the second order derivative term from (2.55). Using (2.59) and (2.60) the values $a = 3/2$ and $b = 1/2$ are obtained. The left and right states are accordingly defined by:

$$\begin{cases} \mathbf{V}_{L,i+1/2} &= \frac{3}{2}\mathbf{V}_i - \frac{1}{2}\mathbf{V}_{i-1} \\ \\ \mathbf{V}_{R,i+1/2} &= \frac{3}{2}\mathbf{V}_{i+1} - \frac{1}{2}\mathbf{V}_{i+2} \end{cases} \tag{2.61}$$

Finally a third order scheme can be obtained when $d = 0$, the CFL like restriction is imposed:

$$a - b + c = 1 \tag{2.62}$$

By the following conditions for eliminating the second and third-order derivative terms from: (2.55)

$$\begin{cases} 3b - a + c &= 0 \\ \\ a - 7b + c &= 0 \end{cases} \tag{2.63}$$

Eqs. (2.62) and (2.63) give the values $a = 5/6, b = 1/6$ and $c = 1/3$. The left and right states are then accordingly defined as:

$$\begin{cases} \mathbf{V}_{L,i+1/2} &= \frac{5}{6}\mathbf{V}_i - \frac{1}{6}\mathbf{V}_{i-1} + \frac{1}{3}\mathbf{V}_{i+1} \\ \\ \mathbf{V}_{R,i+1/2} &= \frac{5}{6}\mathbf{V}_{i+1} - \frac{1}{6}\mathbf{V}_{i+2} + \frac{1}{3}\mathbf{V}_i \end{cases} \tag{2.64}$$

The high resolution methods are based on high-order reconstruction of the inter cell variable values and individually provide unique ILES formulations.

2.2.4 Viscous Fluxes Approximation

Viscous fluxes were calculated using a second order central difference based on cell centred values. This is in keeping with the physics of the partial differential equations since the viscous part of the equations is elliptic and therefore central differencing here is preferred. For example for the viscous flux $\mathbf{E_V}$, (the derivative of the flux) in ξ in the cell centre is given by:

$$\left(\frac{\partial \mathbf{E_V}}{\partial \xi}\right)_{i,j,k} = \frac{(\mathbf{E_V})_{i+\frac{1}{2},j,k} - (\mathbf{E_V})_{i-\frac{1}{2},j,k}}{\Delta\xi} \tag{2.65}$$

where the first derivatives inside the viscous flux are approximated at the cell face using a central difference approximation e.g.:

$$\left(\frac{\partial u}{\partial \xi}\right)_{i+\frac{1}{2},j,k} = \frac{u_{i+1,j,k} - u_{i,j,k}}{\Delta\xi} \tag{2.66}$$

2.2.5 Time Integration

The solution of transient problems requires an update for the velocity time derivative, this is commonly performed by use of a predictor-corrector approach such as Heun's method, or for greater accuracy, higher order methods can be applied.

The time evolution of the system(s) is first order accurate and is performed using a fourth order Runge-Kutta time integration in pseudo time and a first order prediction in real time.

Using superscripts to denote the time level and the Runge-Kutta step, the time integration for pseudo time is defined as:

$$\mathbf{U^1} = \mathbf{U^n} \tag{2.67}$$

$$\mathbf{U^2} = \mathbf{U^n} - \frac{\Delta\tau}{2}\mathbf{RHS}(\mathbf{U^1}) \tag{2.68}$$

$$\mathbf{U^3} = \mathbf{U^n} - \frac{\Delta\tau}{2}\mathbf{RHS}(\mathbf{U^2}) \tag{2.69}$$

$$\mathbf{U^4} = \mathbf{U^n} - \Delta\tau\mathbf{RHS}(\mathbf{U^3}) \tag{2.70}$$

$$\mathbf{U^{n+1}} = \mathbf{U^n} - \frac{\Delta\tau}{6}(\mathbf{RHS}(\mathbf{U^1}) + 2\mathbf{RHS}(\mathbf{U^2}) + 2\mathbf{RHS}(\mathbf{U^3}) + \mathbf{RHS}(\mathbf{U^4})) \tag{2.71}$$

Here **RHS** represents the right-hand side of the Navier-Stokes operator in (2.25).

The time step on each Runge-Kutta iteration is locally defined according to the convergence requirements of the advective part of the Navier-Stokes equations, which is defined as:

$$\Delta\tau_\Omega = \frac{CFL}{\left(\min\left\{\left(\left|\lambda_0, \lambda_1\right|, \left|\lambda_2\right|\right)\right\}\right)_\Omega} \tag{2.72}$$

Here CFL denotes the Courant number, the convergence criteria for the set of conserved variables is satisfied once the solution computed residuals reach a given maximum value. This value was 2.0×10^{-6} for pressure and 1.0×10^{-9} for all velocity components.

Finally the solution is evolved in real time using a first order approximation:

$$\frac{\partial \mathbf{U_r}}{\partial t} = \frac{\mathbf{U_r}^{\mathbf{n+1}} - \mathbf{U_r}^{n}}{\triangle t} \tag{2.73}$$

A constant suitably small real time step has been used throughout the thesis. Unless otherwise stated for a particular case, $\Delta t = 0.01$ has been used by default.

2.3 Postprocessing

In this section we outline the post-processing process applied for various turbulent flow quantities since the procedures used are the same for all turbulent flow cases.

Using operator $< \cdot >$ to denote average in time, we can decompose the velocity vector using the Reynolds decomposition as follows:

$$u =< u > +u^{'} \tag{2.74}$$

$$v =< v > +v^{'} \tag{2.75}$$

$$w =< w > +w^{'} \tag{2.76}$$

Here the $\left(u^{'}, v^{'}, w^{'}\right)^{T}$ vector represents fluctuations of the velocity components.

In theory, the velocity record is continuous and the mean can be evaluated through integration. However, in practice, the velocity signal obtained numerically constitutes a time series of discrete values.

Generally a typical turbulent flow simulation includes two major computation stages:

- Initial development stage - from the start of the computation until time t where the flow is deemed to have developed sufficiently to establish a recurrent

pattern. This point is usually determined by inserting marker points into the flow and analysing the velocity signal obtained at the fixed locations.

- Sampling stage - here the averaging for the velocities and other turbulent quantities is performed using the averaging window $(t, t + t_{av})$. The window is selected based on the analysis of averaged quantities. For a developed flow the averaged quantities do not change if the time window is further increased.

In the time window, t_{av}, the averaged signal for velocity u, for example, is given by:

$$< u >= \frac{1}{t_{av}} \sum_{t}^{t_{av}+t} u^n \Delta t^n \tag{2.77}$$

Where the summation runs over the sampling interval from the time step corresponding from t to the time step corresponding to $t + t_{av}$.

The turbulent fluctuations component is presented in the form of turbulence strength, this is the Root Mean Square (RMS) value of the fluctuating velocity component. It is defined as the standard deviation of the set of random fluctuations, e.g. for u:

$$u_{RMS} = \left(\frac{1}{t_{av}} \sum_{t}^{t_{av}+t} (u^n - < u >)^2 \Delta t^n \right)^{0.5} \tag{2.78}$$

The cross-components of the Reynolds stress tensor are computed similarly, e.g.:

$$< u^{'} v^{'} >= \frac{1}{t_{av}} \sum_{t}^{t_{av}+t} (u^n - < u >)(v^n - < v >) \Delta t^n \tag{2.79}$$

Further information regarding the ensemble properties may be found in various textbooks along with other high order statistics as in Pope (2000).

For the lid-driven validation case, the fluctuating streamwise component was also used in order to obtain the power spectra. This was calculated using a Discrete Fourier Transform (DFT), i.e. with "fft" function in MatlabR2007b.

The result of the computation is presented on Log-Log scales in order to provide suitable comparison with the experiment.

The distance from the wall to the first grid cell centre in terms of wall units is also presented in the results. Assuming, with dimensions (for the moment), y^* to be the direction normal to the wall, we can define the viscous length y^*_τ (e.g. Pope (2000)) as:

$$y^*_\tau = \frac{\nu^* \sqrt{\rho^*}}{\sqrt{\tau^*_w}} \tag{2.80}$$

Where τ^*_w denotes the shear stress at the wall. The non-dimensional distance in terms of the viscous length is then given by:

$$y^+ = \frac{y^*}{y^*_\tau} = \frac{y^* \sqrt{\tau^*_w}}{\nu^* \sqrt{\rho^*}} = \frac{y^*}{\nu^* \sqrt{\rho^*}} \sqrt{\mu^* \frac{\partial u^*_{||}}{\partial n^*}}, \tag{2.81}$$

Where $u^*_{||}$ is the component of the velocity tangential to the wall and n^* indicates the direction normal to the wall. On extracting the non-dimensional compounds in the above equation, one obtains the link between the non-dimensional wall-normal coordinate in terms of the viscous length and characteristic length:

$$y^+ = y^* \sqrt{Re \frac{\partial u_{||}}{\partial n}} \tag{2.82}$$

The partial derivative in the wall normal direction in the above equation has to be evaluated numerically with suitable accuracy. For example using the first order approximation, we obtain the following expression for the y^+ corresponding to the first cell centre from the wall:

$$y^+ = \sqrt{\frac{Re \Delta y \sqrt{u^2 + w^2}}{2}} \tag{2.83}$$

2.4 Pressure Forcing for Hypervapotrons

In this section the derivation of the pressure forcing term for an arbitrary geometry is summarised. In order to preserve correct mass flux through the domain and achieve homogeneity in the streamwise direction a body force may be introduced Lenormand & Sagaut (2000). The time evolution equation for the mass flux in this case may be calculated by operating on the streamwise component of velocity i.e. streamwise averaging and integrating over the whole domain the streamwise velocity component. The method suggested by Lenormand & Sagaut (2000) was derived for a plane channel flow. In the following section the forcing term for the Hypervapotron model in the developed flow region is derived. The approach and methods provided here are applicable to an arbitrary geometry provided that the model itself is periodic in both the streamwise and spanwise directions. Introduction of end walls only result in an additional stress term to be determined and therefore the philosophy used here may be directly extended to duct models of any shape. However, the formulation presented assumes periodicity of geometry in the streamwise direction and no end walls present. We begin the derivation by considering the streamwise component of the momentum equation:

$$\frac{\partial u}{\partial t} = -\frac{\partial (u^2 + p)}{\partial x} - \frac{\partial vu}{\partial y} - \frac{\partial wu}{\partial z} + \frac{\partial \tau_{xx}}{\partial x} + \frac{\partial \tau_{yx}}{\partial y} + \frac{\partial \tau_{zx}}{\partial z} \tag{2.84}$$

Assuming that the inlets and outlets are in the x direction we can integrate the above in the complete domain leading to:

$$\frac{\partial G}{\partial t} = \frac{1}{L_x} \int\int\int \left(-\frac{\partial (u^2 + p)}{\partial x} - \frac{\partial vu}{\partial y} - \frac{\partial wu}{\partial z} + \frac{\partial \tau_{xx}}{\partial x} + \frac{\partial \tau_{yx}}{\partial y} + \frac{\partial \tau_{zx}}{\partial z} \right) dV \tag{2.85}$$

where

$$G = \int\int udzdy \tag{2.86}$$

is the volume flow rate in the cross section and τ_{ij} are the components of the shear stress tensor and L_x is the size of the domain in x. By considering the shear stresses we may write:

$$\frac{\partial \tau_{xx}}{\partial x} + \frac{\partial \tau_{yx}}{\partial y} + \frac{\partial \tau_{zx}}{\partial z} = \nabla \cdot \mathbf{D} \tag{2.87}$$

Here $\mathbf{D}$ is defined as a vector:

$$\mathbf{D} = (\tau_{xx}, \tau_{yx}, \tau_{zx})^T \tag{2.88}$$

Therefore we may write:

$$\frac{1}{L_x} \int\int\int (\nabla \cdot \mathbf{D})\, dV = \frac{1}{L_x} \int\int (\mathbf{D} \cdot \mathbf{n})\, dS \tag{2.89}$$

Here $\mathbf{n}$ is the outward normal vector to the bounding surface S. The integral sum over the control faces is given by:

$$\frac{1}{L_x} \int\int (\mathbf{D} \cdot \mathbf{n})\, dS_i = \frac{1}{L_x} \sum_{i=1}^{n} \int\int (\tau_{xx} n_x + \tau_{yx} n_y + \tau_{zx} n_z)\, dS_i \tag{2.90}$$

Here dS_i is defined as the set of face elements. Further let us decompose the pressure into two terms, one being the periodic part and the other representing the linear pressure drop:

$$p = p_p + f \cdot x \tag{2.91}$$

In the momentum conservation law the divergence of the following vectors can be identified:

$$\mathbf{E_u} = \left(u^2, vu, wu\right)^T \tag{2.92}$$

$$\mathbf{E_p} = (p_p, 0, 0)^T \tag{2.93}$$

$$\mathbf{E_l} = (f \cdot x, 0, 0)^T \tag{2.94}$$

Corresponding to the convective flux, periodic and linear parts of the pressure respectively. Similarly applying the divergence theorem, these can be converted into surface integrals. By considering the convective flux we obtain:

$$-\frac{1}{L_x} \int \int (\mathbf{E_u} \cdot \mathbf{n})\, dS = 0 \tag{2.95}$$

The contribution to this integral from the wall boundaries is zero due to the no-slip condition. Contribution from the opposing periodic boundaries is zero because of the periodicity. Therefore the contribution to the volume flow rate from convective flux is analytically derived to be zero.

Contribution from the periodic pressure component is nullified on the periodic boundaries but is not necessarily zero at solid walls unless $n_x = 0$, hence we need to take it into account:

$$-\frac{1}{L_x} \int \int (\mathbf{E_p} \cdot \mathbf{n})\, dS_i = -\frac{1}{L_x} \int \int p n_x dS \neq 0 \tag{2.96}$$

This term can be incorporated into the integral of stresses to yield:

$$\frac{1}{L_x} \sum_{i=1}^{n} \int \int \left((\tau_{xx} - p)\, n_x + \tau_{yx} n_y + \tau_{zx} n_z\right) dS \tag{2.97}$$

Or by expanding the stress tensor we may write:

$$\frac{1}{ReL_x}\sum_{i=1}^{n}\int\int\left(\left(2\frac{\partial u}{\partial x}-p\cdot Re\right)n_x+\left(\frac{\partial u}{\partial y}+\frac{\partial v}{\partial x}\right)n_y+\left(\frac{\partial u}{\partial z}+\frac{\partial w}{\partial x}\right)n_z\right)dS \quad (2.98)$$

Finally the integral corresponding to the linear pressure contribution can be calculated explicitly as:

$$-\frac{1}{L_x}\int\int\int(\nabla\mathbf{E_l})dV=-\frac{f}{L_x}V \quad (2.99)$$

The equation for the rate of mass flux can then be written as:

$$\frac{dG}{dt}=\frac{f}{L_x}V+\frac{1}{L_x}\sum_{i=1}^{n}\int\int\left(\left(\tau_{xx}-p\right)n_x+\tau_{yx}n_y+\tau_{zx}n_z\right)dS_i \quad (2.100)$$

Here the sum is taken over all boundaries of the domain. Discretising the above in time we obtain the update formula for the mass flux:

$$G^{n+1}=G^n-\Delta\tau\left(f^n\frac{V}{L_x}-\frac{1}{L_x}\sum_{i=1}^{n}\int\int\left(\left(\tau_{xx}-p\right)n_x+\tau_{yx}n_y+\tau_{zx}n_z\right)dS_i\right) \quad (2.101)$$

Finally the calculation of the pressure forcing term f is performed using a (first order) Euler correction given by Lenormand & Sagaut (2000):

$$f^{n+1}=f^n+\frac{1}{L_xL_z}\left(C_1\left(G^{n+1}-G_{ideal}\right)+C_2\left(G^n-G_{ideal}\right)\right) \quad (2.102)$$

Here both C_1 and C_2 are relaxation constants to provide faster convergence during the iteration cycles. The value of C_1 and C_2 during all cases was 2.0 and -0.2 respectively.

2.5 Approximation of Conjugate Heat Transfer Boundary Condition

Thermal boundary conditions at the solid-fluid interface, see Figure [2.2], can be obtained from applying a surface energy balance. The temperature is continuous at the interface and therefore:

$$T_s = T_f = T_w \tag{2.103}$$

where the subscript "w" is used to refer to the wall quantities. At the solid-fluid interface the flux boundary conditions are not easily defined and implementation of the constraints is somewhat more perplexing. The curvature at the cavity walls introduces an additional complication since the cell locations on either side of the interface are not necessarily perpendicular to the wall surface. Since the heat flux is defined through the wall normal direction the boundary condition at the interface is resolved by applying the derivative in the wall normal direction of the temperature at the interface.

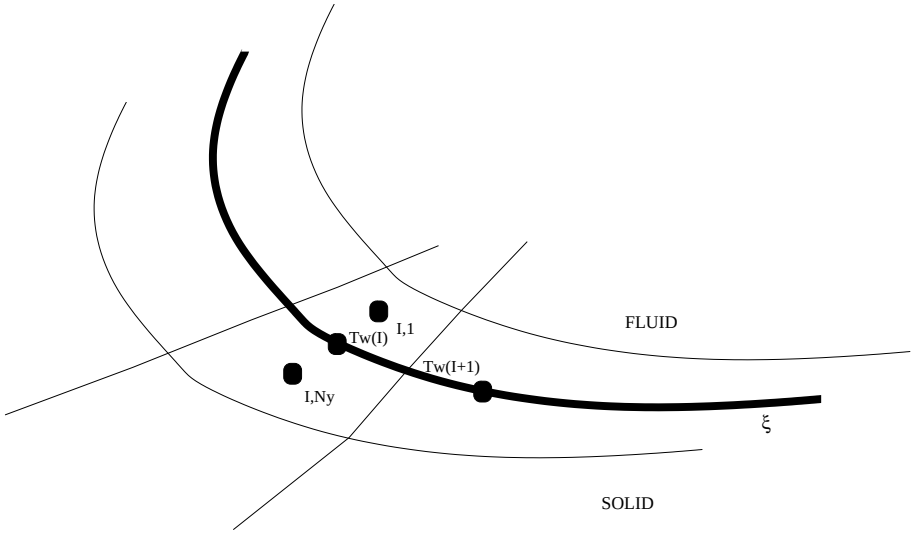

Figure 2.2: Close up view of the grid at the solid-fluid interface for the Hypervapotron cases.

$$k_s \frac{\partial T_s}{\partial \mathbf{n}} - k_f \frac{\partial T_f}{\partial \mathbf{n}} = 0 \tag{2.104}$$

We begin the boundary condition derivation by considering the direct application of the directional derivative for the temperature variable at the interface by using the surrounding cell centre values from both the solid and fluid regions. In two dimensions the equations are more easily derived. Consider the temperature in curvilinear coordinates corresponding to the grid lines $T_{s,f} = f_{s,f}(\xi, \eta)$ as Figure [2.2]. Taking into account the same wall temperature on both sides and the fact that the wall is aligned with ξ, Equation (2.104) implies that at the wall:

$$\left(\frac{\partial T}{\partial \xi}\right)_w cos\theta + \left(\frac{\partial T}{\partial \eta}\right)_s sin\theta = \frac{k_f}{k_s}\left(\left(\frac{\partial T}{\partial \xi}\right)_w cos\theta + \left(\frac{\partial T}{\partial \eta}\right)_f sin\theta\right) \tag{2.105}$$

Here the subscripts of the components of the normal vector have been expanded using the angle θ. While for the grid which is not orthogonal to the wall the above expression will lead to a recurrent relation for wall temperature, for a wall-normal grid, it simplifies to:

$$\left(\frac{\partial T}{\partial \eta}\right)_s = \frac{k_f}{k_s}\left(\frac{\partial T}{\partial \eta}\right)_f \tag{2.106}$$

Approximating the above with first order accuracy we obtain:

$$T_{w,i} = \frac{\frac{k_f}{k_s}\Delta\eta_{s,i} T_{f,i,1} - \Delta\eta_{f,i} T_{s,i,Ny}}{\frac{k_f}{k_s}\Delta\eta_{s,i} - \Delta\eta_{f,i}} \tag{2.107}$$

Once the wall temperature has been calculated the boundary condition in the surrounding ghost cells is defined by extrapolation in both the solid and fluid. The procedure outlined in this section should be valid provided the simulation is wall resolved, otherwise the approximation of the wall normal derivatives used in Equation (2.107 and 2.104) becomes inadequate.

Chapter 3

ILES Validation of a Cubical Cavity Flow using High Order Methods

3.1 Introduction

The lid driven cavity is an idealisation of several fluid mechanics problems. Much of the flow dynamics that appear in a lid driven cavity is also found between the fins within Hypervapotron main section. Although the lid driven cavity is a more simplistic problem, it may be noted that the flow physics present are sufficiently challenging. The flow field exhibits many phenomena which are particularly relevant to the problem in hand. It may be described as a viscous Newtonian incompressible flow and when considered beyond the critical Reynolds number will exhibit inhomogeneous, anisotropic, turbulent behaviour.

With respect to numerical and analytical studies, the first work of this kind originated from Burggraf (1966). The investigation considered the laminar regime up to

400. Further studies in this area were conducted using numerical methods including, vorticity-stream function formulations Ghia *et al.* (1982), Bruneau & Jouron (1990), with the most comprehensive work of the two dimensional case being provided by Barragy & Carey (1997). Analytical and numerical methods have also been used to investigate the stability regime within a lid driven cavity flow Ramanan & Homsy (1994).

Three dimensional lid driven cavity flows have received less attention than the two dimensional counterpart. This may be due to the computational expense and limitations of less versatile solvers. Within the three dimensional problem, additional vortices in the spanwise plane known as Taylor Görtler-Like (TGL) vortices are present. This phenomena has been investigated with success by Zang *et al.* (1993), Jordan & Ragab (1994a) and Jordan & Ragab (1994b) in the testing of sub-grid scale models for conventional LES methods. Within Habisreuting *et al.* (2007) LES has been applied to gain turbulent data using other SGS models. The most accurate and reliable numerical studies have been the DNS conducted by Verstappen *et al.* (1994), Leriche & Gavrilakis (2000) and Leriche (2006) where in the latter, Reynolds numbers up to 20000 have been considered.

The lid driven case may be considered to be a useful validation tool as verified benchmark data is available from laminar to low turbulent Reynolds number regimes. This is partially due to the well posed boundary conditions for the lid driven cavity flow. In fact, many numerical methods have been benchmarked using the lid driven problem, see Deville *et al.* (1992) for discussion in this context.

Much useful experimental data has been acquired with a Reynolds number limited to 10000. Much of this work has been due to Koseff and others, the most reliable of which has been Prasad & Koseff (1989). Within the article, experimental data included turbulent quantities along centrelines in the symmetry plane. The turbulent behaviour of the time traces demonstrated the presence of the sub-inertial

range when power spectrum was computed. Insight into the lid driven problem incorporating extensive turbulent data was also achieved by Deshpande & Milton (1998). Within this study numerical methods were applied to identify energy spectra, the Kolomogrov scale and dissipation rates which are present in the problem (with Re=10000).

This is the first study of the lid driven cavity flow using ILES available in the literature. The ability of ILES to resolve strong recirculating flows in a wall bounded domain is established here. The impact of high order reconstruction, grid resolution and velocity profile (regularised and uniform) is investigated in the following sections.

3.2 Problem Description

All sides are equal in length, defining a cubical cavity domain. The main flow features in the lid driven problem are illustrated in Figure [3.1]. This schematic outlines the basic flow features and locations of them in the $y - z$ plane for reader reference. Several different types of flow phenomena are present in the turbulent, three dimensional problem. Secondary flow structures, i.e. vortices, are located in the corners of the cavities. TGL vortex pairs occur periodically in the flow as counter rotating structures along the cavity base in the streamwise plane. A flow schematic corresponding to the computational model is shown in Figure [3.2]. In this figure Lines A and B denote the positions where experimental data was obtained in the study by Prasad & Koseff (1989).

The flow field is characterised by a large primary vortex driven by the shear motion of the moving upper boundary. The dimensionless Reynolds number is calculated using the lid velocity, and cavity width.

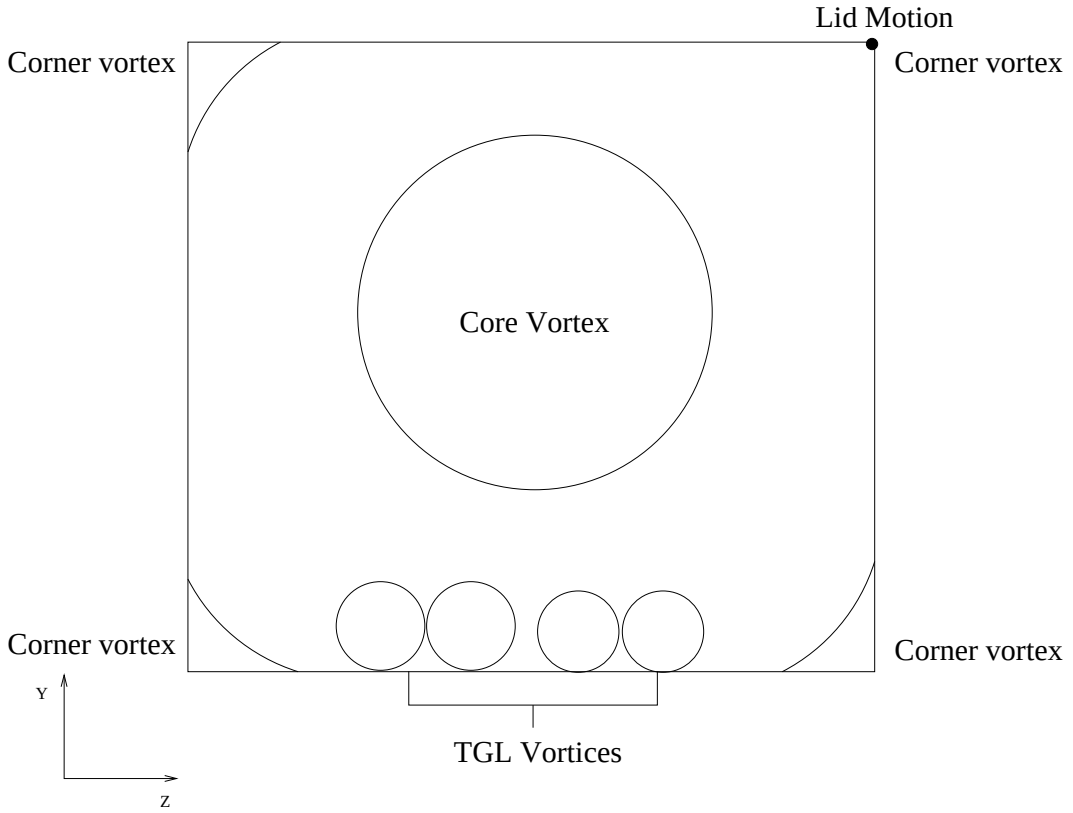

Figure 3.1: Flow structure in the spanwise plane for a cubical lid driven cavity with Re=10000.

The experimental data provided from LDA measurements Prasad & Koseff (1989) is the basis of comparison for two Reynolds numbers, 3200 and 10000. Computations are reported in the following sections and three different grid resolutions are considered. The grids comprised N, $\frac{3}{2}N$ and $2N$ cells where $N = 32$. Therefore the grid rersolutions were 32^3, 48^3 and 64^3, providing 32,768, 110,592, 262,144 nodes respectively. The distribution of points was determined based on wall clustering. The grid node locations were defined using the one dimensional stretching technique initially proposed by Roberts (1971), modified later by Eiseman (1979). For the uniform grid in y covering the domain $[0, 1]$, for example, the stretched grid positions y_1 are given by the transformation:

$$y_1 = ay + (1 - ay)\left(1 - \frac{\texttt{tanh}\,(b(1-y))}{\texttt{tanh}\,(b)}\right) \tag{3.1}$$

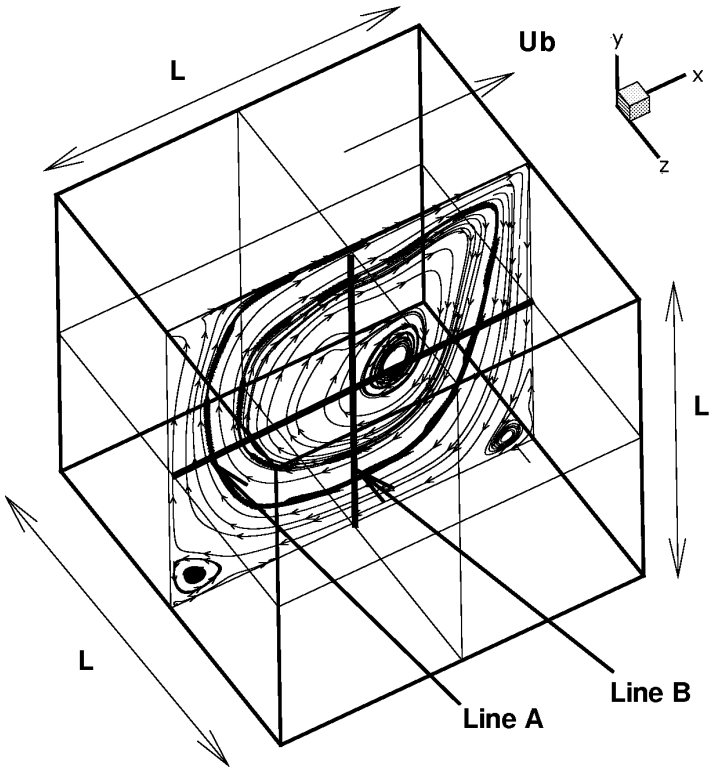

Figure 3.2: Computational domain for the lid driven cube. Here U_b denotes the velocity of the cavity lid.

where a and b are parameters to control point distribution. In this study the values of a and b were, 0.15 and 1.95 respectively. The resulting grids are shown in Figures [3.3] and [3.4].

The main rationale behind limiting the grid size to 64 cells per direction is that in the actual Hypervapotron geometry this was deemed to be the resolution which can be employed per unit volume without leading to the grids which will not be manageable from the computational time point of view.

This investigation also provides confidence in the numerical methods used (i.e. fluid flow solver) and in particular the capability to resolve large recirculating structures in the flow field. The simulations presented intend to highlight that reasonably coarse grids can be used (in conjunction with high resolution methods) to achieve suitable approximation of the key mean and fluctuating features.

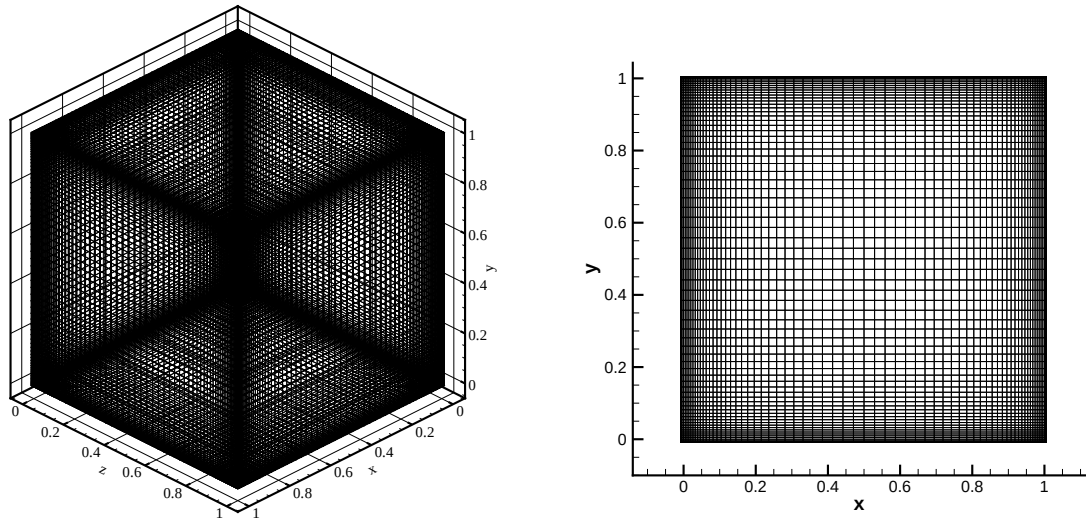

(a) Isometric view of 64^3 grid.

(b) Two dimensional planar view of 64^3 grid.

Figure 3.3: Two and three dimensional views of the 64^3 grid in the lid driven cavity cases.

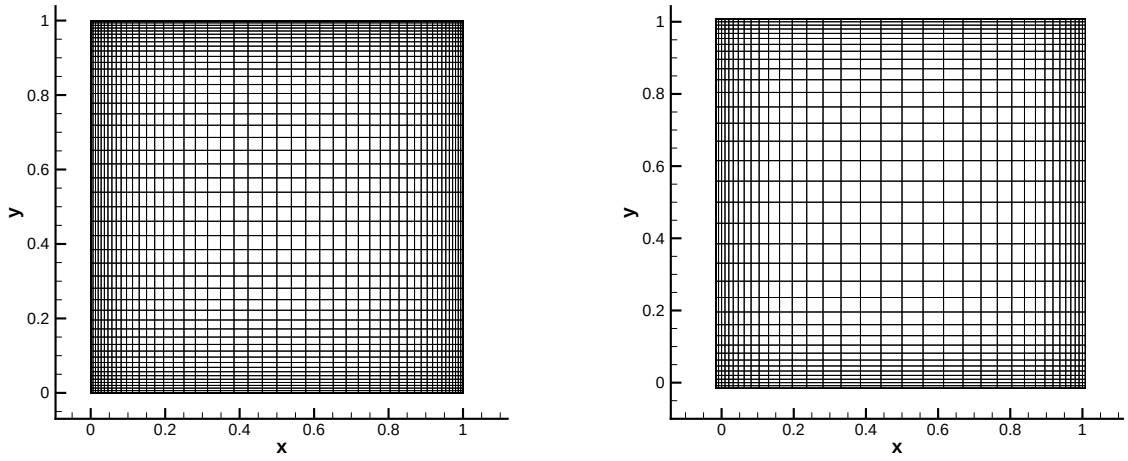

(a) Two dimensional planar view of 48^3 grid.

(b) Two dimensional planar view of 32^3 grid.

Figure 3.4: Two dimensional planar views of the 48^3 and 32^3 grids in the lid driven cavity cases.

3.2.1 Initial and Boundary Conditions

The physical system is subject to the following initial and boundary conditions. The initial condition is defined at time $t = t_0$, for all stationary walls (i.e. except for the lid surface,) the following constraint holds.

$$u = v = w = 0 \tag{3.2}$$

At the lid surface we define the uniform velocity profile as:

$$u = 1, v = 0, w = 0 \tag{3.3}$$

Simulation using the recently proposed Leriche & Gavrilakis (2000) regularised profile is also included and the boundary condition at the lid surface in these cases is described by (the domain in the cited study used a coordinate axis system that was defined from -1 to 1 for each axis):

$$u(x, z) = a \cdot \left(1 - (2x - 1)^{18}\right)^2 \cdot \left(1 - (2z - 1)^{18}\right)^2 \tag{3.4}$$

In the case where the regularised profile is used, the constant a, which gives the maximum velocity in the above distribution, is determined by requiring the same integral of velocity as for the constant lid velocity case. This yields a Reynolds number of approximately 12000 with velocity normalised by the maximum in the distribution.

Application of the regularised profile eliminates the singularity which is present with a uniform profile. Further, it was found that this boundary conditon accelerated convergence.

3.3 Results and Discussion

3.3.1 Statistics and General Flow Description

In order to establish the flow development and accumulate average data on the reporting lines, point markers in the flow were initially considered. Instantaneous and fluctuating velocities have been recorded at a fixed point in space. The data was acquired approximately 5mm from the lower wall upon the reporting Line B. The time traces have been reported so that useful comparison of the data could be made against the available experimental case Prasad & Koseff (1989).

The time windows used in the simulations were identical for each case. Following the initial development stage of (approximately) 30 dimensionless time units, 200 dimensionless time units were found sufficient to establish converged turbulent statistics. The ensemble averages were accrued within this time window.

The examples of time trace averaging windows are shown in Figures [3.5]-[3.6], for the u and v components respectively. The instantaneous velocity in the first order scheme seems to be taking a lower mean value of the other reconstructions. The time trace indicates a laminar solution for the given cell centre and the second and third order methods both exhibit random fluctuations at relativity high frequencies in comparison.

This suggests in order to capture turbulence in the flow field solution, high order reconstruction of the cell face variables was a requirement (based on current grids).

Comparing the behaviour of time traces for different reconstruction schemes with that for different grids shown in Figure [3.7], it is clear that the increase in the order of accuracy yields changes in the flow behaviour similar to these resulting from the increase of the grid density.

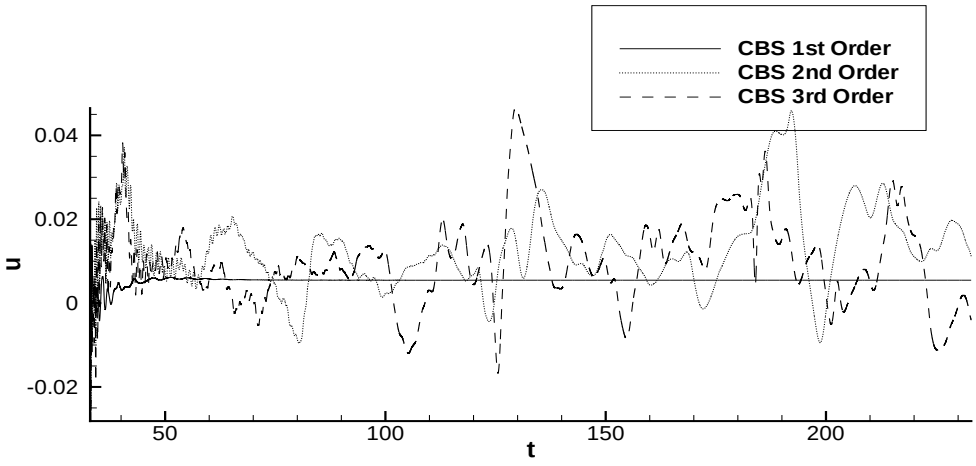

Figure 3.5: Instantaneous u velocity time trace at 5mm from the lower wall surface, with comparison of different reconstruction orders during averaging time period, for Re=10000.

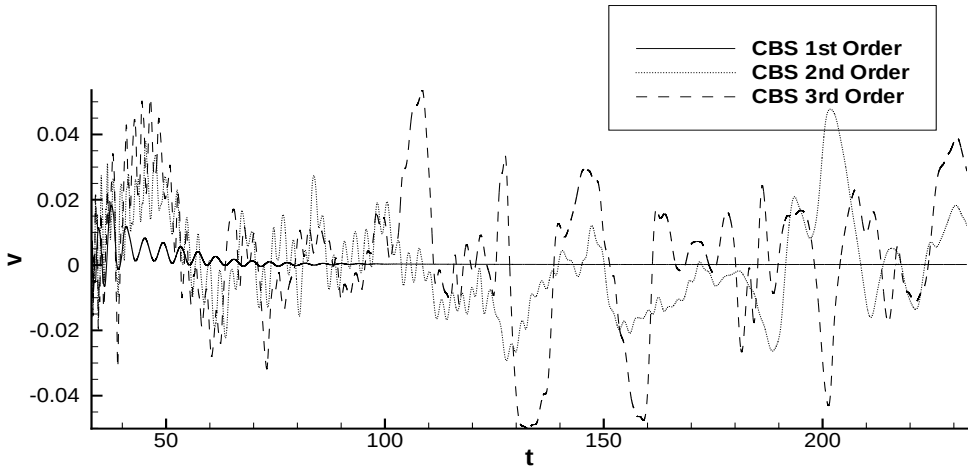

Figure 3.6: Instantaneous u velocity time trace at 5mm from the lower wall surface, with comparison of different reconstruction orders during averaging time period, for Re=10000.

Grid requirements for ILES demand the first grid cell from the wall to have a non-dimensional wall distance of $y+ < 5$.

Although the $y+$ was suggested prior to the computations, the calculated values for $y+$, which are a function of the wall shear stress, were also computed in the post-processing to ensure that the first grid cell from the wall resided in the viscous sublayer.

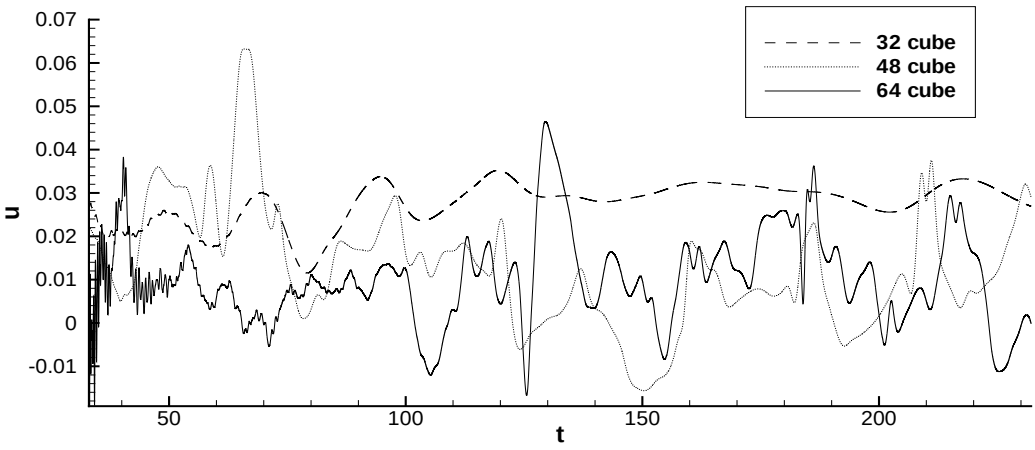

Figure 3.7: Instantaneous u velocity time trace at 5mm from the lower wall surface, with comparison of three different grids and third order reconstruction during averaging time period, for Re=10000.

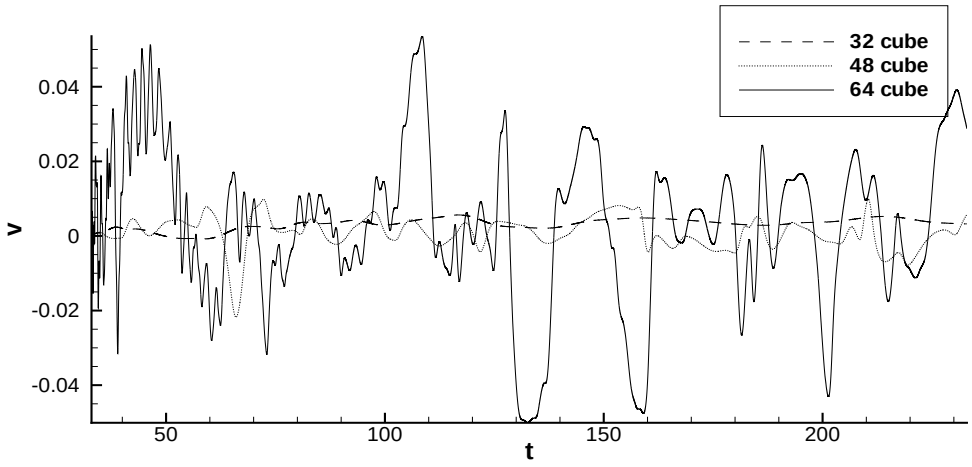

Figure 3.8: Instantaneous v velocity time trace at 5mm from the lower wall, with comparison of third order reconstruction solution on three different grids during averaging time period, for Re=10000.

The Figure [3.9] is a contour plot of the instantaneous distribution of $y+$ values for the first cell centre from the walls for the 64^3 case based on third order reconstruction for the turbulent case with uniform lid velocity.

The average $y+$ for each of the cases was 1, 5 and 10, for the 64^3, 48^3 and 32^3 grids respectively. The region where $y+$ was consistently greatest was at the cavity lid, this was due to the high shear generated by the moving wall.

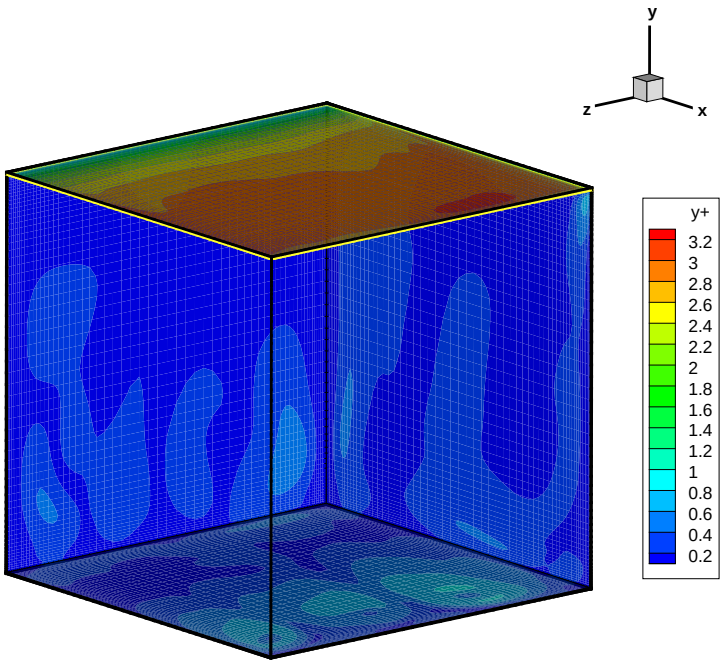

Figure 3.9: Exposed view of $y+$ contours calculated on surfaces at the first cell centre from the cavity interior walls for the 64^3 grid with third order reconstruction for the case with a constant lid velocity, for Re=10000.

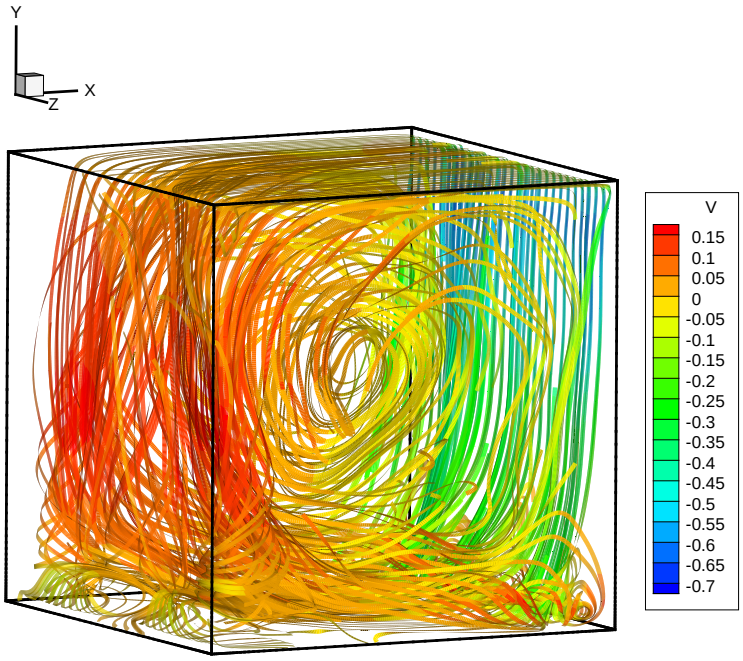

Figure 3.10: Streamribbons with v velocity component contours (superimposed) for the 64^3 grid with third order reconstruction for the case with a constant lid velocity, for Re=10000.

The general flow description presented here for the turbulent flow is based on the 64^3 grid, third order reconstruction and the constant lid velocity boundary condition. The instantaneous trajectories of fluid particles leaving the upper right cavity corner (i.e. $x = 0.975$) are shown in Figure [3.10].

The figure also shows the magnitude of the v velocity component superimposed on to the streamribbons. The streamribbons on the right cavity wall progressively decrease in v velocity from the top to the bottom of the cavity where the fluid impinges on the surface. From this location in the domain the particle trajectories demonstrate a perturbed path line indicating the streamline curvature breakdown to a fully three dimensional flow.

The formation of corner vortices takes place during the flow development stage, all vortices except for the top right corner vortex, remain in the flow field solution once the flow has developed. Figure [3.11] and Figure [3.12] both show the corner vortices in the spanwise plane.

The bottom left cavity vortex appears after the separation point which is located at approximately $x = 0.3$. The bottom right vortex extends from the right wall to approximately $x = 0.8$ The appearance of the TGL vortices is observed clearly at the cavity base at $x = 0.8$ in the $y - z$ planar view, see Figure [3.13]. The TGL vortices arise from centrifugal Görtler instability developing near the separating curved streamline of the primary vortex.

Figure [3.14] shows a close up view of the TGL vortex pair corresponding to those on the left in Figure [3.13]. The location of the TGL vortices corresponds to increase vorticity magnitude in the spatial location. The cavity base, see Figure [3.15], shows peak in vorticity magnitude at $x = 0.8$ due to the TGL vortices. The vorticity contours at the cavity right wall in Figure [3.16] show the high speed primary vortex induced by the moving lid and its breakdown towards the base of the cavity.

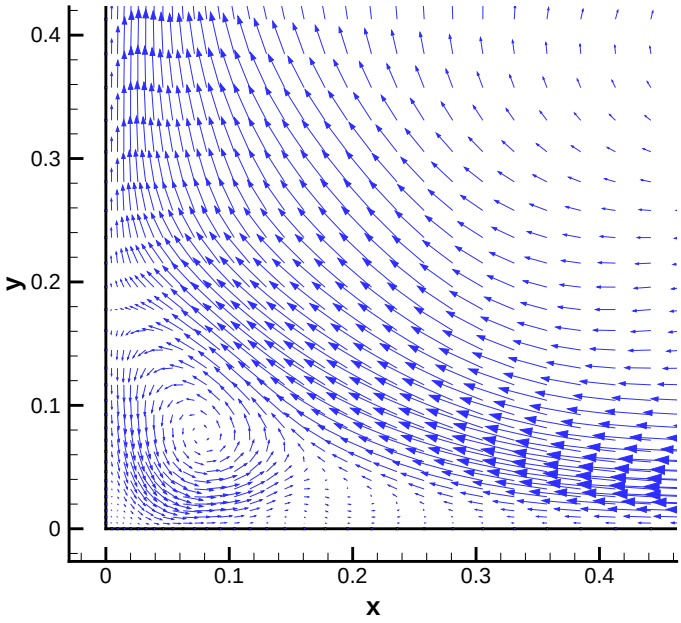

Figure 3.11: Instantaneous velocity vectors of the bottom left corner vortex in the spanwise symmetry plane for 64^3 grid for the third order reconstruction solution with constant lid velocity, for Re=10000.

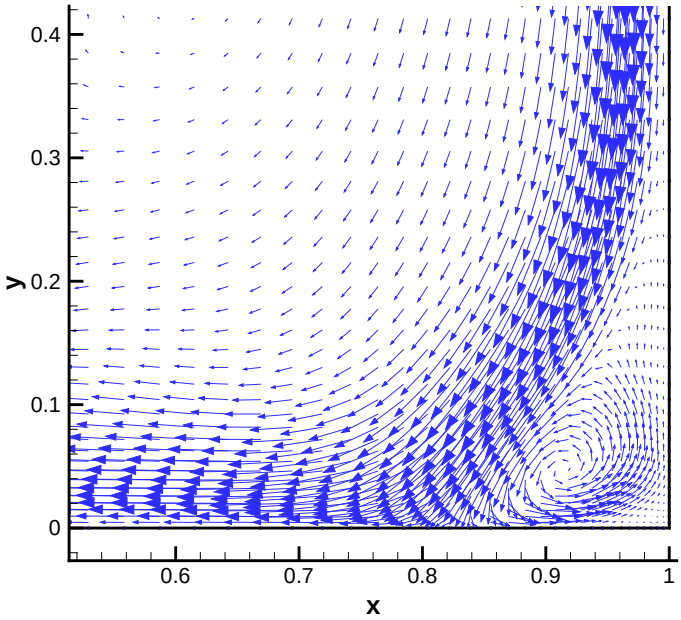

Figure 3.12: Instantaneous velocity vectors of the bottom right corner vortex in the spanwise symmetry plane for 64^3 grid for the third order reconstruction solution with constant lid velocity, for Re=10000.

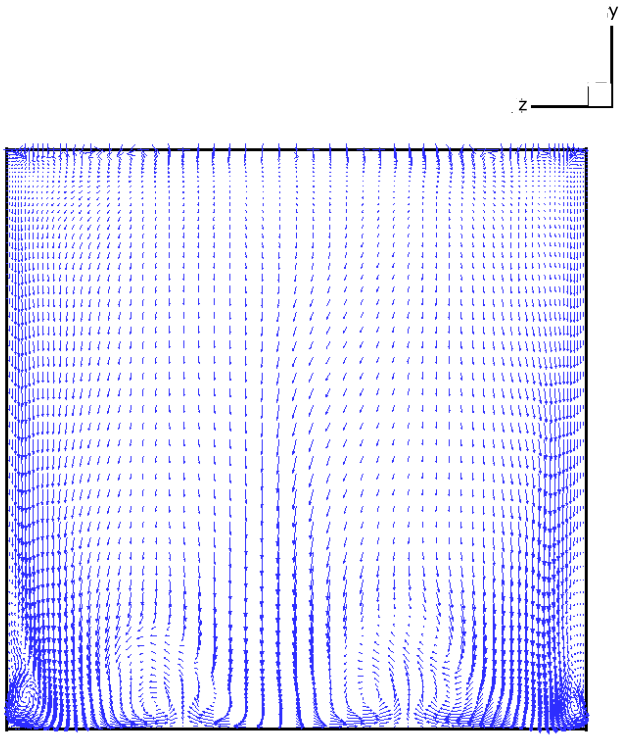

Figure 3.13: $y-z$ planar view of instantaneous velocity vectors showing TGL vortex pairs on the 64^3 grid for the third order reconstruction solution with constant lid velocity, for Re=10000.

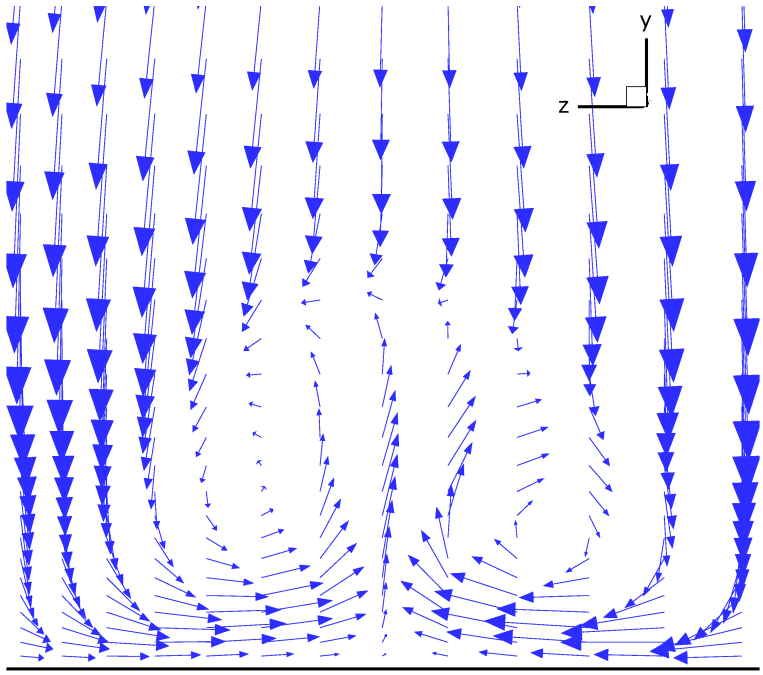

Figure 3.14: $y-z$ planar close-up view of instantaneous velocity vectors showing TGL vortex pair on the 64^3 grid for the third order reconstruction solution with constant lid velocity, for Re=10000.

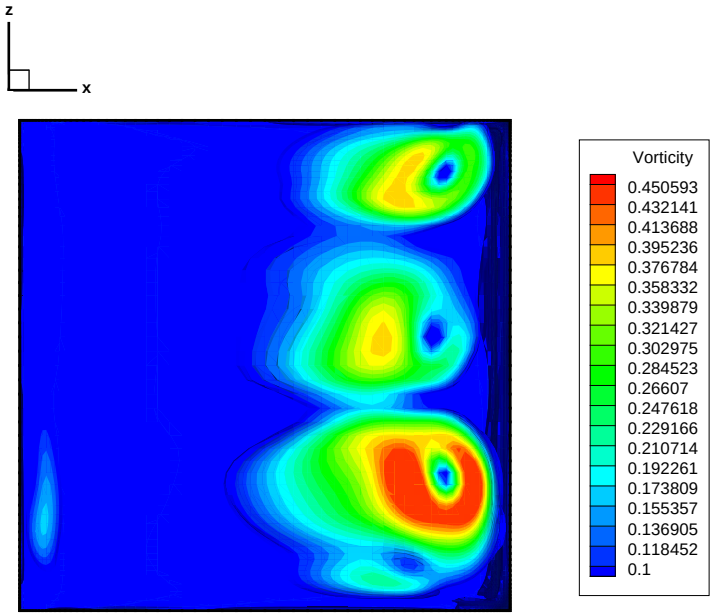

Figure 3.15: Two dimensional view of vorticity (magnitude) iso-surfaces on cavity base for 64^3 grid with third order reconstruction and constant lid velocity, for Re=10000.

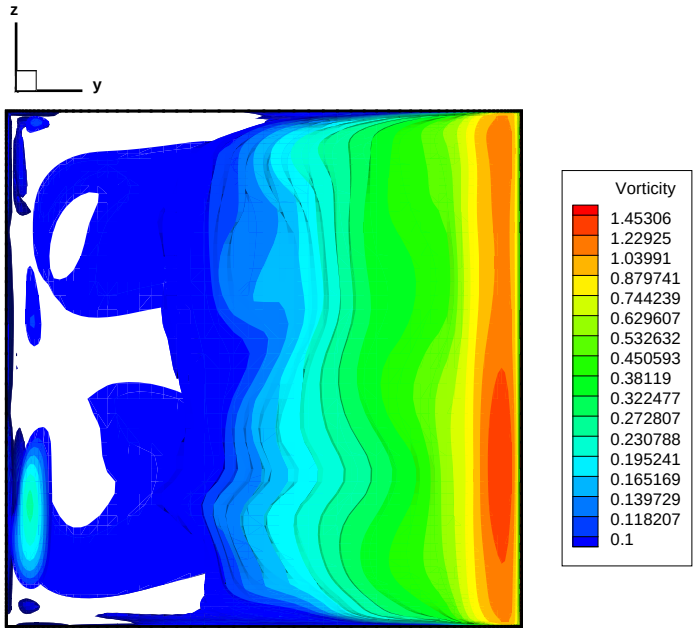

Figure 3.16: Two dimensional view of vorticity (magnitude) iso-surfaces on cavity right wall for 64^3 grid with third order reconstruction and constant lid velocity, for Re=10000.

3.3.2 Results for Measurement Lines

The Re=3200 case was computed by using the steady form of the governing equations. The initial condition for all turbulent cases (were Re=10000) was defined by starting computations with the converged laminar, Re=3200, steady state solution. Figures [3.17] and [3.18] show the corresponding solution computed using third order reconstruction on a 64^3 grid. The velocity components u and v, are shown in comparison with the experimental data on lines B and A respectively.

Comparisons are presented for one component per line as this corresponds to the data provided from measurements performed by Prasad & Koseff (1989). The velocity distribution is captured correctly with the peaks of both components well resolved. The under prediction of the x component of velocity in the middle of the cavity can be due to the strong clustering towards the wall which leads to a relatively coarse grid density in the middle of the cavity.

For the turbulent case (Re=10000), it was felt that recording shear stresses and turbulent quantities throughout the volume in the lid driven case was unnecessary since the experimental validation data does not provide such information. Therefore, averaging was performed on the reporting lines only.

It has been shown that the solution of a lid driven cavity flow may be achieved using high order methods within an ILES framework. The capability of using such a formulation to resolve recirculating flows can be clearly highlighted when drawing comparisons of the accuracy of the results with respect to the experimental validation case Prasad & Koseff (1989).

Presented is both the time averaged ensemble velocity components along Line A and Line B, as per Figure [3.2].

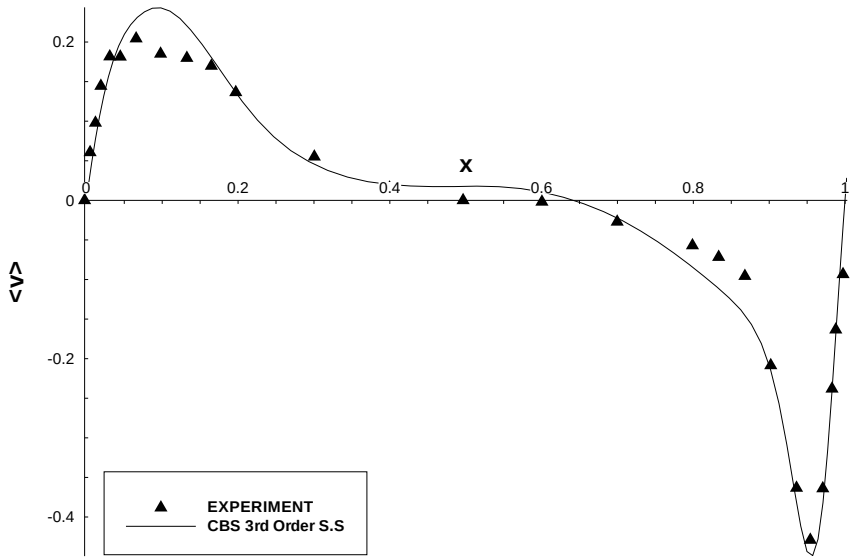

Figure 3.17: Comparison of the v velocity component along Line A on 64^3 grid with experiment (the third order reconstruction solution for Re=3200).

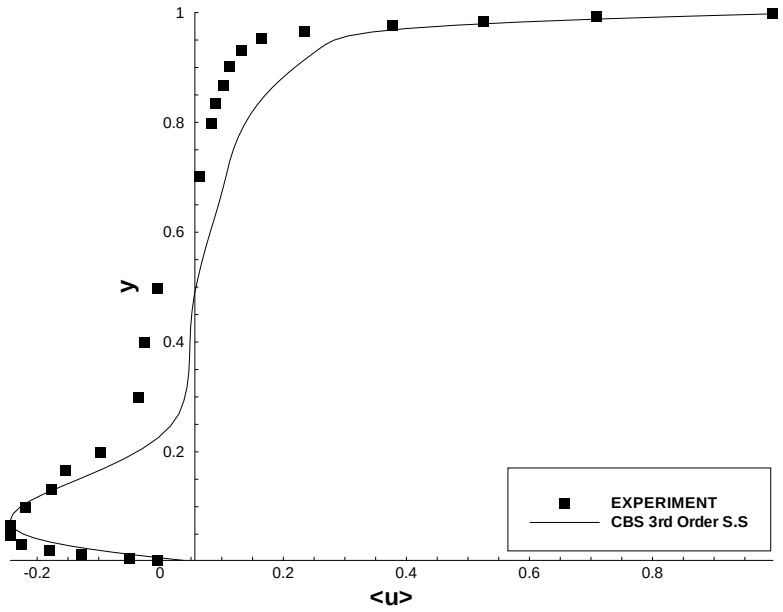

Figure 3.18: Comparison of the u velocity component along Line B on 64^3 grid with experiment (the third order reconstruction solution for Re=3200).

Attention is now turned to the Re=10000 case. The results from the converged cases are presented to demonstrate the solution sensitivity to grid resolution, reconstruction order and the regularised boundary condition. Since the first order results in laminar solution as indicated by the markers in Figure [3.5], only comparison of the second and third order cases is presented in this section. In Figures [3.19] and [3.20] both the Line A and Line B are shown for the 64^3 grid. A large negative peak in $< v >$ along Line A is present close to the right cavity wall. The computed data compares well with the experiment here. The maximum in the $< u >$ component at the base of the cavity is over predicted and this may be due to grid resolution close from the wall being too coarse. However, the reader will note that the third order reconstruction results in closer agreement with the experiment across the Line. However, the comparisons in the middle of the cavity are worse showing the trend similar to that of the laminar case. All the data suggests that the solutions recover the high strain regions of the flow field accurately, such as the lid shear layer and the right cavity wall, but can struggle in more dissipative regions where decaying turbulence may exist.

The regularised profile which had been used in DNS studies and proposed by Leriche & Gavrilakis (2000) has little impact on the flow solution, see Figures [3.21] and [3.22]. The solutions for both the third order regularised and uniform profiles are shown. It seems that although justification exists for employing the boundary condition it has had little impact on the simulations run here. It is suspected that the singularities at the lid corners do not provide the same interference that may arise using spectral methods, however the impact of the boundary condition may be more important depending on grid resolution and reconstruction order. All grids computed may be seen in comparison within Figures [3.23] and [3.24]. The 32^3 case is also shown and it can be suggested from these comparisons that the coarser grids generally do not recover the correct location of the peaks that exist on the centrelines.

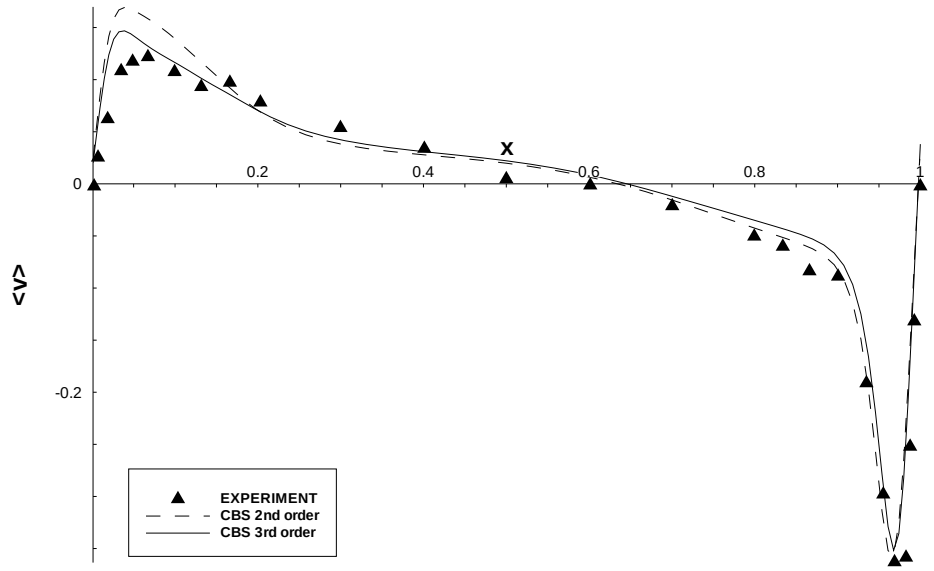

Figure 3.19: Comparison of the ensemble $< v >$ velocity component along Line A on 64^3 grid with different orders of reconstruction for Re=10000.

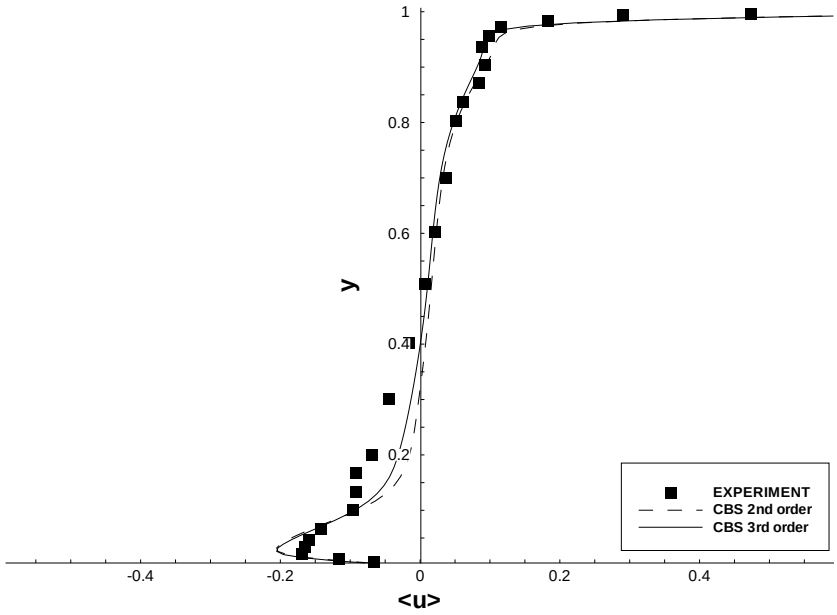

Figure 3.20: Comparison of the ensemble $< u >$ velocity component along Line B on 64^3 grid with different orders of reconstruction for Re=10000.

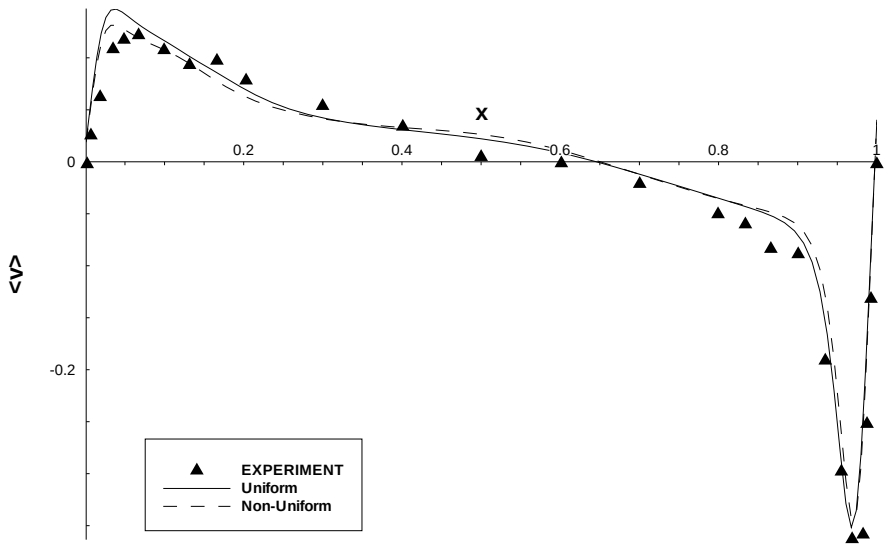

Figure 3.21: Comparison of ensemble $< v >$ velocity component along Line A for uniform and regularised cases on 64^3 grid with third order reconstruction for Re=10000.

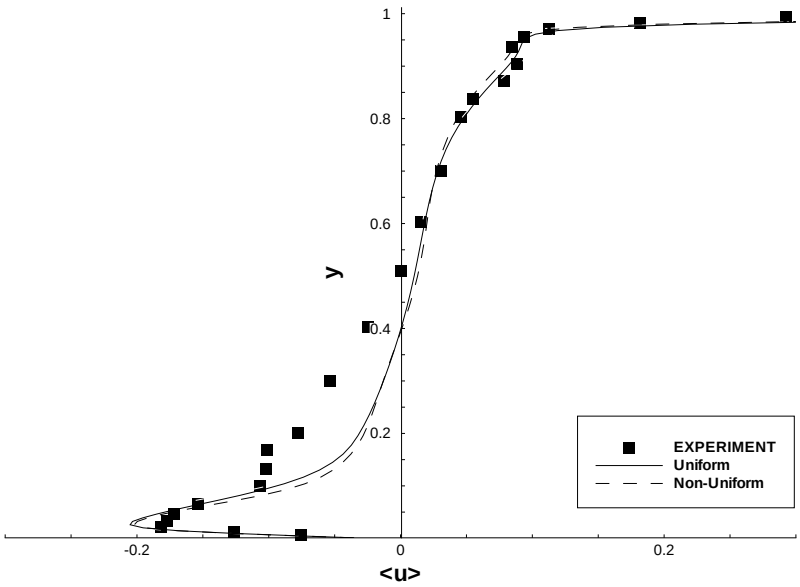

Figure 3.22: Comparison of ensemble $< u >$ velocity component along Line B for uniform and regularised cases on 64^3 grid with third order reconstruction for Re=10000.

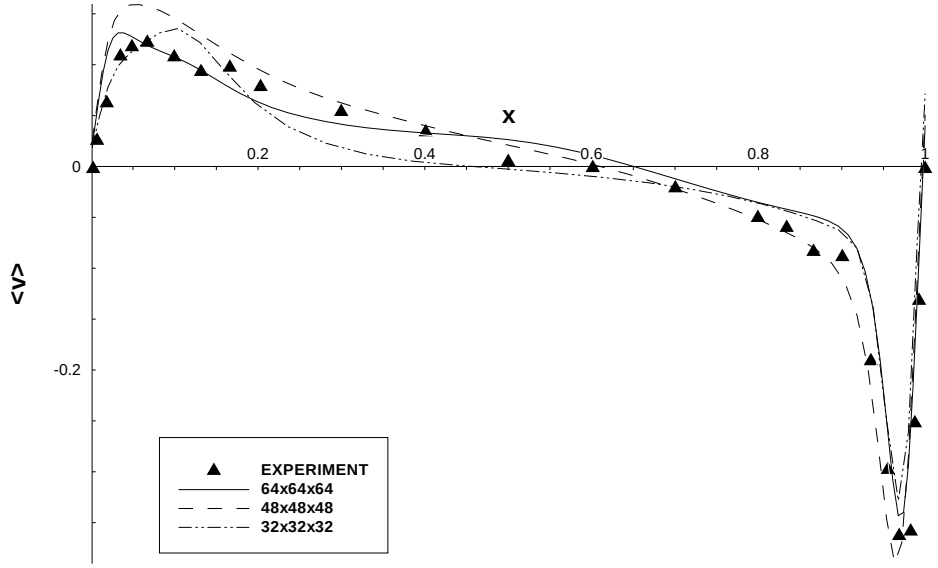

Figure 3.23: Comparison of ensemble $< v >$ velocity component along Line A with different grids with third order reconstruction for Re=10000.

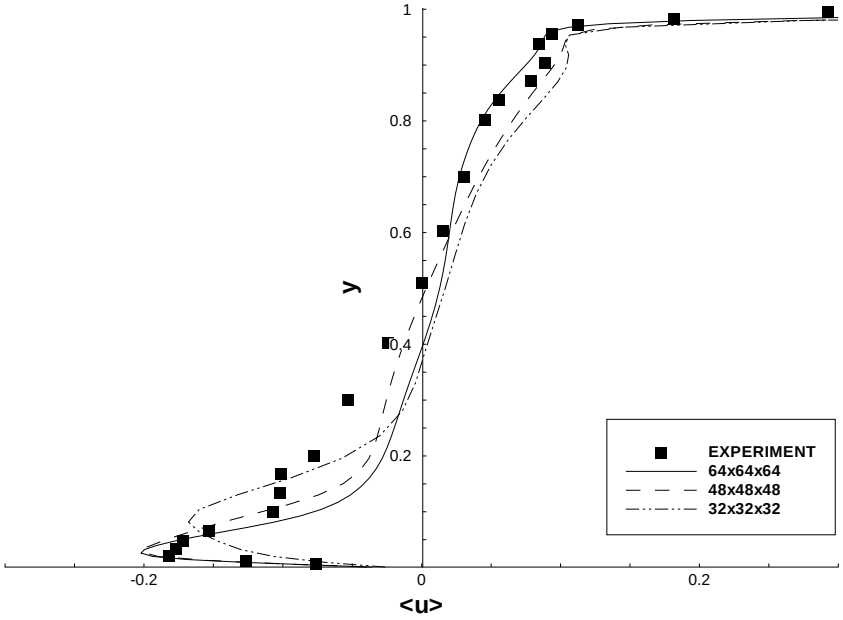

Figure 3.24: Comparison of ensemble $< u >$ velocity component along Line B with different grids with third order reconstruction for Re=10000.

The Figures [3.25]-[3.26] show the RMS of the fluctuating components of velocity for Line A and B. All data has been multiplied by a factor of 10 to enable direct comparison with the figures in the reference experimental study by Prasad & Koseff (1989).

The comparison of the fluctuating components is less favourable, however the same trends are observed. The third order reconstruction provides the best comparison. All data for RMS quantities are under predicted suggesting excessive dissipation may exist in the numerical formulation.

The results obtained are of the same order as the experimental data for the third order reconstruction, see Figures [3.23] and [3.24]. The sensitivity of the solution based on grid resolution for RMS quantities can be seen in Figures [3.27] and [3.28]. It could be argued that with respect to the fluctuating components the second order scheme provides similar accuracy to the third order cases.

The impact of the recently proposed regularised profile is more apparent when considering the fluctuating components, see Figures [3.29] and [3.30]. One may note the magnitude of fluctuating components is generally higher for the uniform case.

It is possible to argue that the presence of the singularity in the uniform velocity boundary condition provides an additional mechanism for the excitation of turbulent flow and the smoothed profile may lead to a more dissipative solution. The results also suggest that the solutions obtained here are far from grid independent.

The under prediction tendency of the data obtained here is comparable with other numerical studies performed for the turbulent case. For example Leriche & Gavrilakis (2000),Verstappen *et al.* (1994) and Deshpande & Milton (1998). In the mentioned investigations, arguments are made to suggest the experiment suffered from poor sampling.

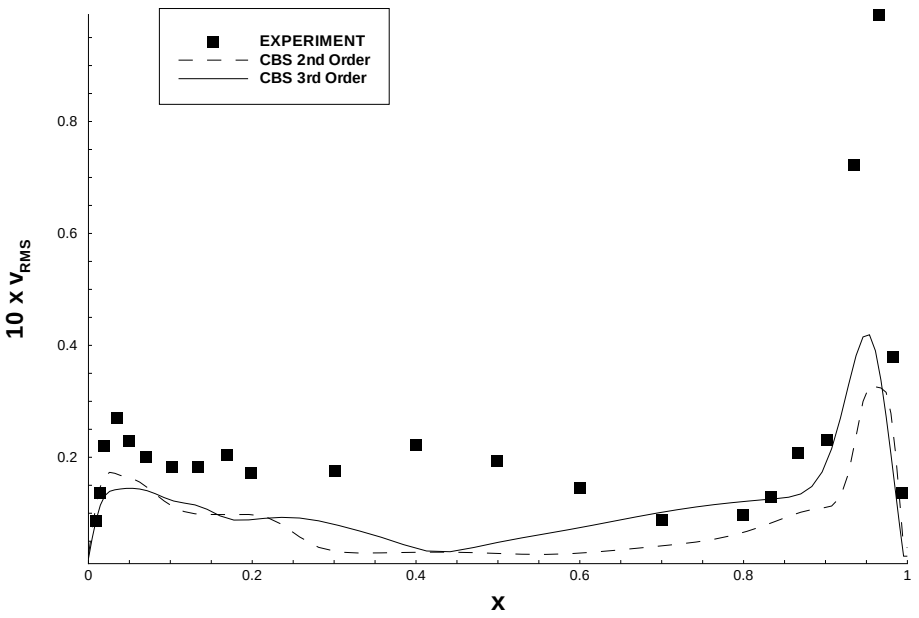

Figure 3.25: Comparison of v_{RMS} velocity component along Line A on 64^3 grid with different orders of reconstruction for Re=10000.

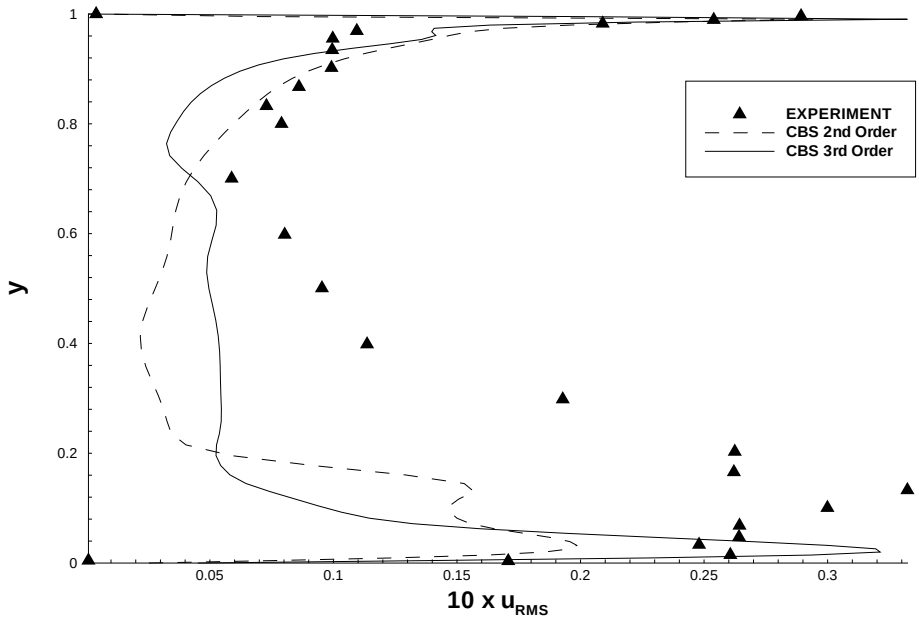

Figure 3.26: Comparison of u_{RMS} velocity component along Line B on 64^3 grid with different orders of reconstruction for Re=10000.

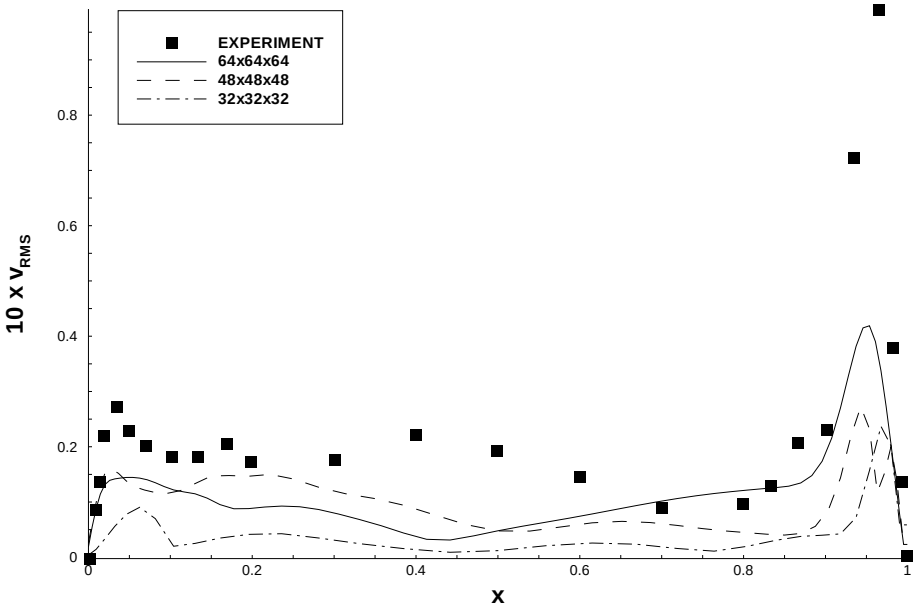

Figure 3.27: Comparison of v_{RMS} velocity component along Line A with different grids and third order reconstruction for Re=10000.

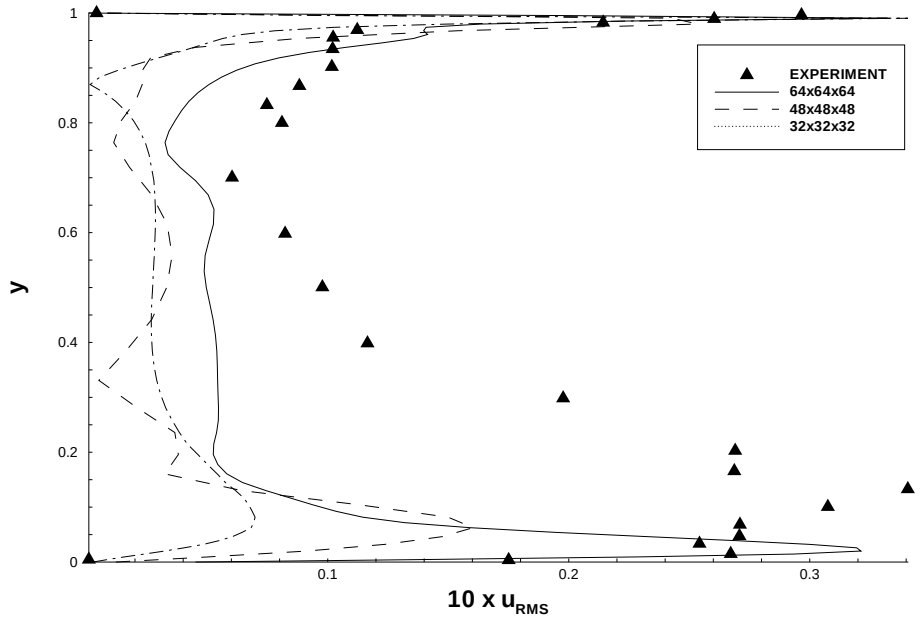

Figure 3.28: Comparison of u_{RMS} velocity component along Line B with different grids and third order reconstruction for Re=10000.

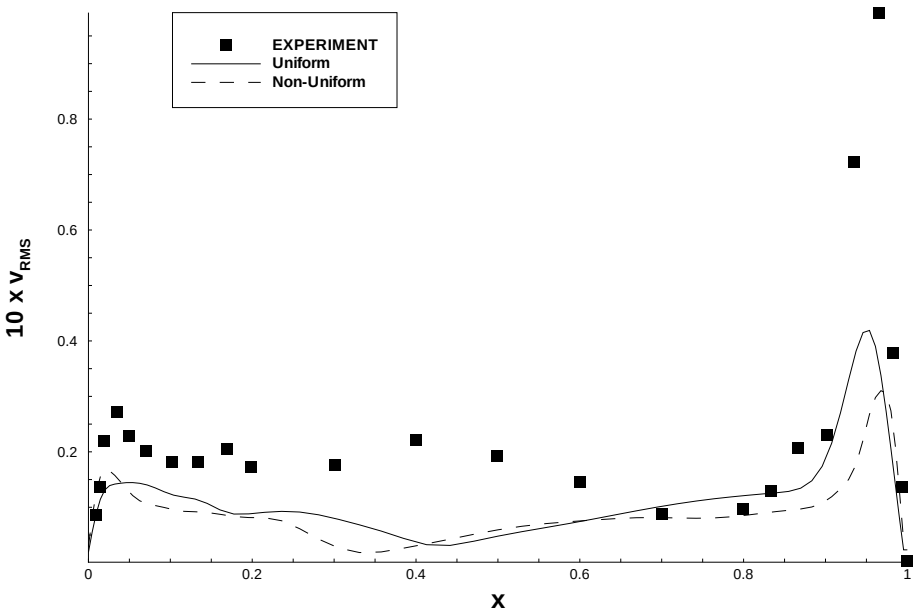

Figure 3.29: Comparison of v_{RMS} velocity component along Line A for uniform and regularised cases on 64^3 grid with third order reconstruction for Re=10000.

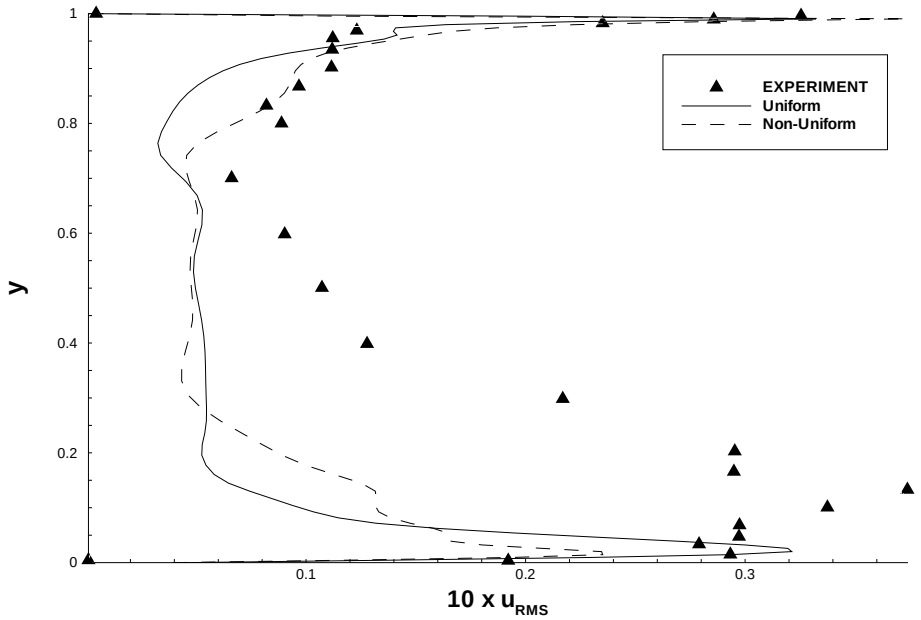

Figure 3.30: Comparison of u_{RMS} velocity component along Line B for uniform and regularised cases on 64^3 grid with third order reconstruction for Re=10000.

A statement made by Leriche & Gavrilakis (2000) with reference to turbulent RMS data on Line A was:

"the u' data from the experiment tends to be larger than those from the simulation, but the velocities involved are very small, perhaps of the order of a few mm/sec in the experiment where the measuring error would be proportionally greater. Thus this difference is probably of no significance.".

In terms of the actual magnitude of under predicted fluctuating components, the results of Leriche & Gavrilakis (2000) are closer to the experiment than the results obtained here. However, one should take into account that the mentioned study used a far higher grid resolution and gained only a marginal increase in magnitude for the turbulent quantities. The simulation applied 129^3 Chebyshev polynomials and a minimum and maximum grid spacing of 0.000301, 0.0245 respectively. Thus, this makes it difficult to make direct comparisons without computing the cases based on identical grids.

On the other hand the mean flow properties are captured adequately with the resolution employed here as is the distribution and tendency for the fluctuating components. This gives confidence in the mean flow properties which can be obtained on grids of similar density in the more complicated scenario, namely the complete Hypervapotron case.

The volume of computational domains considered for the Hypervapotrons later in this thesis comprise of $\simeq 18.5$ and $\simeq 66.7$ dimensionless units for a single cavity and three cavity array respectively. With the resolution equivalent to 64^3 grid employed here, we will require $\simeq 4.7$ and $\simeq 17.5$ million cells for these cases respectively.

These grid sizes are quite challenging within the computational resource available. Hence, the finest resolution presented for the lid driven cavity validation case gives the upper boundary of the resolution that could be obtained in the actual study.

3.3.3 Spectral Properties

The fluctuating streamwise component was used to obtain power spectra of velocity. The experimental data of Prasad & Koseff (1989) is just a straight line and the author assumes this represents the regression of data achieved in experiments. The power spectra describes how the signal (fluctuating velocity record) is distributed as a function of frequency. The spectra shown are one-sided since the validation data was presented in this form. The cut-off for the frequency in Hz corresponds to the cut-off in the experimental data of Prasad & Koseff (1989). It can be seen from the results (see Figure [3.31]) that both second and third order reconstruction exhibit the sub-inertial range and the -5/3 slope is a prominent feature of the figures. The power spectra for the first order case was considered spurious since the simulation demonstrated laminar flow and is not presented.

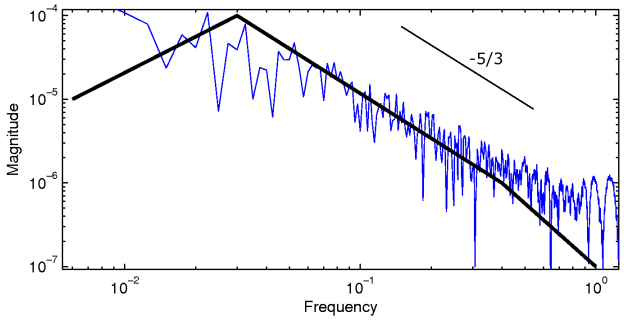

(a) Power spectra for second order reconstruction.

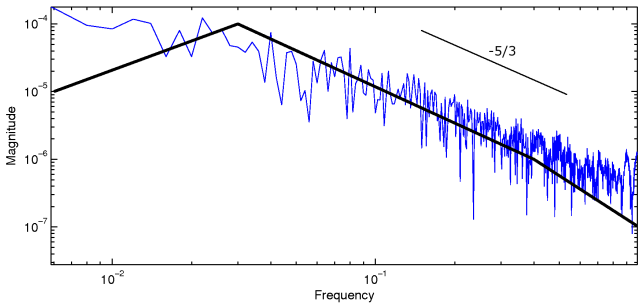

(b) Power spectra for third order reconstruction.

Figure 3.31: Longitudinal power spectra of u velocity based on averaging time period, for Re=10000. Units of magnitude is m^2/s^2Hz and the frequency units are Hz.

Chapter 4

Validation of a Lid Driven Cavity Flow with Heat Transfer

4.1 Validation of Conjugate Heat Transfer

The validation of conjugate heat transfer has been conducted and the solutions of both steady and transient models are presented. It has been shown that validation of the temperature field is achieved for steady and unsteady solutions when the fluid and solid exchange heat.

Such validation was required to ensure that the temperature treatment was accurate prior to the Hypervapotron analysis. Comparisons against analytical solutions by Özişik (1985) show that the current formulation and application of boundary conditions is satisfactory to model the conjugate problem (also required in the Hypervapotron models).

In addition to the fluid flow the solid alloy is also considered here and the conjugate heat transfer between different media with specified material properties is described. Several different models are presented and serve to provide confidence in

the implementation of the temperature scalar.

The code was developed from the multi-species formulation, see Shapiro & Drikakis (2005), which includes the capability to model any number of scalars within the code, therefore, it was expected from the outset that only limited validation of the temperature scalar was necessary.

Although the basis of the work presented for the conjugate heat transfer has considered one dimensional solutions it is thought that extension to the three dimensional model does differ in principle.

The one dimensional model in both the time dependent and steady state implementations demonstrate that application of the temperature scalar in the solid is physical, convergent and time accurate.

Finally simulation of a hybrid (laminar) lid driven cavity flow with heat transfer is provided. The flow over the two dimensional cavity is compared against the work of Chen (1996) and good agreement is achieved.

4.1.1 One Dimensional Three Layer Composite

Solutions have been obtained for a three layer composite consisting of two different media; water and the copper based alloy Cu-Cr-Zr (1.0% Cr,0.07% Zr). This arrangement was selected since analytical solutions for the case exist.

The case allowed application of the boundary conditions (constant temperature and flux) at the interface regions. Since at this stage only preliminary validation of the heat transfer was to be performed the fluid velocity was set to nearly zero in order to simulate stationary fluid and therefore a layered composite medium.

4.1.2 Problem Description

The two material, three layer composite with thermal conductivities k_f^* (fluid) and k_s^* (solid) is considered with $k_s^* > k_f^*$. In the general case with dimensions, we can have three layers of different thickness, however, for the validation we assume without loss of generality the same thickness for both materials. Also if we normalise temperature by the difference of constant temperatures at the upper and lower solid walls the non-dimensional temperature takes values within the range of 0 and 1.

The schematic of the non-dimensional problem is given in Figure [4.1]. As long as the flow is laminar, the non-dimensional heat conduction problem depends only on the ratio of thermal conductivities which has been selected to match the material for the Hypervapotron walls and water. The summary of the problem parameters is provided in Table 4.1.

Dimensionless Parameter	Magnitude
Reynolds Number	10
Ratio of Thermal Conductivity $k_{sf} = \left(\frac{k_s^*}{k_f^*}\right)$	691.0
Domain Length in x	6.0
Domain Length in y	3.0
Domain Length in z	1.0

Table 4.1: Thermal and geometric constants for the one dimensional model.

The validation provided by Özişik (1985) has been simulated on coarse grids, with dimensions, $n_x = 16$, $n_y = 30$ and $n_z = 12$. The non-dimensional parameters presented were used in both the steady state and transient models. Values for water and the copper alloy at 25^oC have been applied to derive the thermal constants. A fixed time step was applied to the simulations, 0.1.

The temperature profile for this case is easily obtained and solved and the reader is reminded that the piecewise temperature profile in all three domains is expressed by:

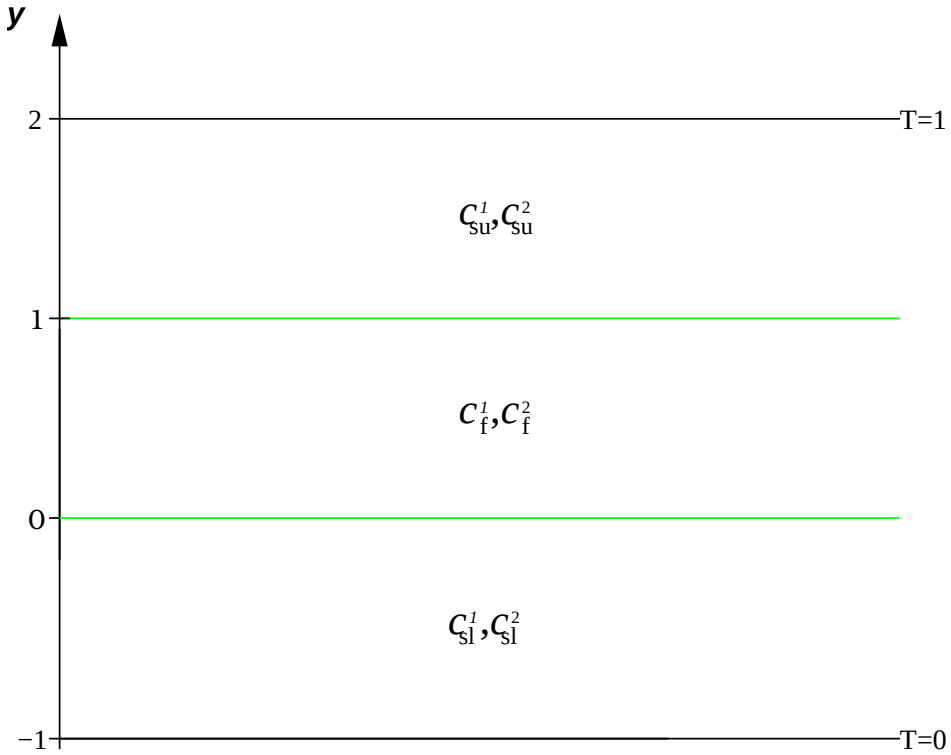

Figure 4.1: One dimensional three layer composite physical model.

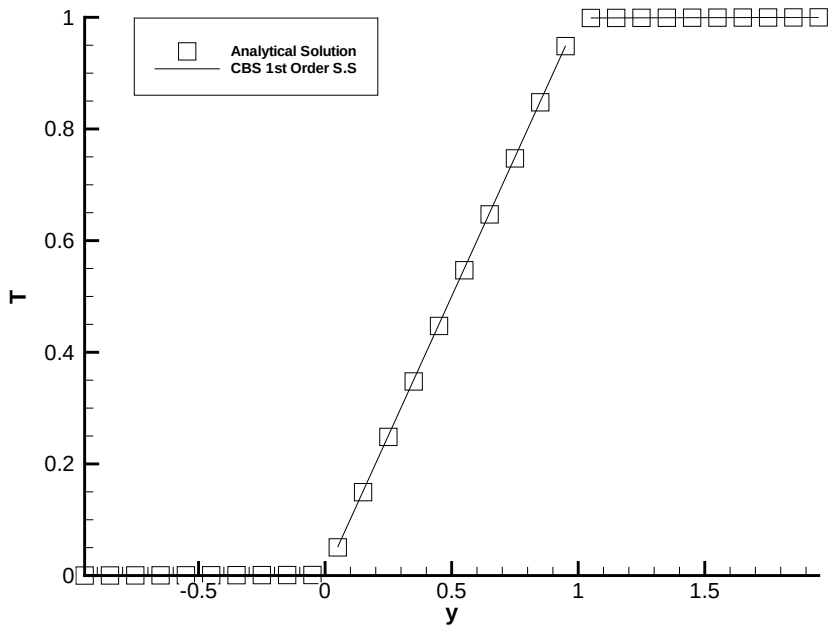

Figure 4.2: One dimensional three layer composite solution with CBS first order reconstruction and comparison with Özişik (1985).

$$T_{sl,f,su}(y) = c^1_{sl,f,su} y + c^2_{sl,f,su} \tag{4.1}$$

where the subscripts "sl", "f", and "su" refer to the lower solid domain, fluid domain and upper solid domain respectively. The constants for the resulting solution are obtained from the continuity of temperature and heat flux on the internal boundaries and constant temperature conditions on the lower and upper solid walls; $T_{sl}(-1) = 0$ and $T_{su}(2) = 1$ respectively, leading to:

$$T_{sl} = \frac{1}{2 + k_{sf}} y + \frac{1}{2 + k_{sf}} \tag{4.2}$$

$$T_f = \frac{k_{sf}}{2 + k_{sf}} y + \frac{1}{2 + k_{sf}} \tag{4.3}$$

$$T_{su} = \frac{1}{2 + k_{sf}} y + \frac{k_{sf}}{2 + k_{sf}} \tag{4.4}$$

Using these formulas for each block in the domain we compare the analytical solution to the computed result, see Figure [4.2].

The solution was computed using a first order reconstruction until convergence was reached. The convergence criteria was satisfied once the solution computed residuals reached a given maximum value. In this case the value was 1×10^{-3} for all variables.

From the analytical solution it is possible to notice that the gradient of temperature in the solid differs from that in the fluid by the factor of $1/k_{sf}$ which is of order $1.5 \cdot 10^{-3}$. Although the Figure [4.2] looks as if the solution provides a constant temperature within the solid regions in fact this behaviour is due to the high ratio of thermal conductivities of the solid and fluid media.

The temperature drop in the solid upper and lower regions is shown in Figures [4.3] and [4.4] and is a monotone, linear function. The simulations conducted demonstrate good comparison against the analytical solutions.

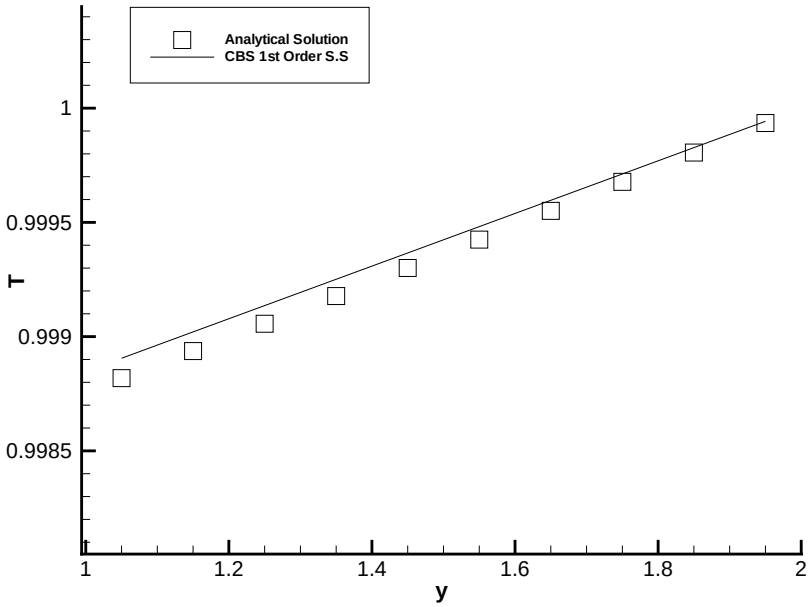

Figure 4.3: Linear temperature increase over solid upper wall (from steady state solution with first order reconstruction and comparison with Özişik (1985)).

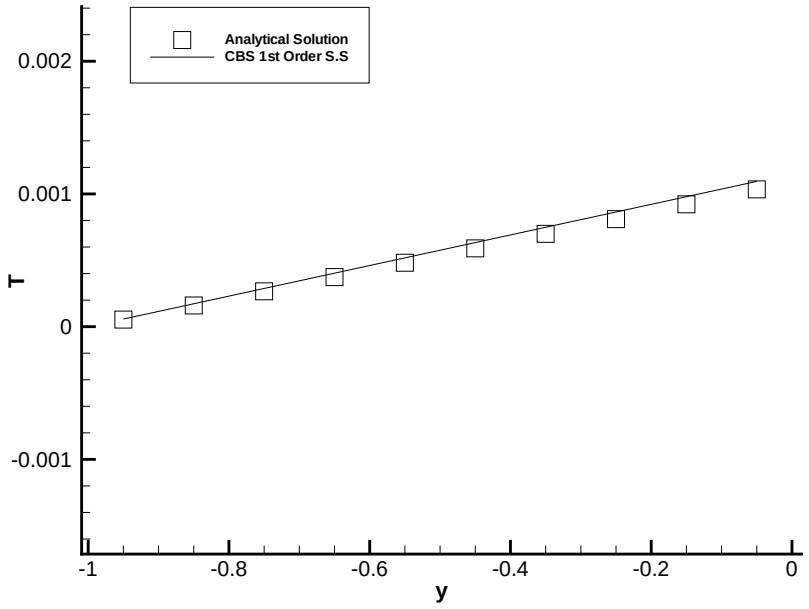

Figure 4.4: Linear temperature increase over solid lower wall (from steady state solution with first order reconstruction and comparison with Özişik (1985)).

4.1.3 Transient One Dimensional Model Single Medium

In order to verify the time dependent solutions we consider heat front propagation in a uniform slab of material with the same dimensions as in the previous case. The computational setup, including the domain size and the grid are as in the previous case however, in this instance the ratio of heat conductivities is equal to one, i.e. $k_{sf} = 1$. The initial condition for the problem is $T_{su}(2) = 1$ in the complete domain. Then at time $t = 0$ the lower wall outer surface is dropped to a constant temperature $T_{sl}(-1) = 0$ while the upper wall outer surface is maintained adiabatic (insulated b.c). The analytical solution of the resulting transient, one dimensional problem is given by Özişik (1985).

For this problem we introduce an additional non-dimensional quantity, the Fourier number:

$$F = \frac{\alpha_s^* t_c^*}{l_c^{*2}} \tag{4.5}$$

The Fourier number is a measure of the rate of heat conduction in comparison with the rate of heat storage in a given volume element. Therefore the larger the Fourier number, the deeper the penetration of heat into a solid over a given time. Now we may express the non-dimensional solution (of a single medium) through the following series expansion, one may also note that the time considered in the following equation is also the total run time of the simulation:

$$T(y,t) = \frac{4}{\pi} \sum \frac{(-1)^{n+1}}{2n-1} exp(-\lambda_n^2 F) cos(\lambda_n y) \tag{4.6}$$

Here the quantity λ_n is defined by $\lambda_n = \pi(2n-1)/2$. By using this formula for the temperature profile we are able to compare the result to the computed solution.

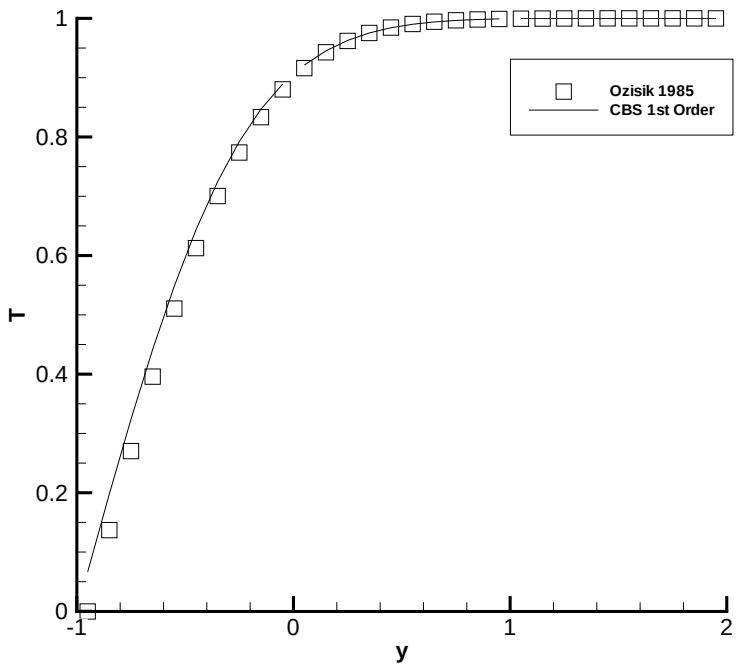

Figure 4.5: Comparison for the transient conjugate heat transfer with analytical solution provided by Özişik (1985) at t=50.

The solution, see Figure [4.5], was computed using a first order reconstruction for a number of pseudo time steps until convergence was reached. The convergence criteria was satisfied once the solution computed residuals reached a given maximum value. This value was 1×10^{-3} for all variables.

The numerical solution compares well with the work of Özişik (1985) and served to provide confidence in the transient results with heat transfer of the time dependent solver.

The transient solution can be computed as a three layer composite by expanding the series solution of the single media through introducing the array of size three for the thermal conductivities. However, such a solution approaches the steady state behaviour as shown in Figure [4.2].

4.2 Laminar Lid Driven Cavity Flow with Heat Transfer

4.2.1 Introduction

The numerical results based on the evaluation of a steady hybrid lid driven flow over a two dimensional cavity is compared against the work of Chen (1996). The model consists of a laminar two dimensional cavity with the upper lid wall some distance above the cavity mouth.

The case is simple to implement and served to show that the numerical method approximates the temperature diffusion in the channel and cavity well. The reader may note the case has the advantage to study the interaction between the cavity and the channel (i.e. the shear layer) which also appears in the Hypervapotron cases.

The boundary and initial conditions for the laminar flow model were straightforward to apply and therefore the physical behaviour of a two dimensional flow was quickly verified by using this case study. The model was simulated with Re = 1,000, Pr = 2.2 and steady state solution was achieved.

4.2.2 Problem Description

The lid driven flow over an open cavity can be characterised as a nearly parallel flow in the channel. This channel flow then causes the formation of eddies in the cavity. It can be observed that most of the space within the cavity is occupied by a primary vortex.

The secondary eddies that result from the motion of the primary recirculation along the cavity walls appear at the lower corners of the cavity. Consequently, the motion

of the primary eddy is the dominant factor in affecting the heat transfer over the cavity walls.

The physical system is subject to the following initial and boundary conditions. When the value of $H_{chan} = 0$, the physical system is a lid driven cavity flow see Figure [4.6]. The characteristic length is the cavity width and the simulation used a channel height to cavity width ratio of 0.2 leading to non-dimensional channel height $H_{chan} = 0.2$. Here, the Reynolds number is based on the moving wall velocity with Re=1000.

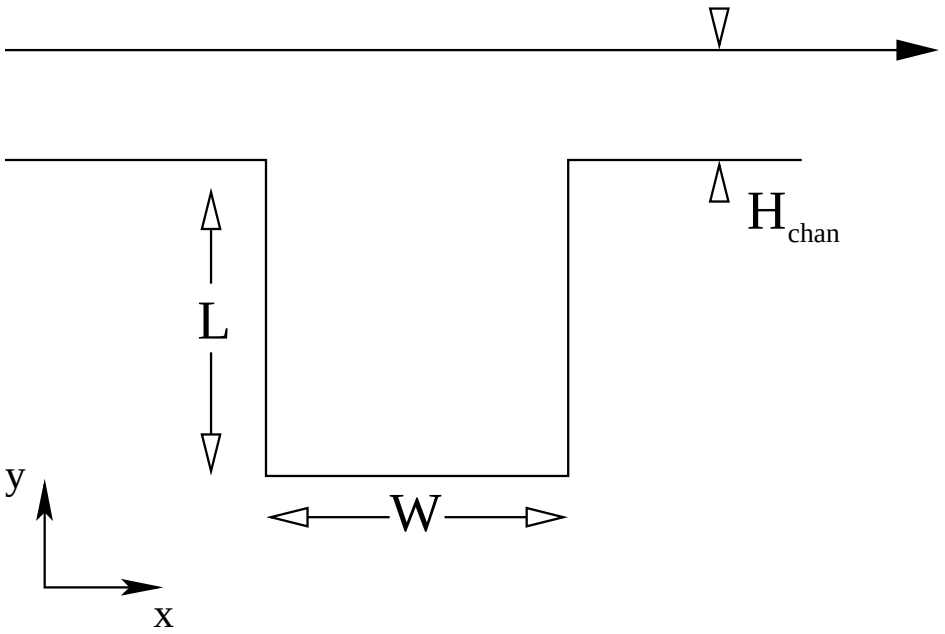

Figure 4.6: Physical domain for the hybrid lid driven case.

The results were obtained from a 111×131 uniform grid in the cavity section and compared against a 110×130 grid in Chen (1996). The characteristic length in the model was the cavity width and the characteristic velocity was the lid velocity. The upstream and downstream lengths were chosen to be four times the cavity width with the domain origin located at the upper upstream cavity corner.

4.2.3 Initial and Boundary Conditions

The velocity distribution at the inlet is obtained by solving the impulsively started plane Couette flow problem and the outlet of the domain has the extrapolation of all flow field variables. The initial condition for the steady state simulation is that the flow and upper channel wall are both at rest at time, $t_0 = 0$ and the non-dimensional temperature in the channel is set to 0. The boundary conditions are enforced as follows:

- At the inlet:

$$u(y) = \frac{y}{H_{chan}} \tag{4.7}$$

$$\frac{\partial v}{\partial x} = 0, T = 0 \tag{4.8}$$

- At the outlet all variables were:

$$\frac{\partial}{\partial x} = 0 \tag{4.9}$$

- At the upstream and downstream lower walls of the channel:

$$u = v = 0, T = 0 \tag{4.10}$$

- At the cavity walls constant temperature is applied:

$$u = v = 0, T = 1 \tag{4.11}$$

- Finally on the upper channel wall surface we have:

$$u = 1, v = T = 0 \tag{4.12}$$

4.2.4 Results and Discussion

The steady state solution was achieved with a Full Multigrid - Full Approximation Storage Algorithm (FMG-FAS). Here, three stage V cycles are used to accelerate convergence. The convergence criteria was 1×10^{-7} for all variables. The results of the simulations are presented in terms of non-dimensional temperature, velocity plots, see Figures [4.7] and [4.8] and wall heat fluxes, see Figures [4.9] and [4.10].

The flow field exhibits several features expected to be seen in the Hypervapotron main section due to the presence of the cavity and the channel interaction. Most importantly the flow field contains the shear layer which is a key characteristic of the flow structure. The shear layer resides over the cavity mouth and is highly dissipative although still laminar. Confidence that the shear layer flow can be resolved is extremely important since the flow structure inside the cavity is heavily influenced by the shear layer and may not be representative of the true cavity flow structure if under resolved. The presence of the corner vortices at the base of the cavity are fully resolved, see Figure [4.7].

In the comparison case see Chen (1996), results were obtained using a less robust numerical scheme known as the 'deterministic vortex method'. In this method, at each computational time step, both equations (linear diffusion and nonlinear Euler) are solved sequentially to give the approximation of the vorticity field. The solutions achieved by using the current formulation gave much better results. This can clearly be seen by the presence of the corner vortices that are resolved and do not appear in the results of the comparison data, see Figure [4.7].

Over the cavity walls the heat transfer rate is enhanced by the motion of the primary eddy. Contour plots of the iso-concentration lines are shown in Figure [4.8], the asymmetric characteristic of dense contour lines near the downstream upper corner reveal the high heat transfer rate in this region.

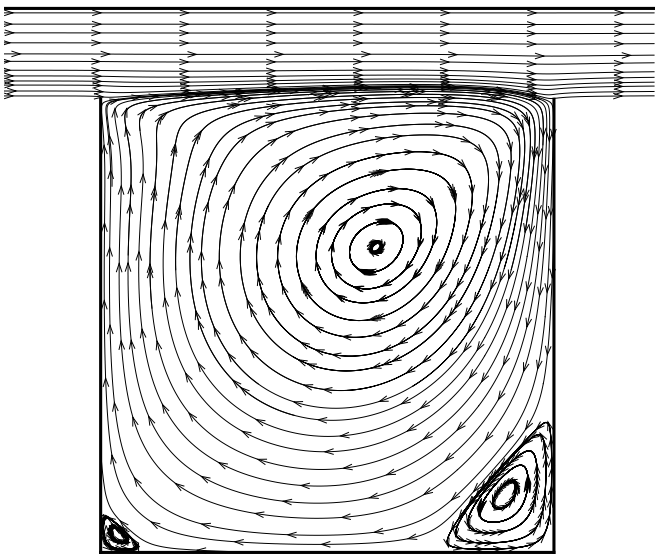

Figure 4.7: Streamlines of velocity for the hybrid lid driven case with Re=1000 on 111×131 uniform grid.

Figures [4.9] and [4.10] illustrate the local wall heat flux distributions over the cavity walls (calculated using a first order central differencing scheme). The largest heat flux occurs near the downstream upper corner due to the impingement of the separated layer from the bulk channel flow inertia. Small differences do exist between the CBS solution and that presented by Chen (1996). The left wall demonstrates the least favourable comparison of the two. It may appear from Figures [4.9] and [4.10] that the heat flux approaches zero at the lower corner on either wall. However, this is not the case. The heat flux in the corner regions is significantly lower than the rest of the wall since the secondary recirculation provides much lower magnitude wall velocity and therefore lower heat flux. In order to illustrate this effect, a zoomed in view of the heat flux on the left cavity wall is provided in Figure [4.11].

It is expected that the difference present is superficial since the digitisation of the comparison case introduces a large error close to the wall region.

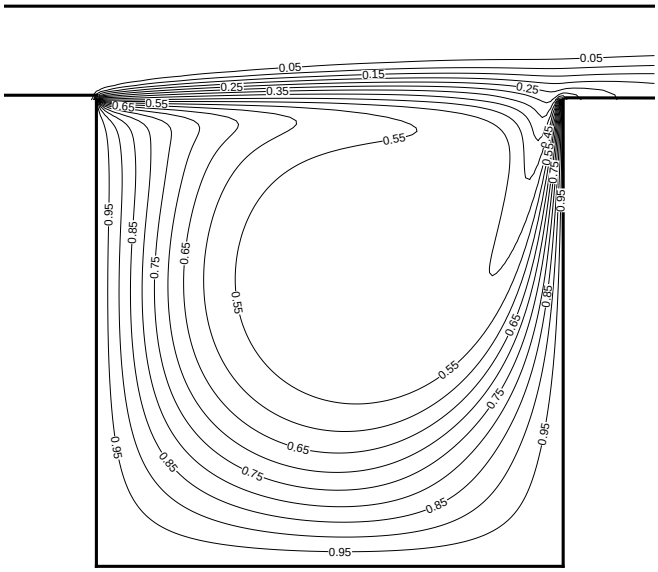

Figure 4.8: Temperature contours for the hybrid lid driven case with Re=1000 on 111×131 uniform grid.

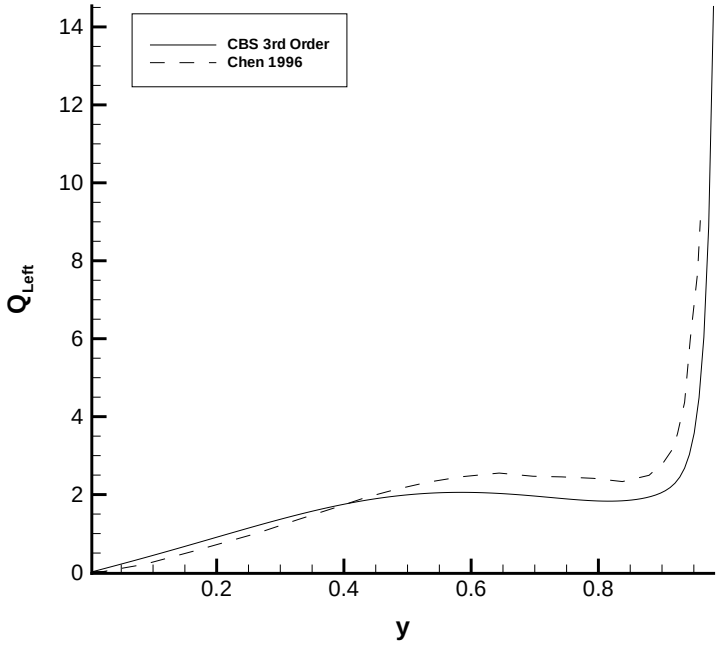

Figure 4.9: Left side local wall heat flux using third order central differencing in comparison with Chen (1996).

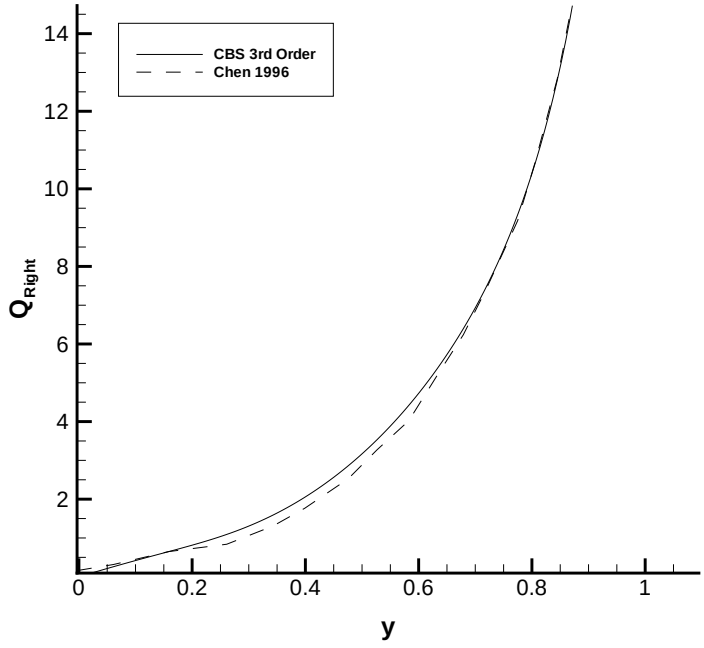

Figure 4.10: Right side local wall heat flux using second order central differencing in comparison with Chen (1996).

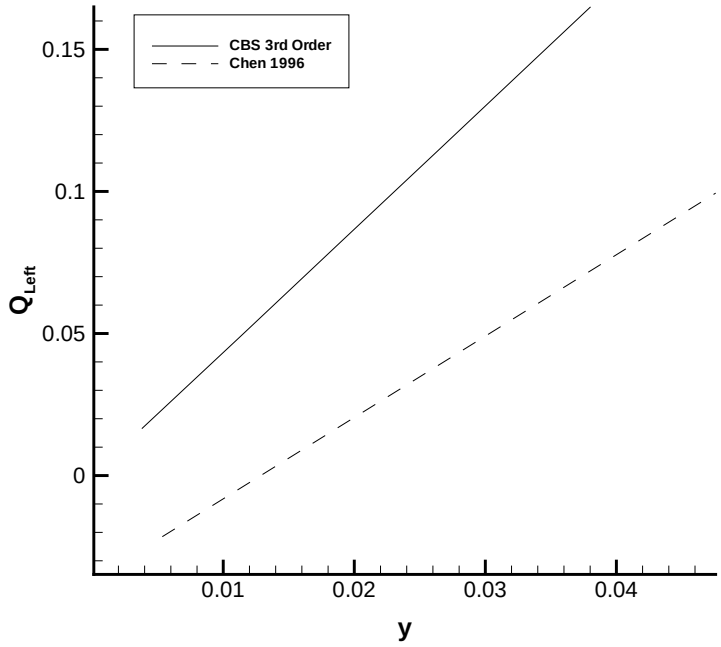

Figure 4.11: Left side corner local wall heat flux using first order central differencing in comparison with Chen (1996).

Chapter 5

ILES of Hypervapotron Flow Configurations with Heat Transfer

5.1 Introduction

The motivation to obtain optimised heat fluxes within Hypervapotrons has defined the need for understanding and analysis of the unsteady thermo-fluid behaviour that exists within the ribbed section of the ion beam dumps. The use of a cavity array within the main duct sections of a Hypervapotron provides a large increase in exposed surface area.

The Hypervapotron takes advantage of an efficient technique of removing heat fluxes, namely, subcooled flow boiling. The idea of subcooled flow boiling for heat sinks has been considered and it has been proven, for high heat flux consumption the CHF is an unsuitable operating point. Such high heat flux may result in dry out at the wall surface and be responsible for thermal shock during pulsing. However, studies based on the heat transfer and flow characteristics within Hypervapotrons suggest that enhanced heat dissipation may be achieved by inducing controlled wall

boiling. It has been suggested by Boyd (1985), the Hypervapotron technique, which involves fins placed transverse to the fluid flow in the device, "is one of the most intriguing fin enhancement techniques predicated on the idea of allowing a portion (the base) of the fin to operate at a temperature greater than the CHF temperature, while the remaining portion operates near the onset of stable nucleate boiling". The Hypervapotron technique in subcooled flow boiling and the corresponding CHF has been approached by many authors, a milestone study of this is Cattadori *et al.* (1993a). Within the latter, useful visualisation data related to the CHF was recorded and important characterisation of the Hypervapotron effect as a function of geometry and fluid flow conditions was obtained through high speed videography.

Many experimental investigations have evaluated the performance of Hypervapotrons for short pulsing in NBH systems (used at JET), which is typically around 5-10 seconds; a recent work of this type is Nightingale *et al.* (2001). Several studies conducted on Hypervapotron performance applied in nuclear reactors have been reviewed by Chang & Baek (2003). Here attention is drawn to factors affecting the CHT and several theoretical models are discussed. Performance analysis has demonstrated that the cavity and channel design has significant impact on the overall performance characteristic of the device, see Milnes *et al.* (2005). Here it was suggested that the Hypervapotrons used at JET are the most economical and reliable energy dumps available for NBH systems. The latter investigation was focused on the performance of Hypervapotrons under long pulse operation.

Further information surrounding the longer pulse (approx. 1000 seconds) performance may be found in Dahlgren *et al.* (1994). The development of novel designs for Hypervapotrons has been conducted by others and in particular some useful enhancements made by a saw-toothed design have been noted in Ezato *et al.* (2001). Further, the more established swirl tube concept and comparisons of this with the cavity array design previously used have received some attention by Baxi (2004).

Although much experimental work has been conducted on these devices numerical simulations have received far less attention until recently. In particular, studies such as Pascal-Ribot *et al.* (2005) Pascal-Ribot *et al.* (2007) using Neptune and most recently the two dimensional studies conducted by the UKAEA using RANS models, see Milnes & Drikakis (2009), have provided an assessment of various methods available using the commercial solver CFX. Through numerical methods, in particular, those present here, the analysis of flow manipulation for heat transfer enhancement may be conducted to indicate the locations and development thermal boundary layer and hot spots occurring during pulse activation. Simulations and numerical analysis are fast becoming an integral part of the design process where this cooling device is concerned.

Within this thesis is presented the results of studies conducted using AC-ILES for the Standard design with various grids and high order variable reconstructions. This serves to provide a fundamental understanding of the flow structure and its effect on the heat transfer within the Hypervapotrons under operational conditions. On beam activation the Hypervapotrons are bombarded by high energy residual ions from the NBH process, the water cooled tiles absorb this heat energy and the solid face of the device exterior is maintained at approximately 450^oC. The beam stopping elements are manufactured from a copper based alloy Cu-Cr-Zr (1.0% Cr,0.07% Zr). This physical circumstance corresponds to a far field, solid surface, boundary condition that is specified as constant temperature. At the interior wall surface, the working fluid; water, passes over the ribbed duct and is exposed to high temperatures at the wall surfaces. It is assumed that the flow through the duct is developed and therefore a periodic model was examined to aid understanding of the flow field features.

Three transport modes of heat transfer occur in our system; they are heat conduction, (non-linear) highly unpredictable nucleate boiling wall heat transfer and forced convection. It is expected that convective heat transfer is the primary mechanism

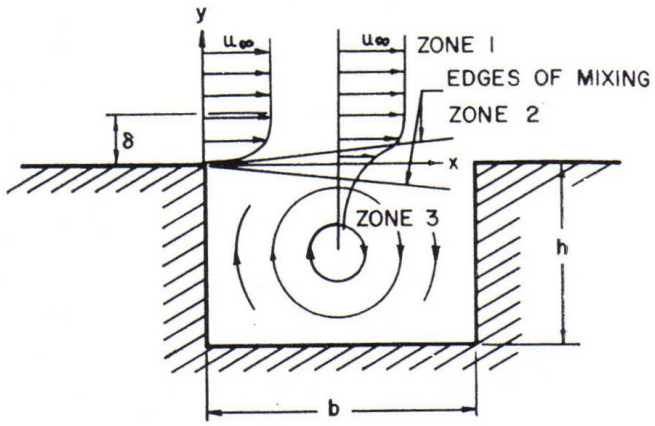

Figure 5.1: Separated flow over a cavity.

through which cooling is achieved in the device. The mainstream flow is responsible for the large exchange of heat transfer from the near wall region to the free-stream temperature. At the near wall region methods to approximate the temperature variable and heat flux distribution at the solid-fluid interface is of primary concern. An important aspect of an open cavity flow is the separation of the fluid over the discontinuous path.

The boundary layer separation in an open cavity flow is characterised by the formation of reversed flows and recirculation regions. Initially the oncoming boundary layer enters the cavity and forms a shear layer. The layer resides over the cavity and borders on the external flow, the shear layer itself widens from the upper left corner to the upper right corner (assuming the direction of the flow is from left to right). At this stage, part of the shear layer (zone 2) at the right side cavity wall detaches and is deflected into the cavity notch itself, giving rise to the flow in the cavity (zone 3) (as in Figure [5.1]). Here, a large unsteady vortex resides from the separated shear layer over the open cavities and secondary flow is generated from this primary motion.

This concept results in a highly non-linear flow regime of unstratified wall boiling which occurs at repeated locations within the cavities while the cavity base exceeds

the CHF. A large primary vortex is formed and thermobuoyancy helps promote secondary vortex shedding (at the cavity mouth) which contributes to the replenishment of subcooled water ensuring dry out is avoided. The voidage that occurs in the cavities (between the fins) is born into a region of high mixing and subcooled water and is believed to condense quickly. The turbulent motion of the fluid flow is responsible for the rapid exchange of heat transfer at the wall surface and this results in an unsteady temperature behaviour at the interface. The wall heat flux exhibits different modes of behaviour based on the direction of recirculation, number of vortices and the location in which they reside. The flow path of the unstable eddies that leave the cavity and travel downstream require an explicit unsteady time dependent solution of the flow field to effectively recover the flow behaviour. The ability to achieve the correct wall heat flux relies on the solver to determine properties within both media (solid and fluid) and resolve the unsteady interface temperature (which is heavily related to the flow structure surrounding the solid material). However, since a turbulent high speed flow is passing over the high temperature surface it is assumed that boiling will occur only in a thin layer. Therefore in this region, like in the solid alloy, heat transfer occurs by conduction. Near wall, where velocity is zero, conduction is the sole means of transport and when the velocity takes some finite value an associated heat transfer via convection transport occurs.

During nominal operation it is assumed the Hypervapotrons have a steady flow rate and the operational parameters of the devices within the JET facility are outlined in Table 5.1.

Operational Parameters	Units	Magnitude
Flow Velocity Range	$\frac{m}{s}$	4 - 6
Inlet Pressure Range	$10^5 \times \frac{N}{m^2}$	4 - 6
Pressure Drop	$10^5 \times \frac{N}{m^2}$	< 1
Peak Surface Temperature	K	723.15
Temperature Gain (per unit)	K	30

Table 5.1: Nominal operation parameters for Hypervapotrons.

5.2 Timescale Analysis

Although the forced convection within the channel section is the dominant mode of heat transfer, the scalar transport is due to both advection and diffusion as expressed in the governing equations (see Chapter 2). Analysis of the non-dimensional equations can lead to the derivation of several important timescales related to the transport of the temperature field and flow development. Let us consider the characteristic timescales for the development of flow and heat transfer processes. In the following analysis media properties have been taken from Rohsenow *et al.* (1998), the key parameters are summerised in Table 5.2.

Parameter	Magnitude
Prandtl Number	7.13
Ratio of Thermal Conductivity $k_{sf} = \left(\frac{k_s^*}{k_f^*}\right)$	691.0
Ratio of Thermal Diffusivity $k_{sf} = \left(\frac{\alpha_s^*}{\alpha_f^*}\right)$	866.0

Table 5.2: Non-dimensional thermal constants for Hypervapotron simulations

For an incompressible flow, the development of the flow is linked to the development of the pressure field. The characteristic time τ_f^* for the flow development can then be expressed as the time it takes the pressure wave to propagate through the geometry:

$$\tau_f^* = \frac{L^*}{a^*} \tag{5.1}$$

where L^* is the characteristic length of the geometry, which generally cannot be the same as the characteristic length l_c^* used when making the system non-dimensional, and a^* is the speed of sound. Estimates for the length of the Hypervapotron array and the speed of sound in water at $293.15K$ yields the flow development time of approximately $\tau_f^* \simeq 10^{-4}s$. For the scalar transport due to advection the characteristic length is given by the (reference length) width of the cavity used in the

non-dimensional equations. The characteristic time for the scalar transport due to advection τ_a^* which represents convective heat transfer can then be estimated as:

$$\tau_a = \frac{l_c^*}{u_c^*} \tag{5.2}$$

The above yields $\tau_a \simeq 5 \cdot 10^{-4} s$ for the maximum flow speed and cavity width taken as characteristic parameters. Finally, the heat conduction timescale is given by:

$$\tau_c^* = \frac{L^{*2}}{\alpha_{f,s}^*} \tag{5.3}$$

where characteristic length L^* and thermal diffusivity α^* is chosen depending on whether we consider the fluid or solid regions. In the solid, the characteristic length is given by the thickness of the solid wall below the cavities ($6mm$). Taking into account that the thermal diffusivity of the alloy used can be estimated at $1.25 \cdot 10^{-4} \frac{m^2}{s}$, this yields $\tau_{c,s}^* \simeq 0.288s$.

In water, at room temperature ($293.15K$), the thermal diffusivity is given by $1.44 \cdot 10^{-7} \frac{m^2}{s}$ and the heat conduction on the scale of the cavity width leads to characteristic time scale $\tau_{c,f}^* \simeq 62.6s$.

The flow establishment timescale indicates the time period required for stabilisation of the pressure field in the problem. This occurs very quickly for our problem. Further, since the complete Hypervapotron geometry includes more than 250 cavities, we can expect the flow to develop a periodic pattern away from the inlet and outlet sections. The temperature front then propagates through the solid, reaching the fluid domain where the flow has been already established.

This process is much slower than convection and it would be difficult to resolve it in a fully coupled manner due to substantial computational time required for the front to propagate through the solid. Once the temperature front has reached the fluid, the dominant heat transfer mechanism within the fluid is convection.

5.3 Problem Formulation

The entire Hypervapotron is an immense task to model as a three dimensional geometry and would require an excessive number of grid nodes and consideration of inter alia entrance and exit geometry.

The main section of the Hypervapotron is essentially an array of cavities heated from beneath in a channel flow arrangement; this more simple and recurrent geometric detail is the subject of the investigations.

Based on these observations, the following computational strategy can be adopted to resolve the transient convection-dominated heat transfer in fluid:

- Depending on whether the resolution of the thermal boundary layer in solid is required, the problem can be computed with conjugate heat transfer or in fluid domain only with the fixed temperature boundary conditions.
- The flow can be initially computed for a periodic section of the Hypervapotron encompassing a number of cavities. This would require the forcing mechanism derived in Chapter 2.
- The temperature field is then initialised with constant temperature in the fluid region for the fluid only problem and constant temperature in the solid region for the conjugate heat transfer problem.
- The computation proceeds through the initial stages of the temperature field development in allowing to establish the link between the flow structure and heat flux at the fluid-solid interface.

This approach would allow the analysis of the flow and convective heat transfer in both fluid only and conjugate models and circumvent the computational difficulties associated with the complete time dependent conjugate problem.

The extent of the streamwise length selected for the periodic domain is not a trivial question. Geometrically, the "repeating unit" can be represented by a single cavity with 0.5 (non-dimensional) lengths for the upstream and downstream plates, see Figure [5.2].

On the other hand, for separated turbulent flows with repeated geometrical units it can occur that one repeating unit is insufficient from the point of view of turbulent statistics. This has been observed, for example in DNS simulations of wall mounted cubical arrays, see O. Coceal & Belcher (2006). In order to test whether this one repeating unit is sufficient, another configuration has been selected with three repeating units, see Figure [5.3].

The impact of side wall effects has been neglected within the simulations conducted here due to the large increase in grid nodes required to resolve the additional spanwise walls in the domain. The model is assumed to be span periodic since the spanwise length associated with the Standard geometry is exactly 16 times the characteristic length. In such circumstances it can be suggested periodicity in this direction is an acceptable modelling compromise.

A distance of two cavity widths (equivalent to 2 non-dimensional units) was provided in the spanwise direction with uniform cell distributions. However, clustering was employed in the remaining directions in order to resolve near wall regions sufficiently.

The overall grid densities are representative of that used in the cubical cavity simulations and it was thought that with high order methods the flow would be efficiently resolved to within an order of accuracy.

Based on such data the topology of the flow structure resulting from different reconstruction schemes and grids may be discussed. This would support qualitative analysis of flow topology (and resulting differences in heat transfer) for the various cases considered within this study.

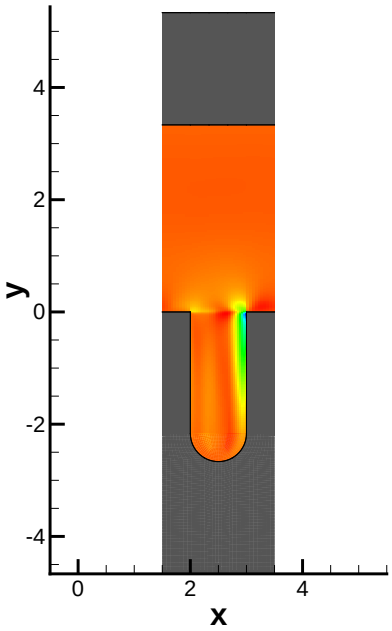

Figure 5.2: Repeating unit based on one cavity.

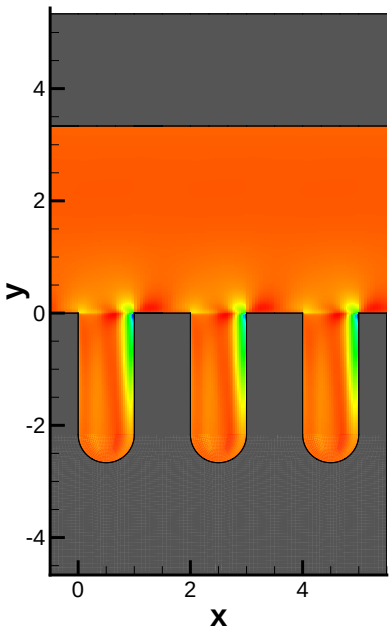

Figure 5.3: Repeating unit based on three cavities.

5.4 Parallelisation and Multiblock Grids

Due to the wall curvature on the base of the cavities, a single block was not easily mappable in computational space and therefore a structured multiblock approach was used. All cases were solved using structured multiblock grids and the parallel implementation of the numerical algorithm reduced the computational time durations significantly.

The multiblock domains consist of 12 and 72 blocks in the $x - y$ plane for the single and three cavities models respectively, see Figures [5.4]-[5.7]. Initially two dimensional simulations where conducted before code parallelisation after which grids were extruded in the spanwise direction to provide a three dimensional domain. Grids were then further decomposed in the z-axis by a specified number of slices, totalling in a different number of blocks for each of the cases.

The three dimensional domains used either 96 or 192 blocks in the single cavity coarse and medium cases respectively. The three cavity coarse grid cases used a total of 576 blocks. Two different grid resolutions were used in simulations for the single cavity. Both coarse and medium grids were all that could be computed within the PhD time frame due to the three dimensional requirement.

Fine grids would require significantly more time than available and therefore the flow may still be under resolved. Coarse grids for the single and three cavity cases were 783,328 and 3,717,168 nodes respectively. Medium grids for the single and three cavity array cases computed used 5,691,840 and 9,561,600 nodes respectively. However, the medium grid, three cavity cases required further run time to acquire convergence and therefore are not presented.

The cases all required significant High Performance Computing (HPC) time and the storage requirements had also become excessive to the point where data was very tedious to manipulate and postprocess. The cases were computed on the Cranfield

University HPC facility, ASTRAL. The parallelisation was based on MPI (Message Passing Interface) standards and data communication was based on distributed memory storage. Within the message-passing methods, the computational grid, is subdivided into non-overlapping sub domains with each contribution being assigned to a separate processor. The optimum number of processors for any one case was determined by time tests.

The boundary conditions were stored into an end of loop layer of ghost cells, with each edge having two ghost cells overlapping in space with the adjacent block coordinates. The boundary conditions were specified on each block face. The performance of the parallel implementation is easily highlighted when subroutines are subject to time testing to investigate the scalability of the solver on specific grids. The time duration of subroutine operations in the solver has been recorded after a single time step on the grids. This serves to illustrate the parallel scalability of the algorithm with the current multiblock decomposition, see Figures [5.8]-[5.13].

From the data in the Figures [5.8]-[5.13] and Table 5.3, the reader may note that an increase in the number of processors results in the ratio of the sweep routine and message passing computing times changes until the message passing bottlenecks the scalability. This time testing showed that the optimum number of processors for each case were 8 on the coarse grid and 16 for the medium grid for the single cavity case. Finally 24 slices were applied for the solid-fluid three cavity array coarse grids.

IPS	N	BCS	SWP	Inv-X	Inv-Y	Inv-Z	Vis-X	Vis-Y	Vis-Z
1	5691840	13.64	137.7	16.40	20.30	16.87	8.62	12.70	49.17
2	5691840	5.76	48.67	7.80	8.15	7.38	3.77	4.67	11.14
4	5691840	5.45	28.77	3.93	4.18	4.09	1.92	2.58	6.62
8	5691840	3.88	13.71	1.97	2.02	2.16	0.94	1.12	1.62
16	5691840	2.78	7.93	0.99	0.97	1.32	0.46	0.55	0.86
32	5691840	2.49	5.47	0.5	0.49	0.89	0.23	0.27	0.60

Table 5.3: Decomposed time durations of solver subroutines on medium grid (5,691,840 nodes) for single cavity simulations.

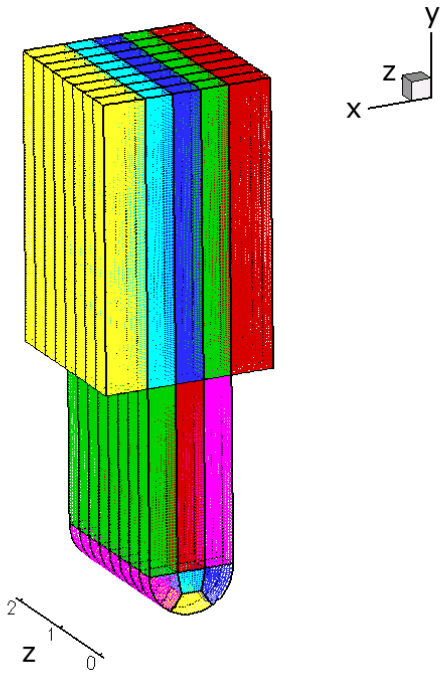

Figure 5.4: Isometric view of coarse grid for single cavity model with eight slices in the z direction axis (Standard design).

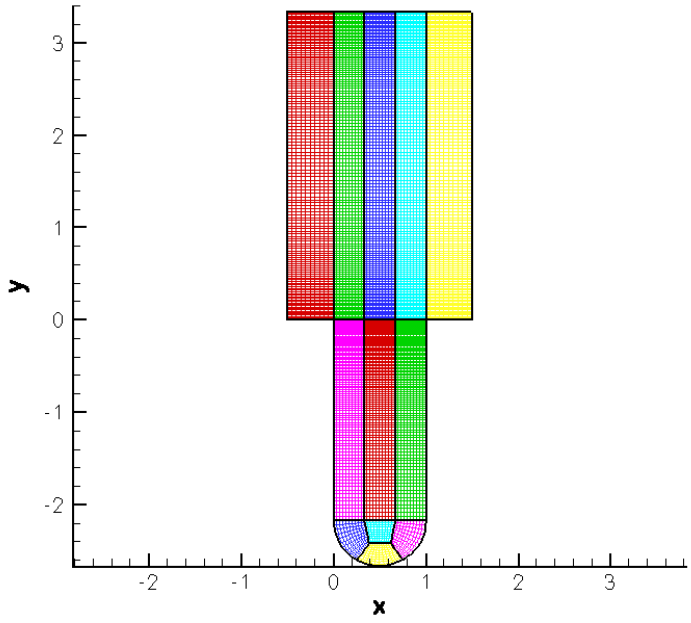

Figure 5.5: Planar $x-y$ view of coarse grid for single cavity model Standard design (12 blocks).

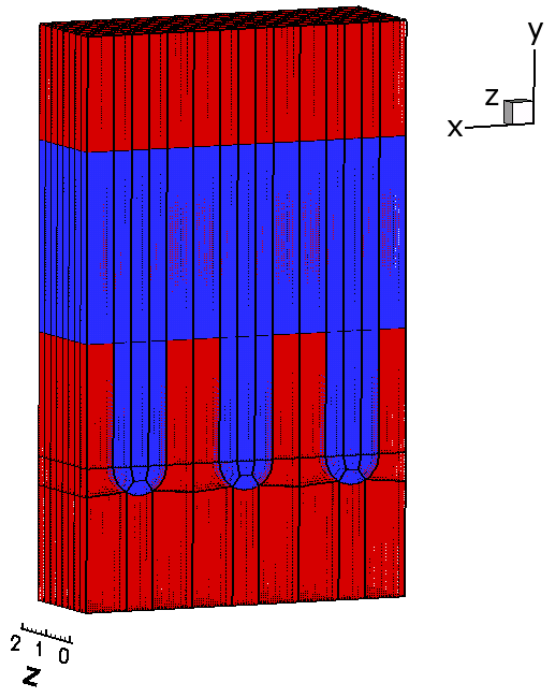

Figure 5.6: Isometric view of coarse grid for three cavity model with eight slices in the z direction axis (Standard design).

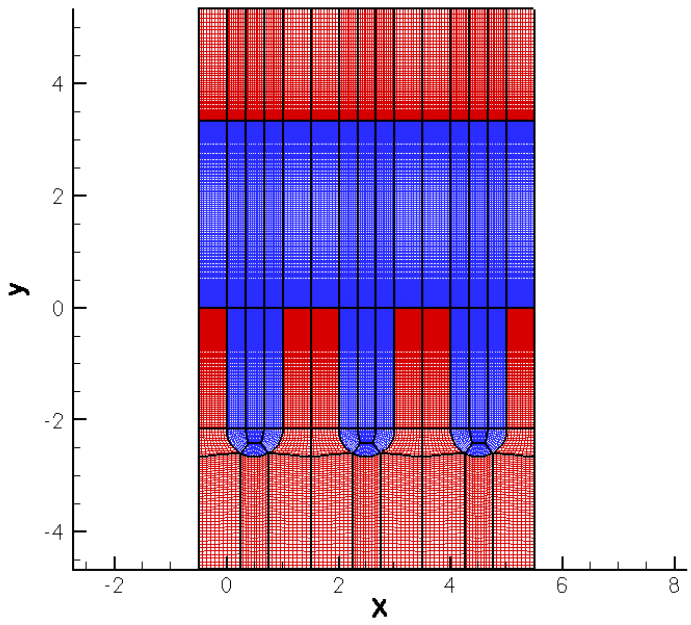

Figure 5.7: Planar $x - y$ view of coarse grid for three cavity array Standard design (72 blocks).

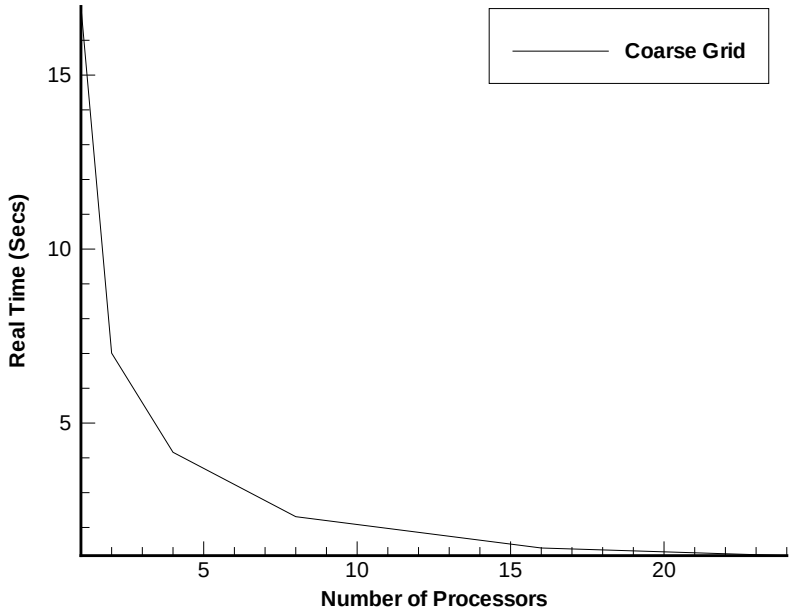

Figure 5.8: Parallel scalability on sweep routine with coarse grid for the Hypervapotron Standard design.

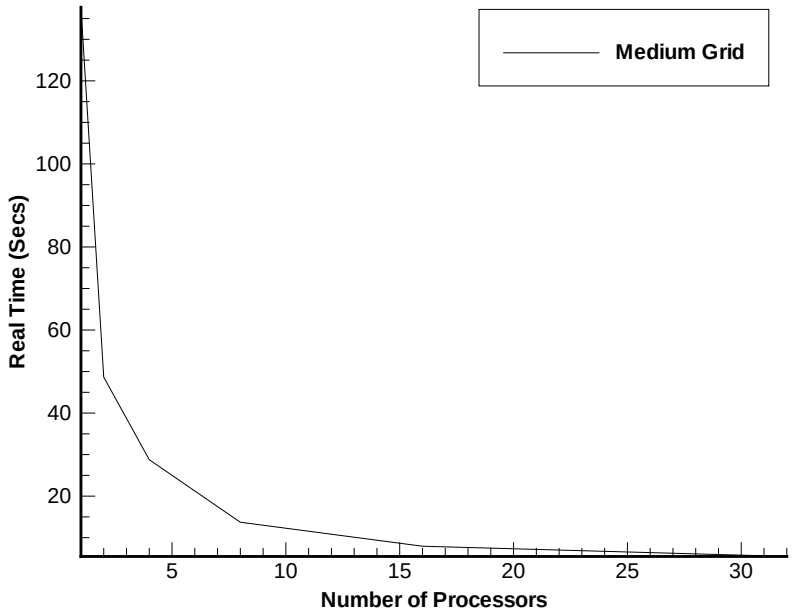

Figure 5.9: Parallel scalability on sweep routine with medium grid for the Hypervapotron Standard design.

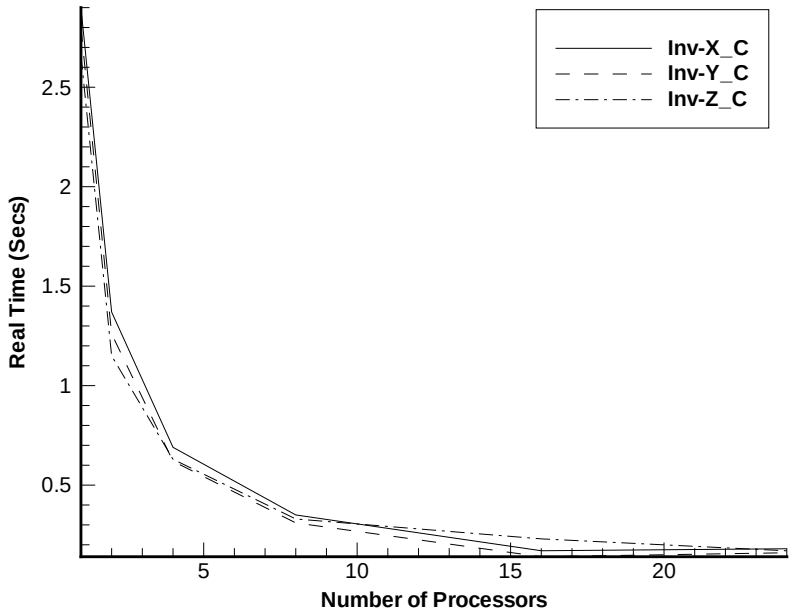

Figure 5.10: Parallel scalability of inviscid fluxes on coarse grid for the Hypervapotron Standard design.

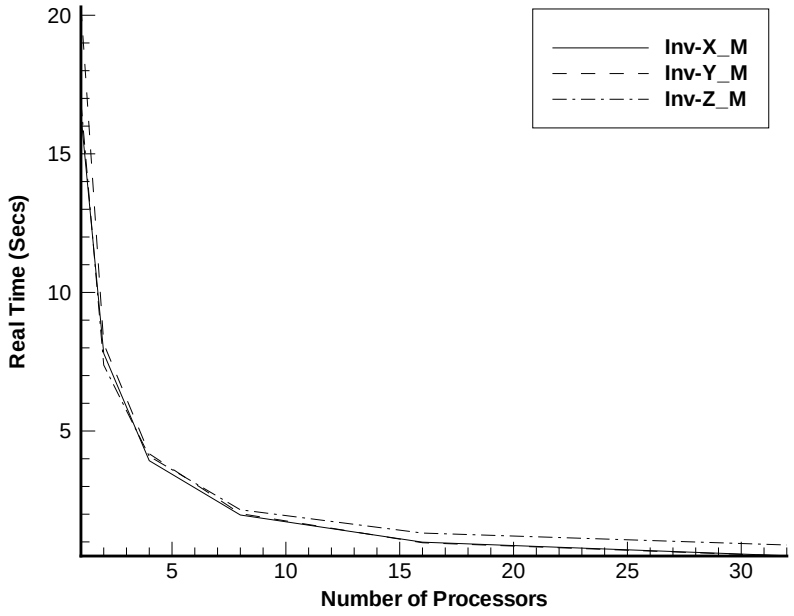

Figure 5.11: Parallel scalability of inviscid fluxes on medium grid for the Hypervapotron Standard design.

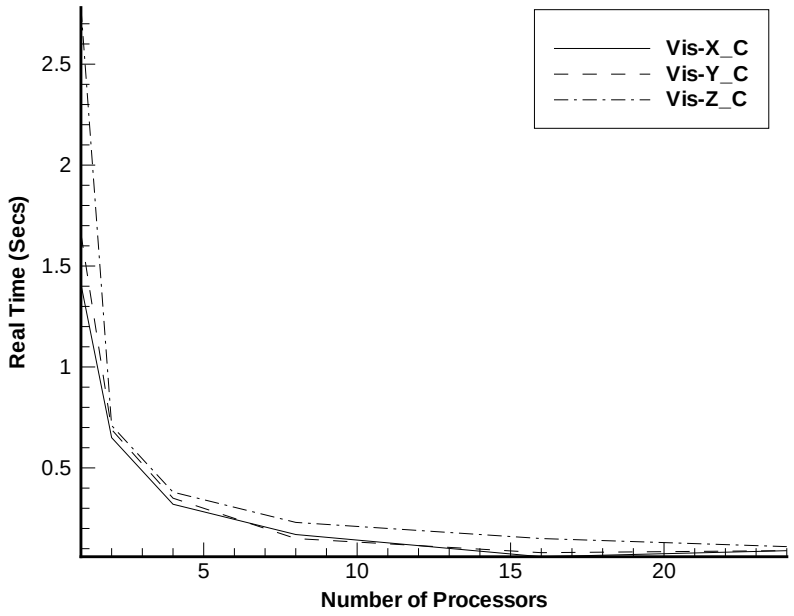

Figure 5.12: Parallel scalability of viscous fluxes on coarse grid for the Hypervapotron Standard design.

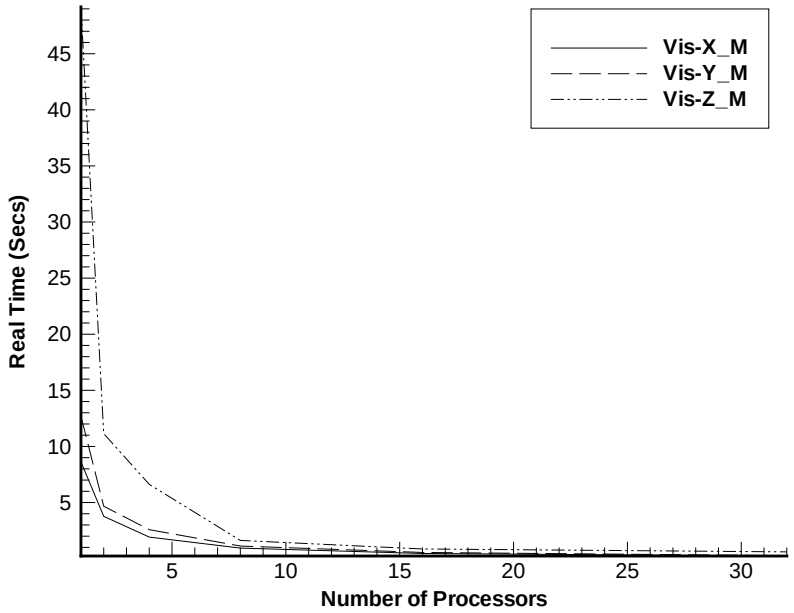

Figure 5.13: Parallel scalability of viscous fluxes on medium grid for the Hypervapotron Standard design.

5.5 Case Matrix

The single cavity simulations are focused on accuracy and achieving high quality results for the turbulent behaviour in the flow field. The impact of the reconstruction order and grid resolution are also important parameters that can be considered in detail within this less computationally expensive environment. In addition, simulations have been conducted for the proposed three cavity arrangement model on a coarse grid. The computational requirements for a full and comprehensive resolution of the coupled problem requires the use of a parallel computing facility to gain the transient behaviour in any reasonable timescale. Further, the results presented are preliminary and simulations are subject to further grid refinement and a sizeable increase in grid nodes to achieve a grid independent flow solution. The breakdown of the converged cases run, i.e. the case matrix is presented below in Figure [5.14]. Results were a very large dataset including cases that required further run-time resulting in a non-converged state. The author has refrained from showing excessive quantities of material that do not aid discussion for such cases and the matrix presented shows only the converged solutions which are also discussed in the results section.

5.5.1 Boundary and Initial Conditions

Different boundary conditions where specified in each case with regard to the temperature scalar. The solid-fluid interface modelling requires introduction of a mesh for the solid part and this increases the computational requirement two fold when based on the two dimensional cases. Therefore, in addition to direct conjugate modelling of the solid, constant temperature boundary conditions were employed in the single cavity cases after the flow field and boundary layer had established. This provided a less computationally expensive set of cases (i.e. less the solid sections).

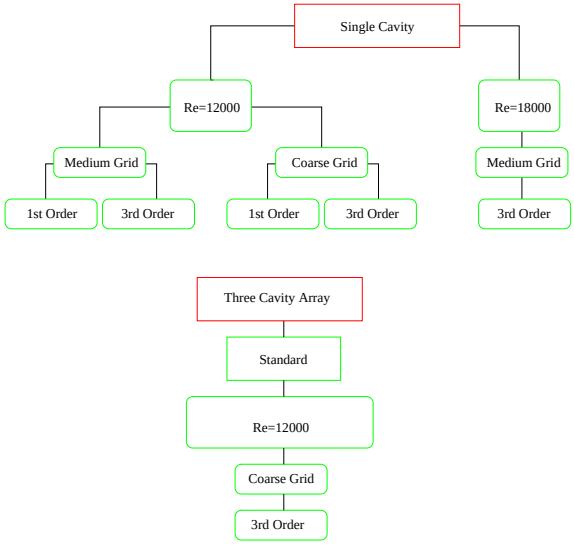

Figure 5.14: Hypervapotron case matrix.

The boundary and initial conditions are outlined for all cases and the reader is reminded that the procedure was repeated on both coarse and medium grids. A turbulent Pouseille plane channel flow is defined when the Reynolds number $\simeq$ 5772.22, Orszag (1971). The Reynolds number, based on the cavity width, lies between 12000-18000 for corresponding mean inflow speeds of 4-6m/s respectively, i.e.:

$$Re = \left(\frac{u_c^* l_c^*}{\nu^*}\right) = \frac{4 \cdot 3 \cdot 10^{-3}}{1.004 \cdot 10^{-6}} \simeq 12 \cdot 10^3 \tag{5.4}$$

Periodicity was applied in both the streamwise and spanwise directions in order to simulate the recurrent geometry that occurs in the main section of the Hypervapotrons. Over 250 cavities exist in the Hypervapotron main sections and it is believed that the impact of entrance and exit effects occur far upstream and downstream from a significant portion of the main section.

Both single cavity and three cavity models have been considered with different temperature boundary conditions for each case.

The single cavity simulations only consider the fluid part of the domain. The tem-

perature variable at the wall in the single cavity simulations is assumed constant. The three cavity cases have both fluid and solid incorporated into the domain and the conjugate solver recovers the interface temperatures based on far field, constant, temperature conditions.

It was not deemed feasible to model the end wall effects on the flow and therefore the applicability of the results obtained here are of greater interest to designs that maintain extended spanwise dimensions of the Standard geometries. The periodicity applied in the spanwise faces is justified by the long spanwise length of the devices in comparison with cavity width. The spanwise dimension is exactly 16 times the cavity width, however, the impact of the end walls would have a significant effect on the flow field solution and therefore the overall heat transfer behaviour.

An initial run for approx. 4000 time steps with a convergence criteria of 0.001 and time step size of 0.01 was used to gain an established flow. Sampling of averages and fluctuations was conducted over a time window of 2000 time steps with a time step size of 0.005. The temperature scalar was introduced after these time periods and ran for an additional (approx.) 2000 time steps with a time step size of 0.01. A similar procedure was adopted for all other cases.

Single Cavity

Single cavity simulations did not contain the solid part in the model. The simulations were a good indicator for grid resolution requirements as a precursor to the three cavity simulations. It was expected that the single cavity simulations were able to achieve far longer time durations due to the sizable reduction of grid nodes. The initial condition at time $t_0 = 0$ was a 10 percent random perturbation on all variables apart from temperature which was initially set to zero until the flow has developed:

$$p = 1., \quad u = 1 + 0.1\epsilon, v = w = 0.1\epsilon, \quad T = 0 \tag{5.5}$$

Here ϵ is defined as a random number ranging from 0 to 1. Since the pressure corresponding to the perturbed flow is recovered on the first time step, it is sufficient to leave it constant in the initialisation. Also the following boundary conditions, at wall surfaces, were enforced during the flow development stage:

$$u = v = w = T = 0 \tag{5.6}$$

In the streamwise axis, domain faces for the inlet and outlet of the geometry are defined as periodic and therefore the boundary conditions here are expressed by:

$$\begin{cases} u(x_0, y, z) = u(x_1, y, z) \\ v(x_0, y, z) = v(x_1, y, z) \\ w(x_0, y, z) = w(x_1, y, z) \\ T(x_0, y, z) = T(x_1, y, z) \\ p_p(x_0, y, z) = p_p(x_1, y, z) \end{cases} \tag{5.7}$$

Where x_0 and x_1 correspond to the start and end of the computational domain in x respectively and p_p corresponds to the periodic counterpart of the pressure field. The forcing term was initially set to zero. The flow field variables for the spanwise direction are periodic and boundary conditions on spanwise boundaries are as follows:

$$\begin{cases} u(x, y, z_0) = u(x, y, z_1) \\ v(x, y, z_0) = v(x, y, z_1) \\ w(x, y, z_0) = w(x, y, z_1) \\ T(x, y, z_0) = T(x, y, z_1) \\ p_p(x, y, z_0) = p_p(x, y, z_1) \end{cases} \tag{5.8}$$

Here z_0 and z_1 correspond to the start and end of the computational domain in z respectively.

The flow statistics were initially gathered from the sampling run with a nullified

temperature field. Afterwards, the following temperature boundary conditions were applied for the heat transfer simulations, $T_{su} = 0$ (upper wall) and $T_{sl} = 1$ (lower wall). The time required for flow development varied between the cases and is discussed separately.

Three Cavity Array

A perplexing feature of the Hypervapotron flow physics is the vast range of turbulent scales that exist and the global and local variation of the flow field features and their interdependency. For this reason the simulation criteria for a number of cavities is evident. The number of cavities in the domain limits the largest scales available in the flow field and the longest wavelengths. However the computational cost of additional cavities limits the number to three. Simulations of this type included the solid walls as part of the domain. Further, with the introduction of the solid alloy in the domain any more cavities would be unfeasible within the current time constraints based on estimates with the available computing hardware.

The wall heat fluxes and Nusselt number corresponding to the convection of the high temperature from the wall surface was a focus for the three cavity array cases. The implementation of the conjugate heat transfer model is realised through the three cavity simulations which where intended to resolve the interface temperature field at the surface where the boundary condition was applied. The simulation procedure was the same as for the single cavity, however, once the flow has developed and the statistics for the flow obtained, temperature field was re-initialised with $T_s = 1.0$ in the solid region. The computations then proceeded to determine the heat transfer properties with the following temperature boundary conditions, $T_{su} = 0$ and $T_{sl} = 1$.

5.6 Results and Discussion

This study was conducted using fully three dimensional transient simulations for the flow field and heat transfer in the three cavity array simulations. Further understanding of the flow structure and heat transfer present within the Hypervapotron, Standard design prior to boiling conditions has been established here.

Streamribbons, contour plots and time averaged velocity vectors are shown within this section to facilitate discussion. Temperature plots of the wall surfaces and heat fluxes are provided for both the single and three cavity array cases.

The Hypervapotron flow field is primarily described along centrelines as in the lid driven case. The data presented here was extracted from the spanwise symmetry plane. The reason for this was the excessive storage requirement for the case.

It was an expectation that future experiments of the (scaled up) Hypervapotron geometries would be realised using LDA techniques similar to recorded measurements as in the lid driven cases, see Prasad & Koseff (1989). This would provide piecewise data at desired locations corresponding to cell centres on the current grids.

5.6.1 Single Cavity

Time Traces, Markers and Averaging

Four distinct stages of computation may be identified during these simulations. These are flow initialisation, the averaging window, sampling of turbulent properties and finally, sampling with the temperature field. The schematic of this process is shown in Figure [5.15].

The sampling intervals for each case are summarised in the Table 5.4. Both the medium cases have run for significantly less time than the coarse cases due to com-

putational load.

In order to estimate whether the flow has developed, data on marker points in the flow at fixed locations within each block have been recorded. The spatial location corresponds to the cell centre of the lower left corner cell for each block. The transient data that has been recorded is a time trace of the component of the velocity variables, u or v.

The grid schematic, see Figure [5.16] indicates the numbering of the blocks which corresponds to the marker locations that are always defined at the lowest left corner cell centre for each block.

Within the single cavity simulations a total of 12 blocks and therefore 12 markers per z-slice were recorded. Such information is used to indicate the periodic and turbulent behaviour of the flow in specified locations.

ILES has demonstrated the ability to resolve turbulent flow structures sufficiently within a wall bounded domain (see Chapter 3) and markers have been used within the current case to indicate the flow establishment and a suitable initial condition to begin sampling of the desired turbulent data.

The analysis of all single cavity cases were assessed for flow and transport phenomena using both statistical data and three dimensional instantaneous variable

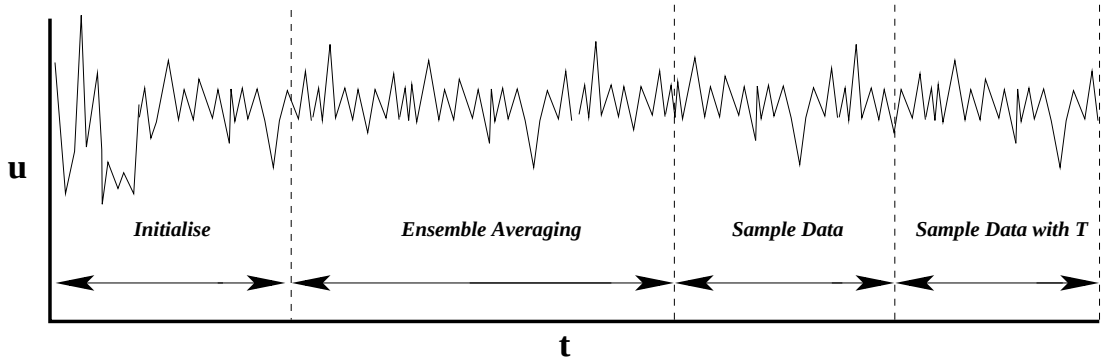

Figure 5.15: Decomposed time trace for the Hypervapotron single cavity cases showing specific time windows.

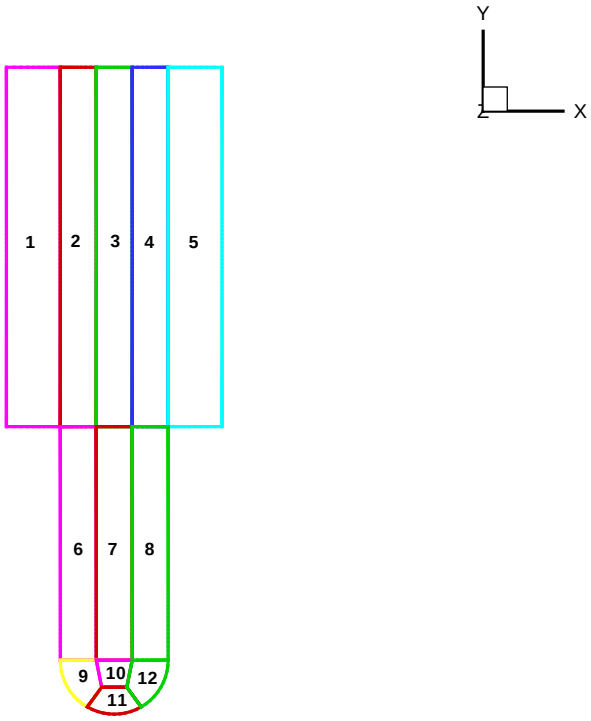

Figure 5.16: Schematic of the multiblock topology for the single cavity Hypervapotron cases with block numbers.

illustrations. As in the lid driven case several restarts of the computations were required to achieve a converged and developed flow field.

The locations of the markers almost all correspond to very near wall locations. They have been useful to identify the development of the viscous boundary layer within the channel and cavity, and shear layer over the cavity mouth.

Very useful information can be gathered from the unsteady signal in the shear layer at the top of the cavity, corresponding to marker points within blocks 2-5, see Figure [5.16].

Figures [5.17]- [5.19] show instantaneous values of v velocity in the shear layer above the cavity. The v velocity has been chosen here to highlight not only the unsteadiness but in addition, the amplitude of the fluctuations in the shear layer.

Coarse Single Cavity, Re 12000	1st Order	3rd Order
Sample	5	16
Medium Single Cavity, Re 12000	1st Order	3rd Order
Sample	16	5
Medium Single Cavity, Re 18000	1st Order	3rd Order
Sample	N/A	16

Table 5.4: Non-dimensional computational time durations for all single cavity cases.

The first order solutions for all cases show a periodic fluctuation at the cavity mouth with the amplitude growing along the shear layer and then decreasing at the impingement point. The amplitude of the fluctuations obtained with the first order of accuracy increases with grid refinement and the apparent frequency of the oscillations decreases. For both grids the motion is essentially laminar and no chaotic flow behaviour is observed.

The third order computations show a similar trend with the amplitude of the oscillations increasing along the shear layer and then decreasing at the impingement point. However, the oscillations exhibit distinctly chaotic nature. This is further highlighted in Figure [5.17] corresponding to the longest sampling interval on the medium grid. Figures [5.18] and [5.19] show the results on the coarse and medium Re=12000 cases by comparing both the first and third order results.

This suggests that in order to capture the turbulent flow, high order reconstruction must be employed based on current grid resolutions.

The character of the unsteady flow can be further illustrated with the behaviour of the mass flux in the correction algorithm and the corresponding forcing term. Figure [5.20a] shows the mass flux variation and comparison with the ideal mass flux for the coarse grid and third order scheme at Re=12000.

The mass flux is integrated on the inlet and outlet faces and the variation observed in the sixth digit of the mass flux occurs due to the error in the computation of the integral, which is a function of the flow distribution. Similar behaviour can be

observed for the forcing term, see Figure [5.20b].

At the same time the integral mass flux variation and the forcing term variation for the first order results shown in Figure [5.21] demonstrate purely periodic fluctuations with the same frequency as indicated by the markers in the shear layer. Note that the forcing term is negative as it corresponds to the slope of the linear component of pressure.

The information obtained from the time dependent behaviour of the shear layer and integral characteristics tends to suggest that turbulent flow behaviour is not resolved with the first order scheme on both grids. Under resolved simulation results in the periodic flow behaviour with highly grid dependent frequency. It further leads to a completely different flow structure as will be demonstrated in the next section.

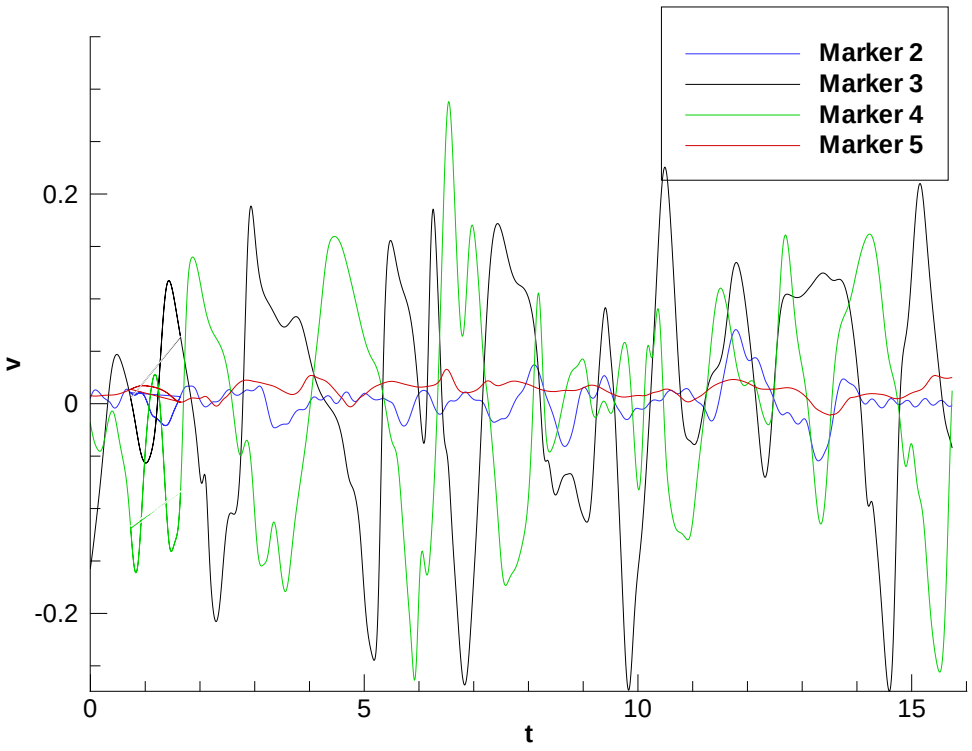

Figure 5.17: Instantaneous v velocity (markers 2-5) for Re=18000 on medium grid with third order reconstruction.

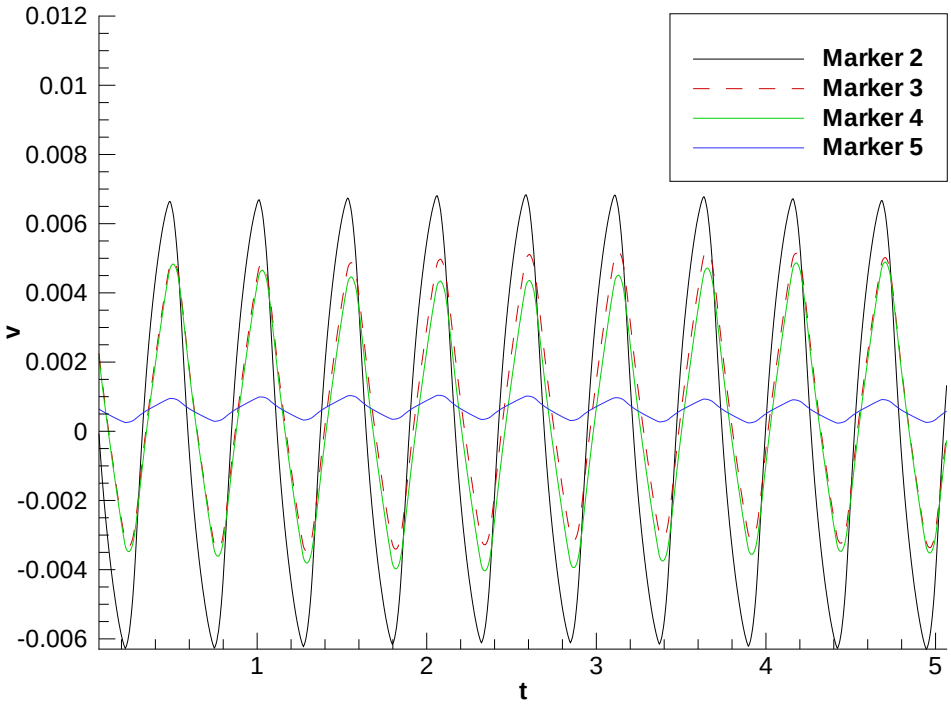

(a) First order reconstruction.

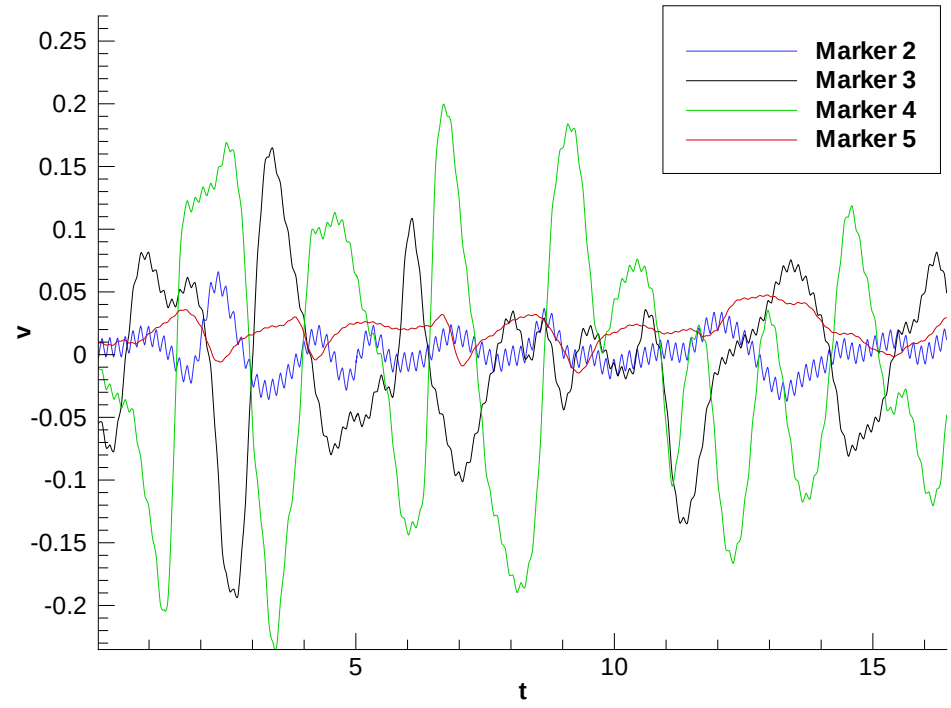

(b) Third order reconstruction.

Figure 5.18: Instantaneous v velocity (markers 2-5) for Re=12000 on coarse grid.

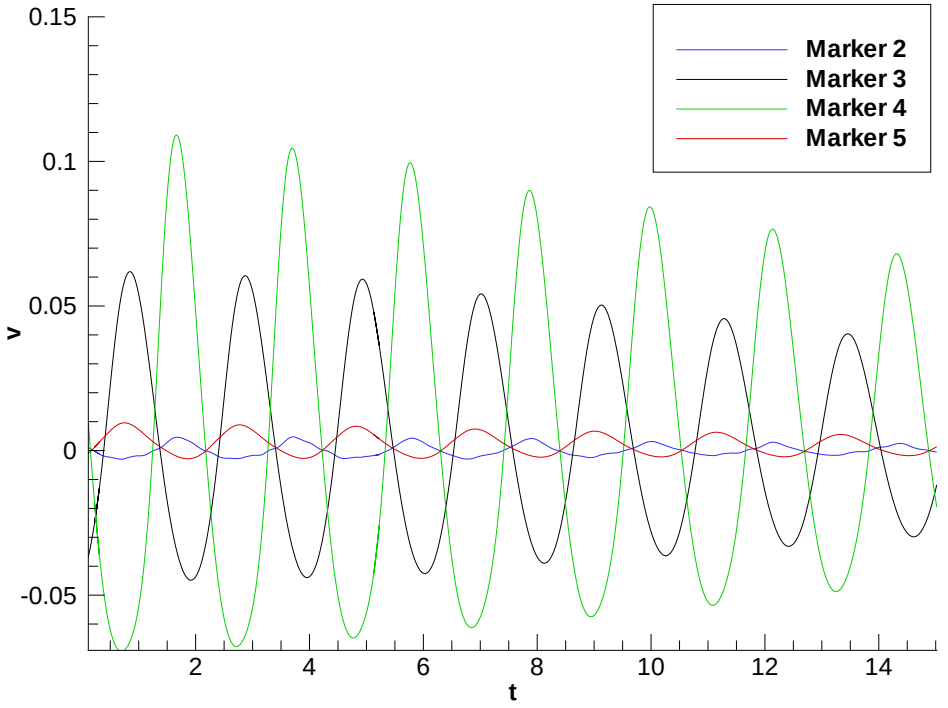

(a) First order reconstruction.

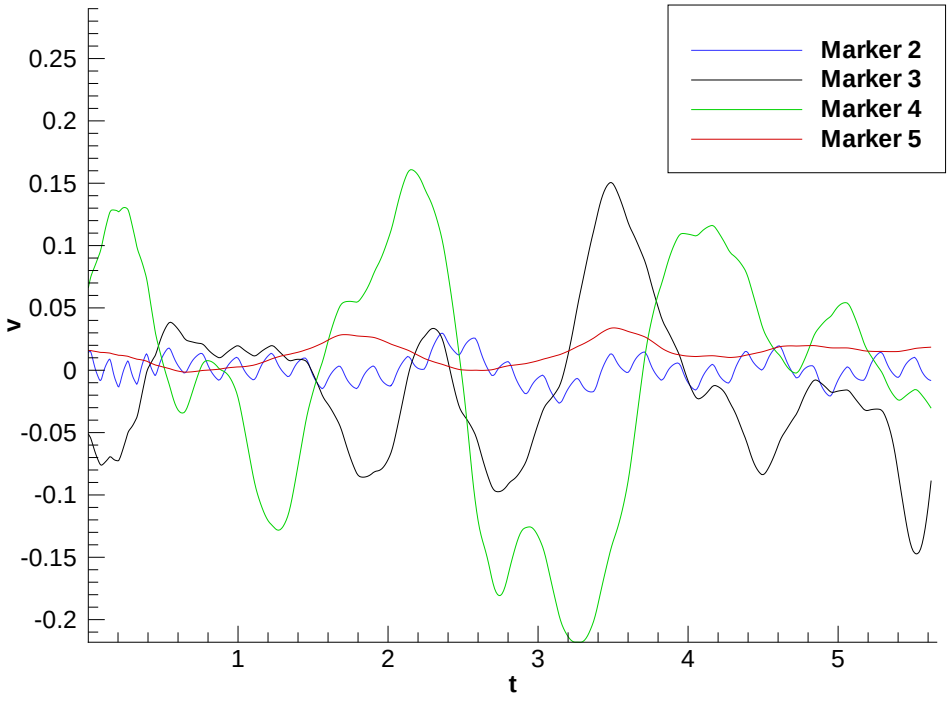

(b) Third order reconstruction.

Figure 5.19: Instantaneous v velocity (markers 2-5) for Re=12000 on medium grid.

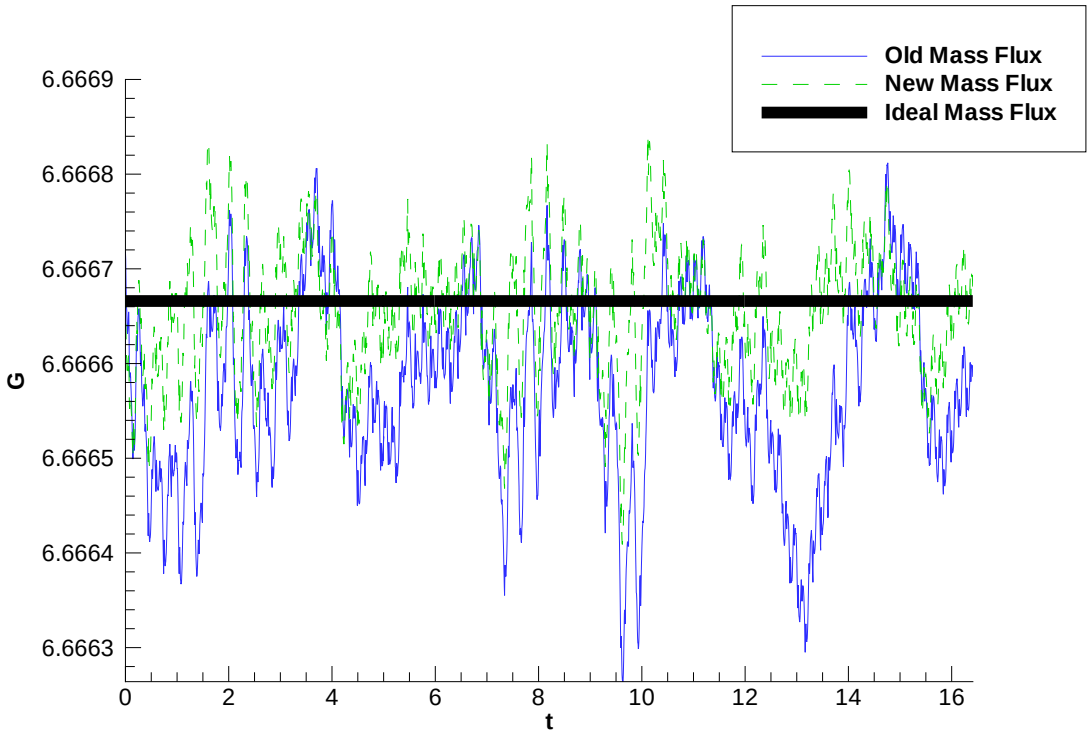

(a) Mass flux.

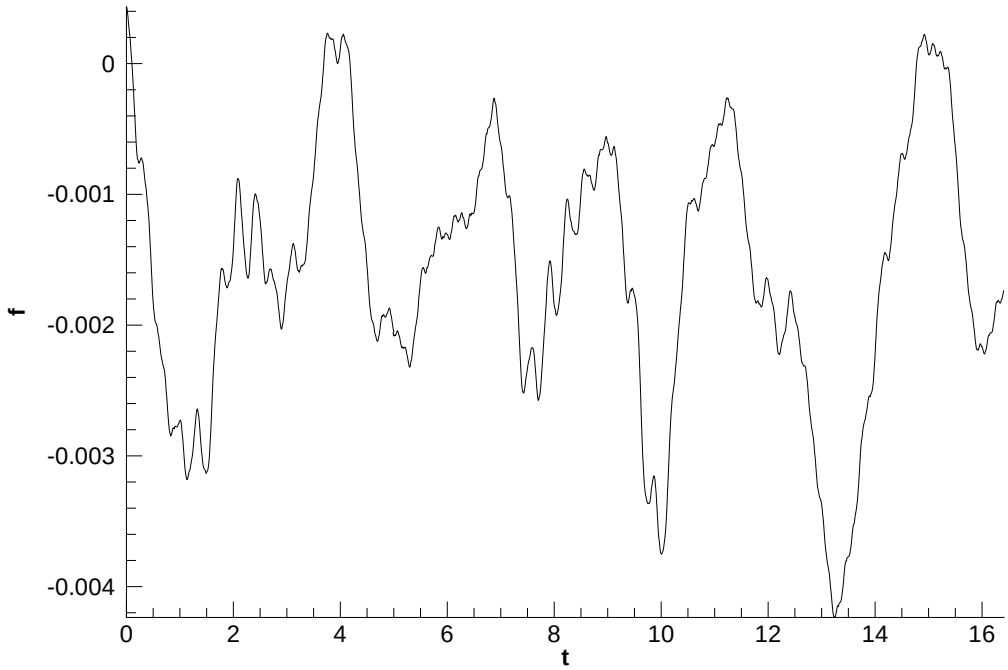

(b) Forcing term.

Figure 5.20: Forcing parameters for Re=12000 on coarse grid with third order reconstruction.

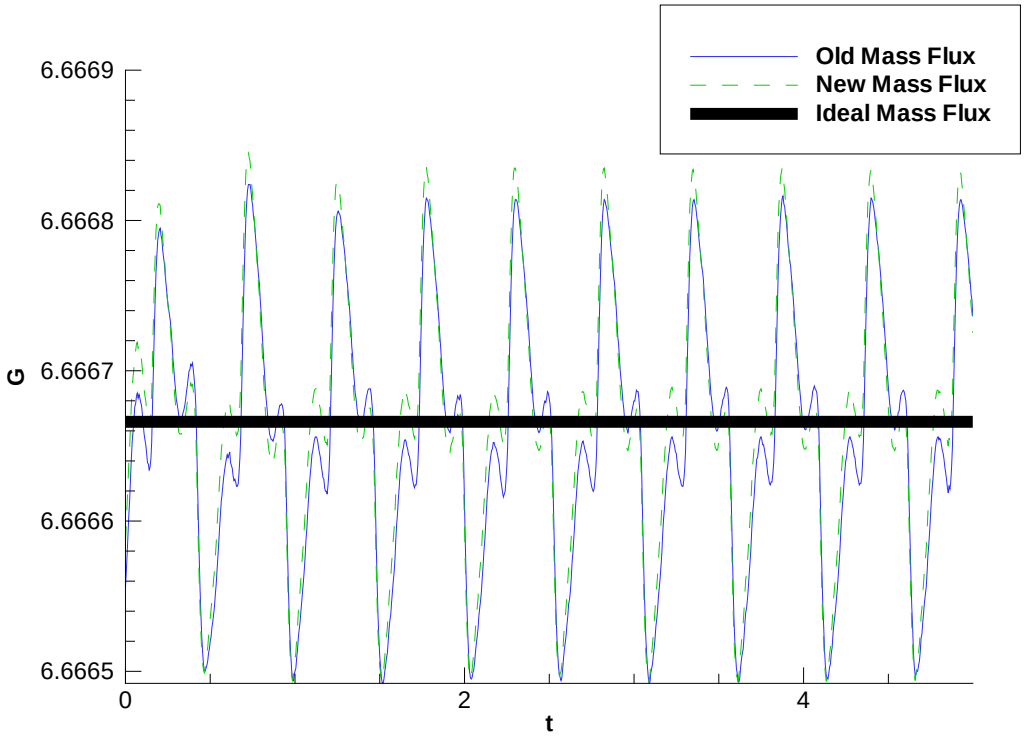

(a) Mass flux.

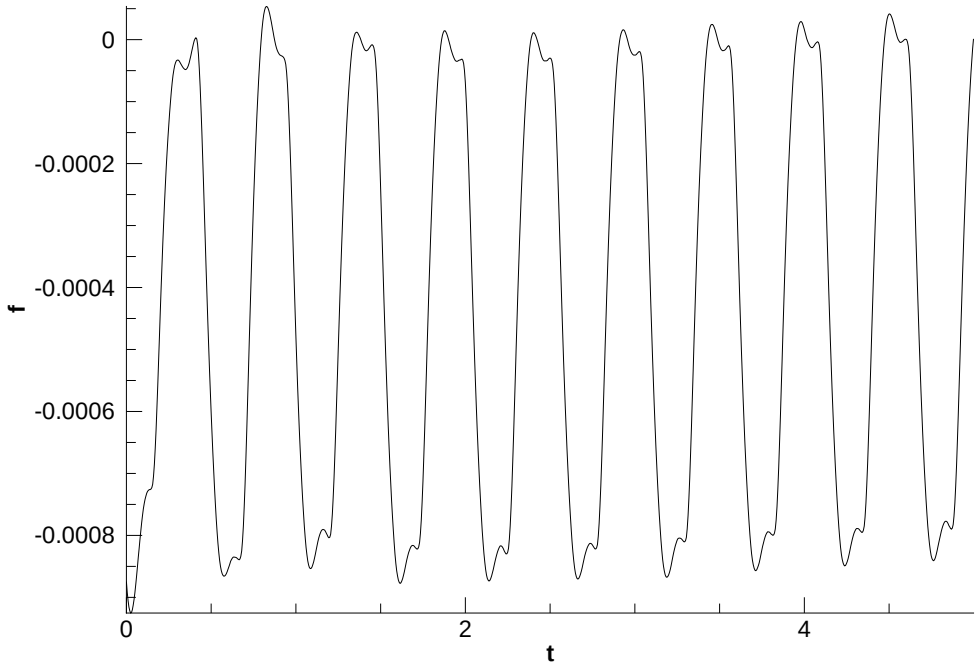

(b) Forcing term.

Figure 5.21: Forcing parameters for Re=12000 on coarse grid with first order reconstruction.

Averaged Flow Behaviour

In this section the topology of the flow resulting from different reconstruction schemes and grids is discussed. The author highlights that whereas the quantitative results for the data on reporting lines and heat transfer characteristics presented in the following sections have been sampled on each time step, this was not done for the complete flow field due to memory restrictions.

The averaged flow fields discussed here were averaged a-posteriori with the sampling interval of 100 time steps. While sufficient for the qualitative analysis of topology, this approach cannot be used to determine turbulent characteristics for the complete flow.

Figures [5.22] and [5.23] show the instantaneous streamribbons coloured by v velocity obtained with the first and third order of reconstruction at Re=12000 on the coarse grid.

The difference in the topology is immediately seen with the first order solution leading to a single recirculation zone in the cavity. However, the third order case results in two separate flow regions with a strong vortex at the cavity mouth and a weaker counter rotating vortex observed at the bottom of the cavity.

Due to the presence of the large primary vortex, the weak secondary vortex is generated at the base. Vortex shedding out of the cavity occurs due to the unsteady nature of the secondary flow generated by the primary vortex.

Therefore, it has been shown that high order reconstruction is a prerequisite for the current numerical formulation in order to capture sufficient flow physics, based on current grids.

In order to describe the averaged flow behaviour, averaging has been performed in the sampling interval for all cases concerned. In order to establish the flow

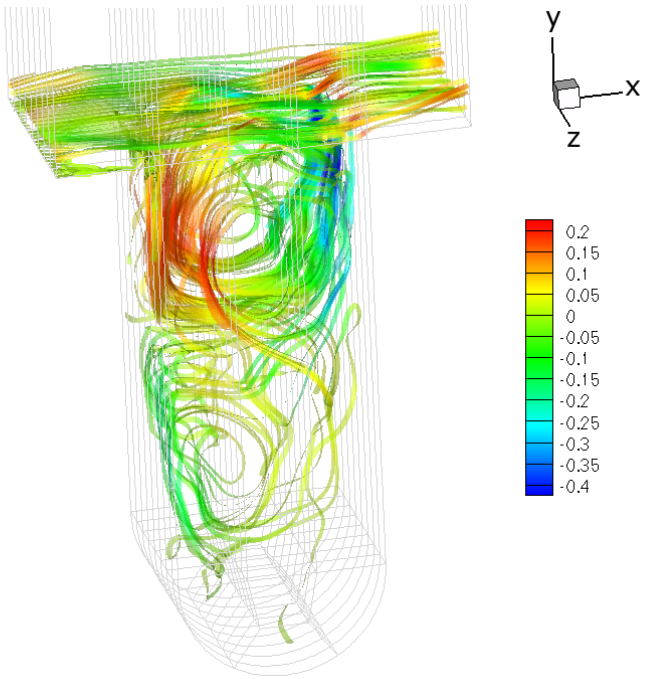

Figure 5.22: Instantaneous streamribbons with v velocity flood for medium grid with third order reconstruction for Re=12000.

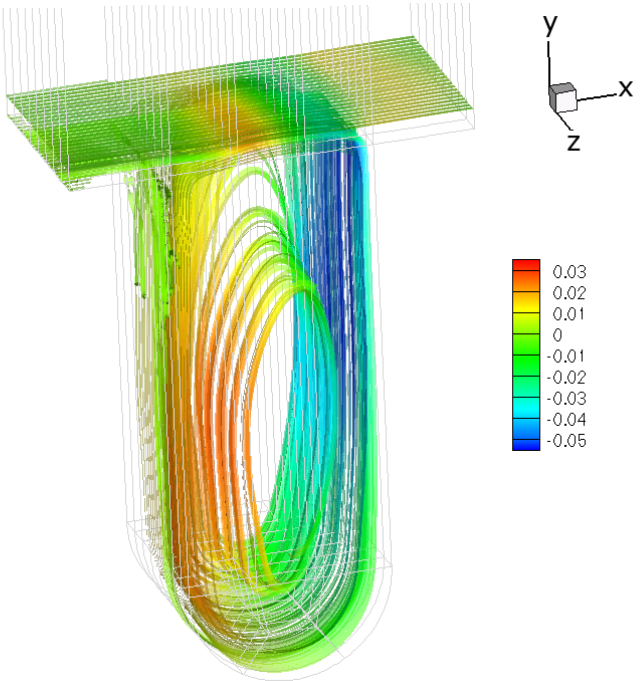

Figure 5.23: Instantaneous streamribbons with v velocity flood for medium grid with first order reconstruction for Re=12000.

topology in two dimensions, in addition to time averaging; spatial averaging has been performed along the z direction. The results allow a qualitative comparison of flow structure with two dimensional RANS results reported by Milnes & Drikakis (2009).

Figures [5.24]-[5.27] show streamlines of time-space averaged flow superimposed on the contours of the v velocity. The results indicate that while the first order solver on both grids leads to a single vortex in the cavity similar to under resolved RANS (SST $k-\omega$) results in Milnes & Drikakis (2009), the third order in all cases leads to a two vortex structure observed in resolved RANS computations. A further grid increase in RANS would result in a third vortex at the bottom of the cavity but the grid densities required would be too slow to run in a time dependent three dimensional ILES simulation.

The formation of a third vortex close to the cavity base can be observed in Figure [5.26] for Re=12000. An additional feature which appears in the third order results but is not present in RANS results of Milnes & Drikakis (2009) is the small corner vortex below the separation point in the upstream edge of the cavity. The vortex is present at both Reynolds numbers and is not captured with the first order solver.

One may also note that the flow speeds within the cavity are largely dependent on the resolution of the shear layer which separates at the downstream corner and splits into the cavity.

Such qualitative analysis of the flow indicates that the solution obtained with the first order reconstruction on all grids does not demonstrate physically correct behaviour and the first order results are excluded from further discussion for the flow description. Another important check for all the cases was the value of $y+$. The averaged $y+$ values at the first cell centre from the channel walls was 5 and 10 for the medium and coarse cases respectively.

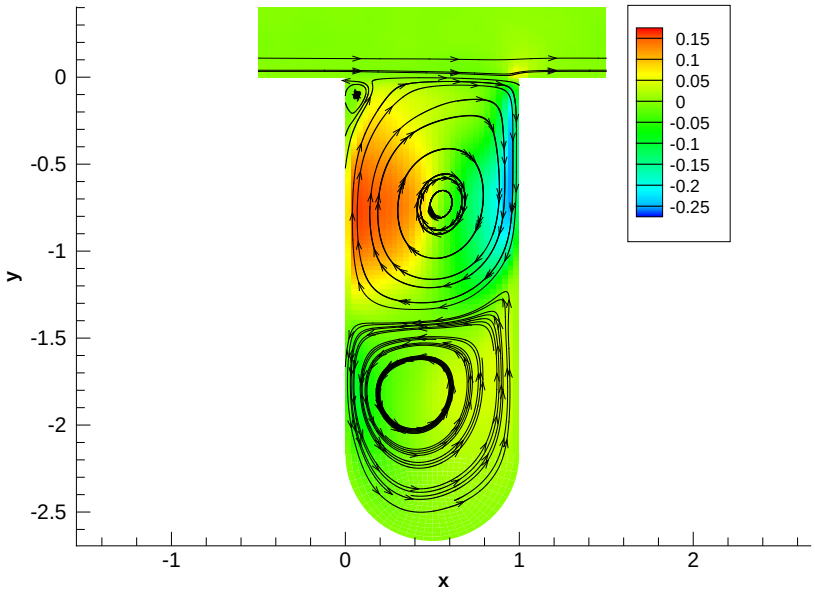

Figure 5.24: Time-space averaged flow for Re=12000 with third order reconstruction on the coarse grid with contours of the ensemble $< v >$ component of velocity and streamlines.

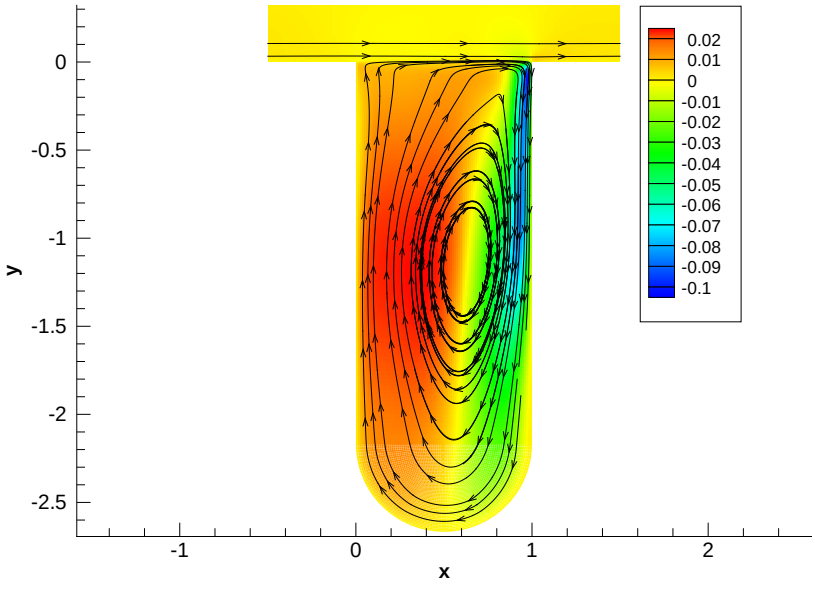

Figure 5.25: Time-space averaged flow for Re=12000 with first order reconstruction on the medium grid with contours of the ensemble $< v >$ component of velocity and streamlines.

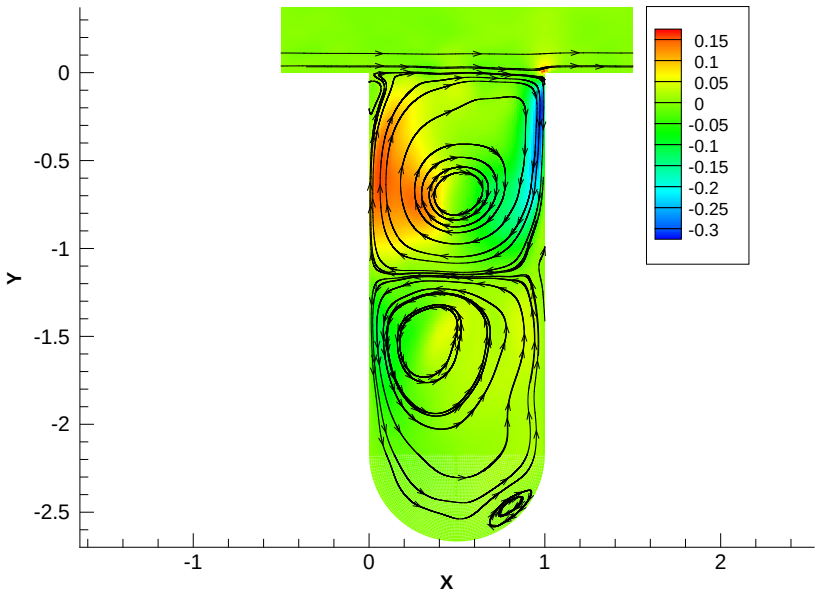

Figure 5.26: Time-space averaged flow for Re=12000 with third order reconstruction on the medium grid with contours of the ensemble $< v >$ component of velocity and streamlines.

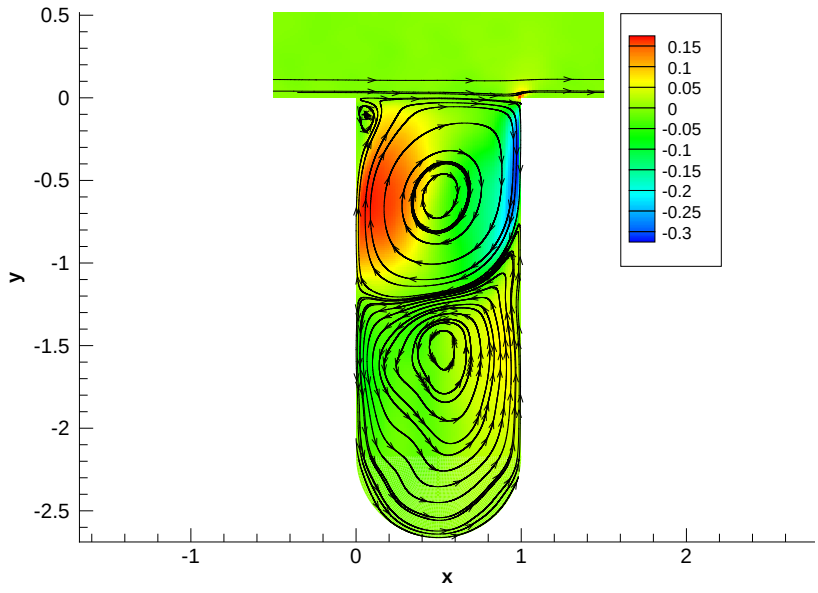

Figure 5.27: Time-space averaged flow for Re=18000 with third order reconstruction on the medium grid with contours of the ensemble $< v >$ component of velocity and streamlines.

Line Data

Statistical data was obtained indicating the flow field behaviour in discrete locations in both the channel and cavity regions. The data is analysed along the centrelines (in the spanwise symmetry plane) that cross the cavity mouth horizontally and vertically, i.e. X1 and Y2 Lines shown in Figure [5.28].

The position of the lines in the computational domain is as follows:

- Line X1: Y=0.0001, Z=1.
- Line Y1: X=-0.25, Z=1.
- Line Y2: X=0.5, Z=1.
- Line Y3: X=1.25, Z=1.

Figure [5.29] shows the average u velocity on Line Y2 for Re=18000 at the end of the sampling interval and 100 time steps ($\simeq$ 1/5th of the sampling window) before the end of the sampling interval.

The results indicate that the averages for these cases have converged with respect to the sampling time window selected. All other cases showed similar convergence of statistics prior to sampling of turbulent properties.

The viscous boundary layer is developed in all cases and flow structure is shown for both Re=12000 and Re=18000 modelled on medium grids. Unfortunately, grid independence was not achieved. Further, it is expected that the flow is still under resolved.

However, it is suggested that the attributes of the key flow structure have been established and the findings presented here provide a significant advancement in the understanding of the key flow structure topology.

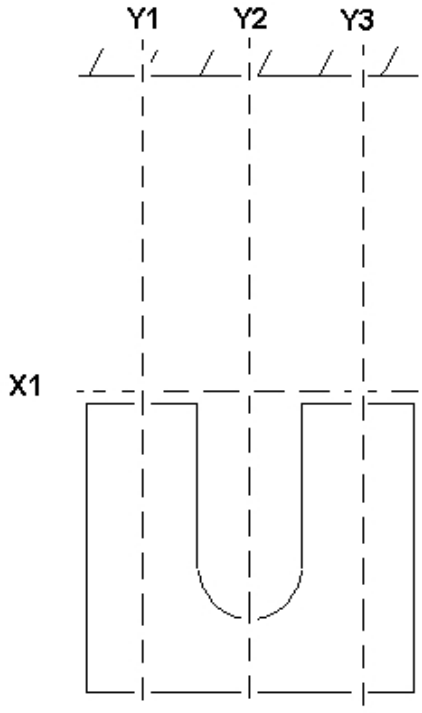

Figure 5.28: Schematic for reporting lines locations in single cavity cases.

The averaged two dimensional flow patterns presented in Figures [5.24]-[5.27] indicate that the solution varies between the coarse and medium grid. Indeed, the examination of the streamwise velocity and its fluctuation presented in Figure [5.30a] indicates that the solution is not fully grid converged.

Here the distributions are presented on Line Y2 in the middle of the cavity from the bottom of the cavity, located at -2.6 to 1, with 0 corresponding to the top of the cavity.

The vortex boundary position as indicated by the negative peak in the streamwise component of the velocity in Figure [5.30a] is similar in both cases, but the shear layer is much thicker on the coarse grid. This effect can be attributed due to excessive dissipation leading to a more laminar incoming boundary layer on the coarse grid.

The maximum of the streamwise Reynolds stress is observed in the shear layer above the cavity top (see Figure [5.30b]) with the same position predicted on both grids, but a difference of $\sim 20\%$ in the peak magnitude.

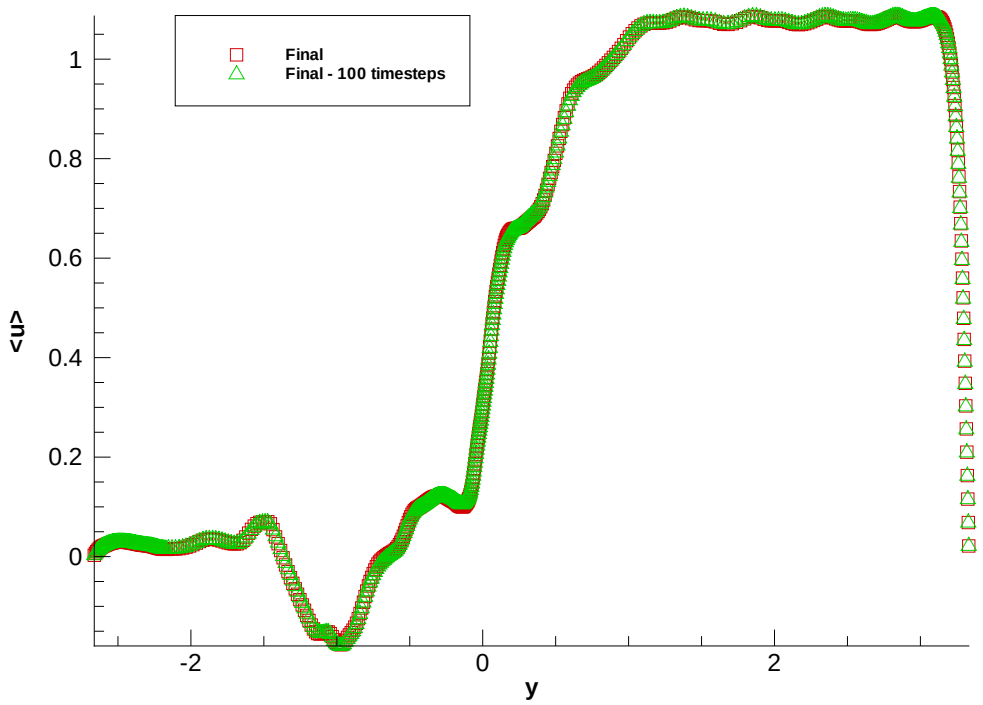

Figure 5.29: Convergence of averages on Lines Y2 over time for the third order scheme with Re=18000 on the medium grid.

These observations suggest that out of the set of available results, the best candidates for the flow analysis are given by medium grids.

Figures [5.31] and [5.33] show the comparison between the solution obtained at Re=12000 and Re=18000 on upstream and downstream lines Y1 and Y3.

The boundary layer above the cavity is more perturbed in the case of Re=18000, which manifests itself both in the thickness of the boundary layer (see Figures [5.31a] and [5.31b)]) and in the higher streamwise and vertical Reynolds stresses (see Figures [5.33a] and [5.33b]).

One may notice a slight asymmetry which is more prominent in the stresses and this may indicate that a single repeating unit is not adequate for the problem, considering the averages have converged.

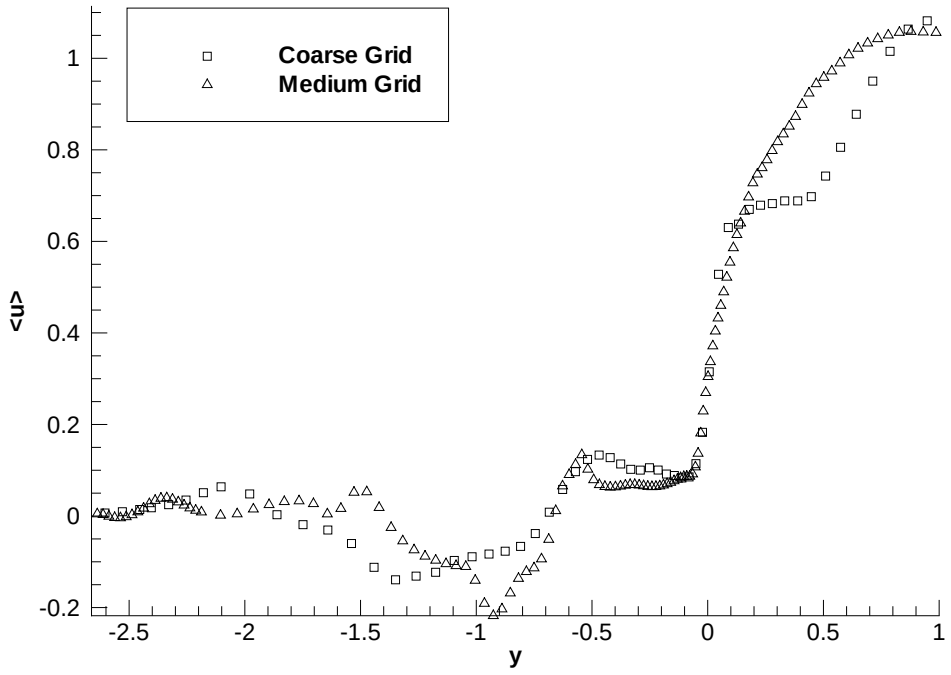

(a) Ensemble $< u >$ velocity component on Line Y2.

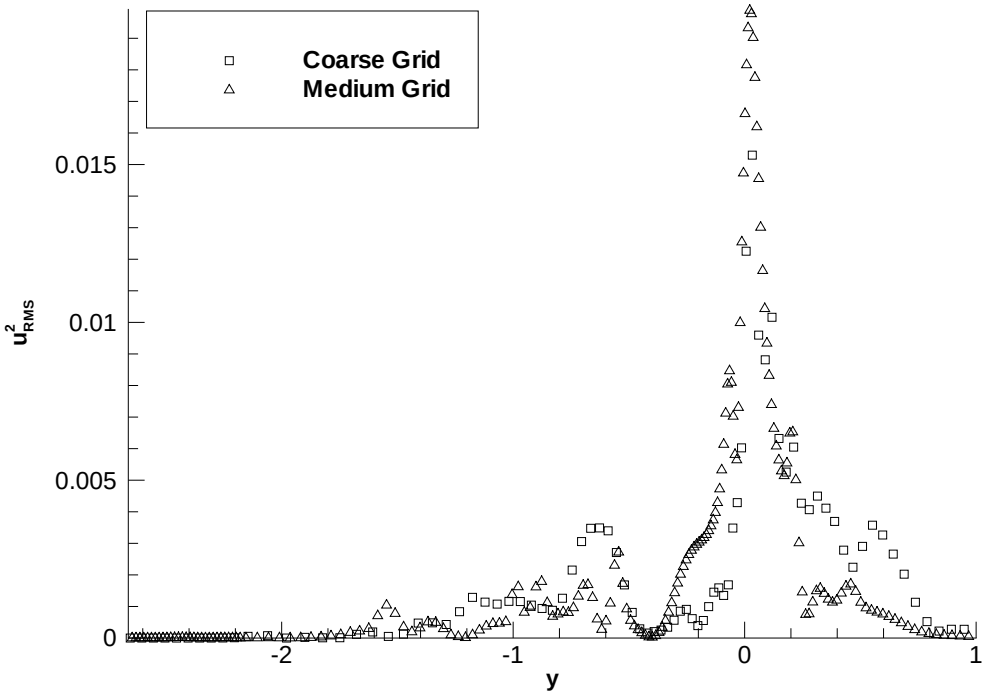

(b) u^2_{RMS} velocity component on Line Y2.

Figure 5.30: Impact of grid dependency on Line Y2 with third order reconstruction for the Re=12000 case.

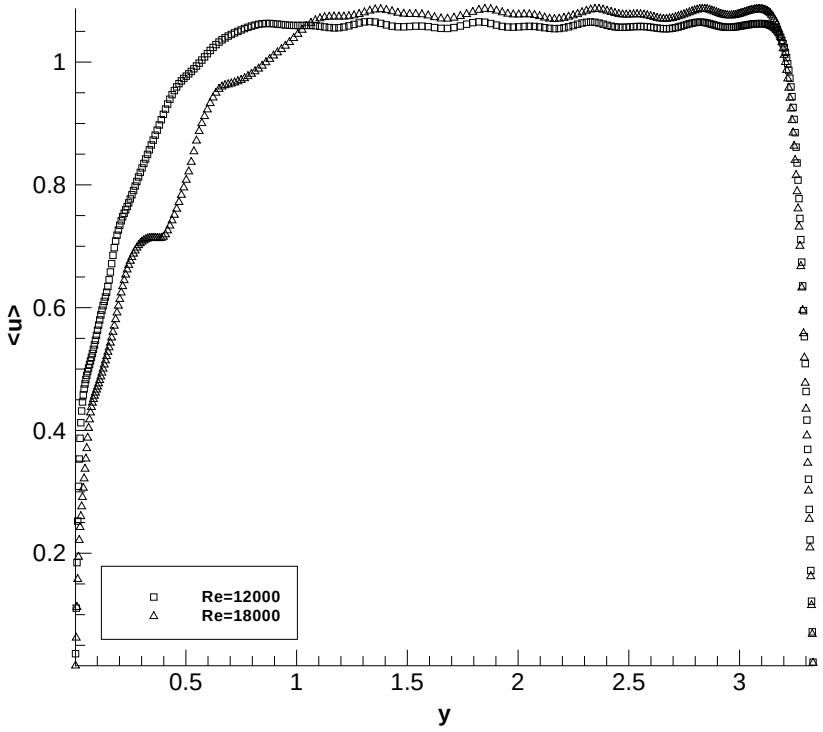

(a) Ensemble $< u >$ along Line Y1.

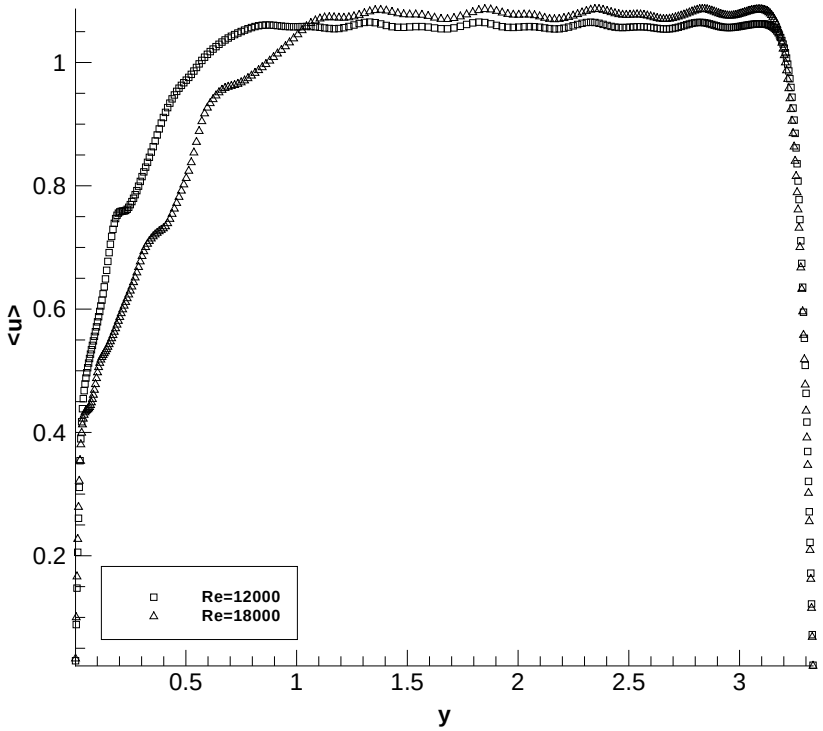

(b) Ensemble $< u >$ along Line Y3.

Figure 5.31: Ensemble $< u >$ for Lines Y1 and Y3 with third order reconstruction on the medium grid.

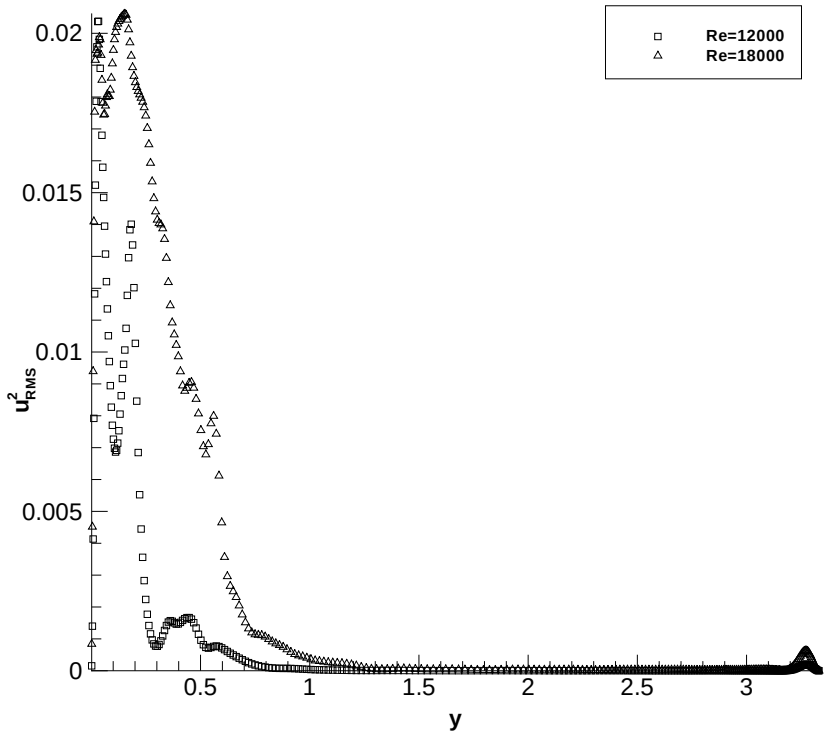

(a) u^2_{RMS} along Line Y1.

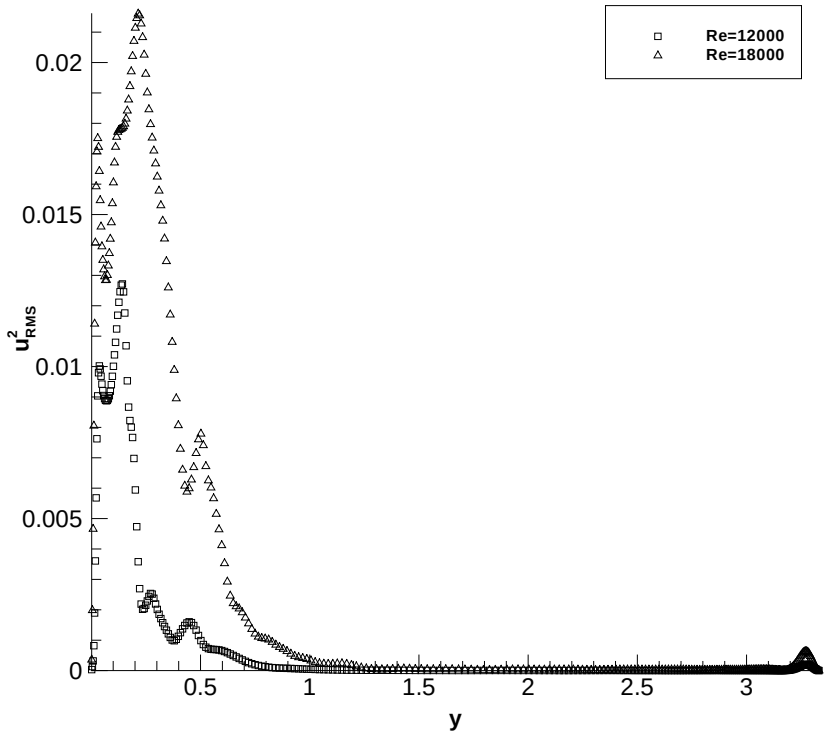

(b) u^2_{RMS} along Line Y3.

Figure 5.32: u^2_{RMS} for Lines Y1 and Y3 with third order reconstruction on the medium grid.

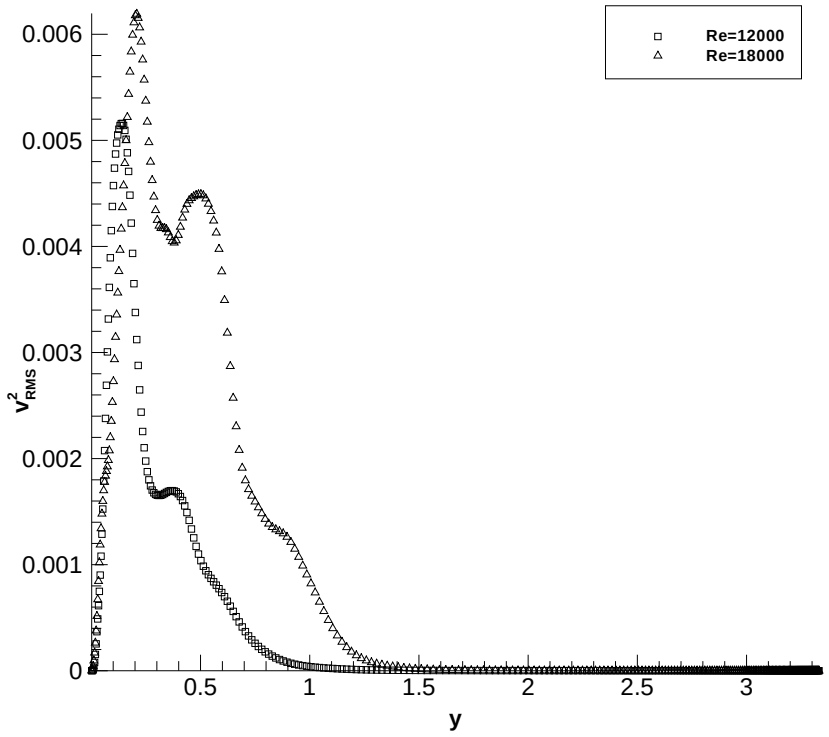

(a) v^2_{RMS} along Line Y1.

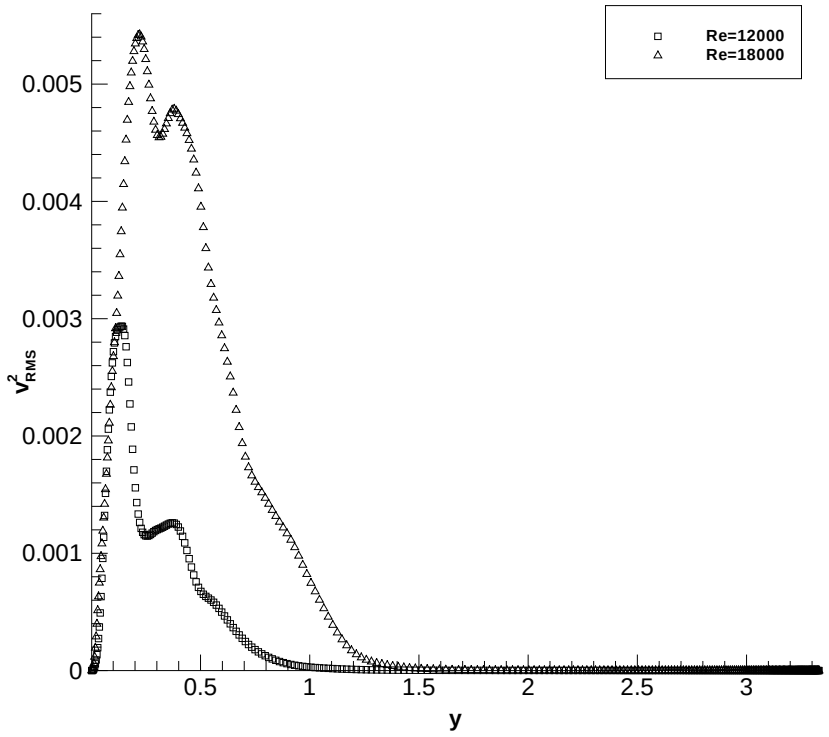

(b) v^2_{RMS} along Line Y3.

Figure 5.33: v^2_{RMS} for Lines Y1 and Y3 with third order reconstruction on the medium grid.

Comparisons on Line Y2 passing through the middle of the cavity are presented in Figure [5.34]. This indicates that the topology of vortices in the cavity is the same at both Reynolds numbers and the boundary between the vortices corresponding to the local maximum in u-velocity (see Figure [5.34a]) is at the same position.

The streamwise stress however develops an additional extrema in the secondary vortex region.

Referring to the position of the secondary vortex core as indicated by the averaged streamlines in Figures [5.24]-[5.27], this may be due to the centered position of the vortex core for the Re=18000 case as opposed to its shifted position to the upstream corner for the Re=12000 case.

Figure [5.35] presents the comparisons at Line X1 passing above the cavity. While the velocity profiles are similar in both cases, the peak of the streamwise Reynolds stress is observed in the developing region of the shear layer at Re=18000, while at Re=12000 it moves towards the downstream cavity corner.

The origins of this different behaviour can be understood by referring back to the time-space averaged flow.

Figures [5.36] and [5.37] show the contours of the v velocity for both cases taken at 0 and ± 0.001 to illustrate the regions of positive and negative v velocity in both cases.

For Re=12000 the interaction between the small corner vortex and the main shear layer creates the first maximum in the stresses. The second maximum is observed in the downstream part of the shear layer where it accelerates.

For Re=18000, the corner vortex is more pronounced and the maximum corresponding to the interaction between the corner vortex and the shear layer is at a higher value than the downstream section.

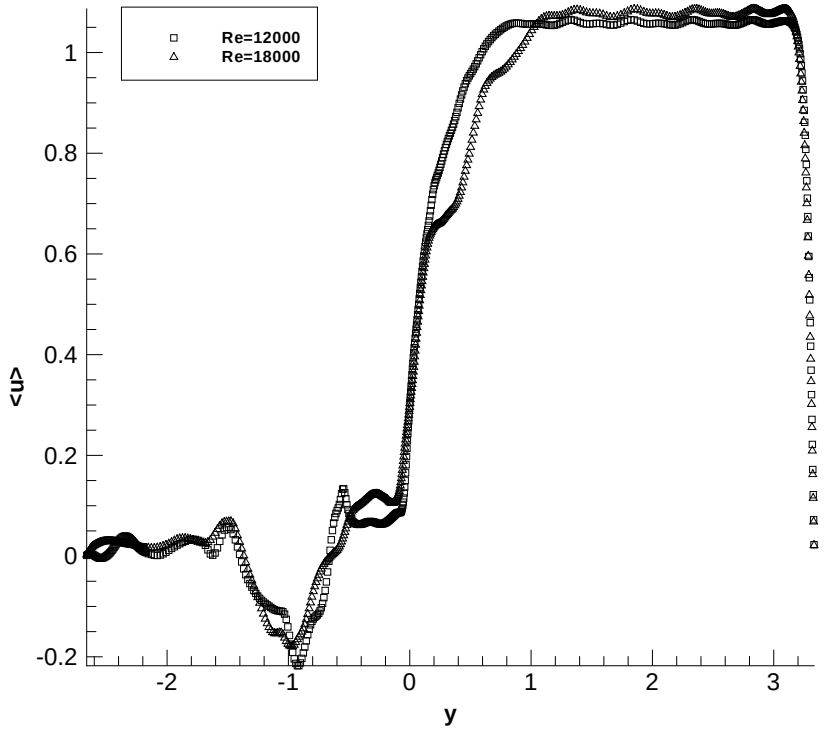

(a) Ensemble $< u >$ component of velocity.

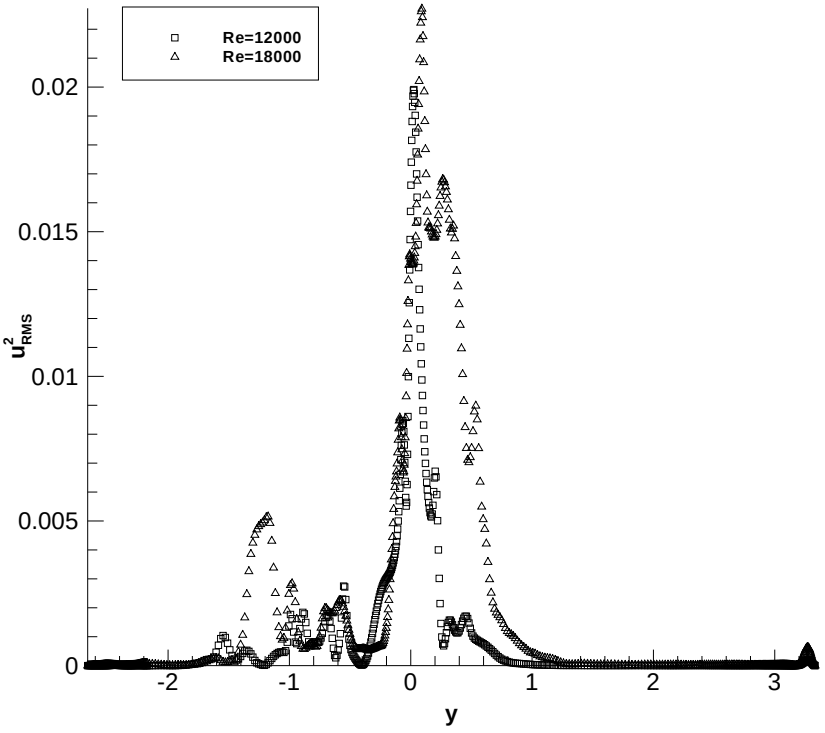

(b) u^2_{RMS} component of velocity.

Figure 5.34: Comparison of Reynolds number effect on mean and fluctuating velocity components along Line Y2 on medium grids with third order reconstruction.

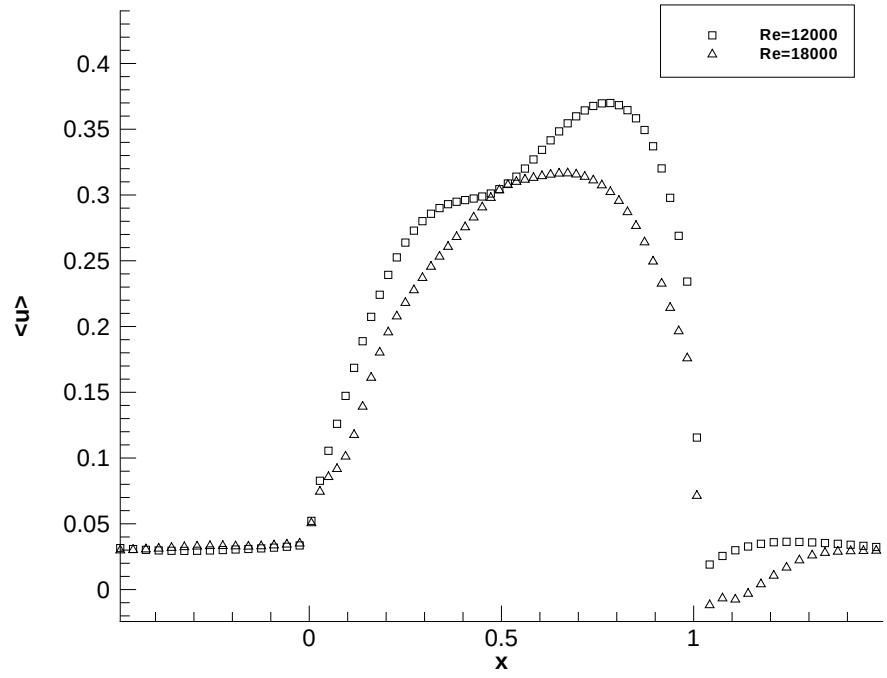

(a) Ensemble $< u >$ component of velocity.

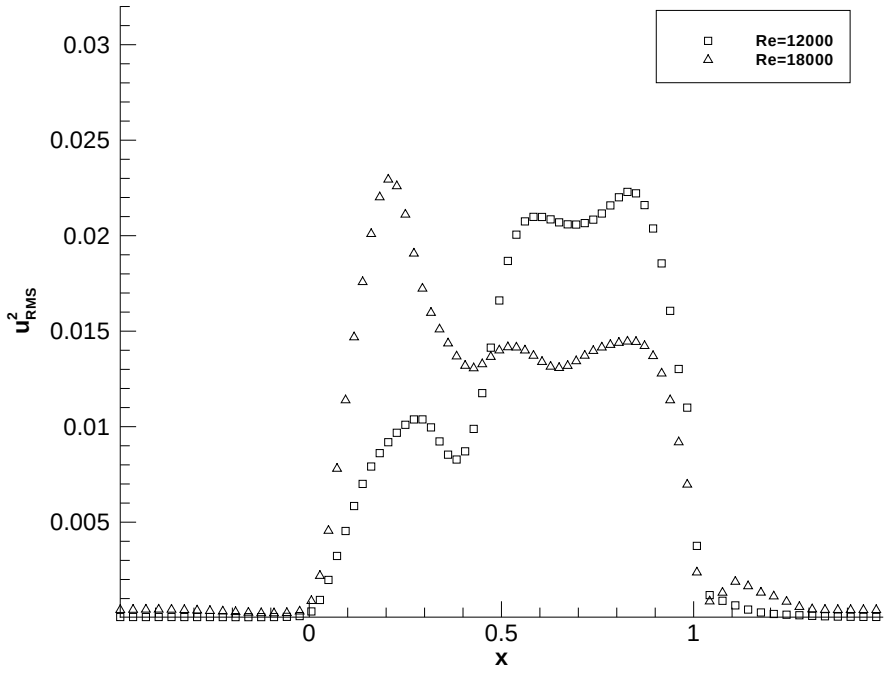

(b) u^2_{RMS} component of velocity.

Figure 5.35: Comparison of Reynolds number effect on mean and fluctuating velocity components along Line X1 on medium grids with third order reconstruction.

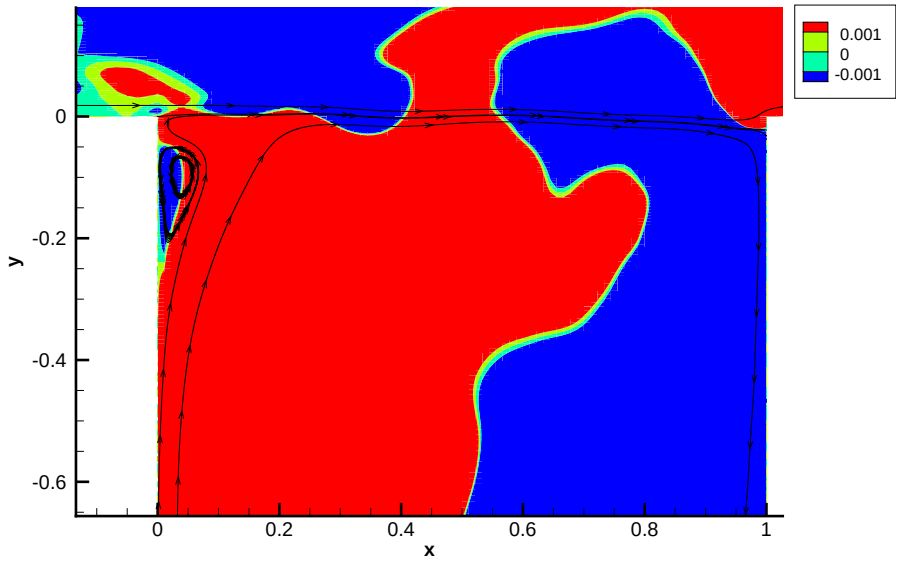

Figure 5.36: Vertical velocity at the top of the cavity with third order reconstruction on medium grid for Re=12000.

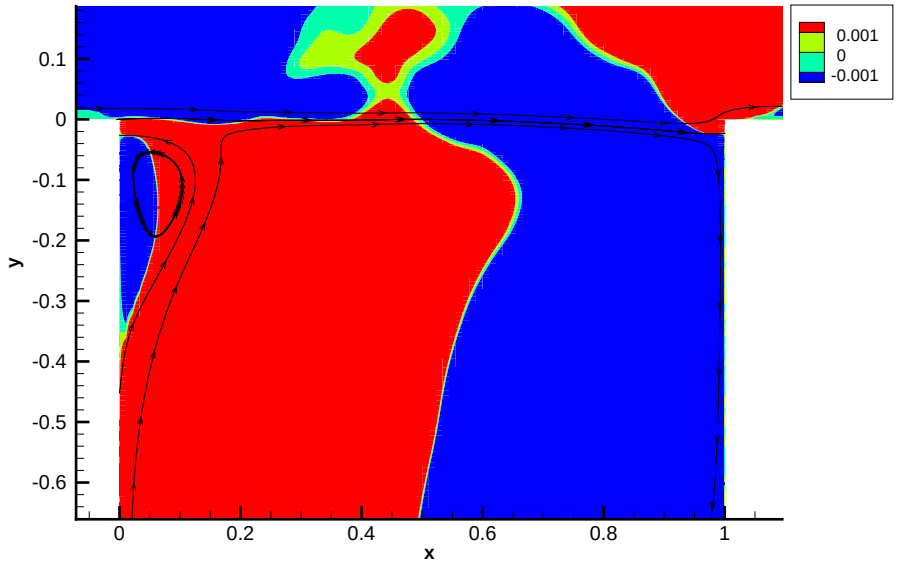

Figure 5.37: Vertical velocity at the top of the cavity with third order reconstruction on medium grid for Re=18000.

Heat Transfer

In order to understand the link between the heat transfer and the flow phenomena, the transient temperature field development has been computed. This can be achieved via two possible means. Firstly the energy increase per unit length can be specified with a forcing mechanism analogous to that of the pressure forcing described in Section 2. This would correspond to the fully developed flow and fully developed temperature field scenario. However, we can note that in order to understand the link between the flow field and heat transfer it is sufficient to compute the initial stages of the temperature field development only. In this approach no forcing term for temperature is used, instead we instantaneously activate the temperature boundary condition at the lower boundary when the flow is developed and compute the evolution of the thermal boundary layer. Understandably this creates a heat flux from the boundary proportional to $1/\Delta y$ at the first time step after the temperature (boundary condition) has been activated. So for the analysis it would be consistent to normalise the total heat flux by the heat flux at the first time step performed with the temperature active.

Therefore, the value plotted for the heat flux distribution in this section corresponds to:

$$Q_i = \frac{\left(\frac{\partial T}{\partial n}\left(t\right)\right)_i \Delta S_i}{\int_S \frac{\partial T}{\partial n}\left(t=0\right) dS} \tag{5.9}$$

Where i is the index of the surface element, ΔS_i is the surface area of this element, n is the direction normal to the wall and S is the solid surface encompassing cavity base, cavity left and right walls and fins. The derivative is approximated numerically using a second order accurate finite difference formula. For this approximation to be applicable, the thermal boundary layer has to be resolved. The integral heat flux as a function of time is then computed as:

$$Q\left(t\right) = \frac{\int_S \frac{\partial T}{\partial n}\left(t\right) dS}{\int_S \frac{\partial T}{\partial n}\left(t=0\right) dS} \tag{5.10}$$

Over the same surface. The times for which the computations were performed with temperature boundary condition are summarised in Table 5.5.

Medium Single Cavity, Re 12000	1st Order	3rd Order
Sample	10	1
Medium Single Cavity, Re 18000	1st Order	3rd Order
Sample	N/A	36.8

Table 5.5: Non-dimensional computational time durations for single cavity cases with heat transfer.

Indicative qualitative information can be extracted from the distribution of heat flux towards the end of the computational run time. Figure [5.38] shows the distribution of the normalised heat flux for first and third order reconstructions in space over the surface of the cavity and fins at Re=12000. Note that the gaps indicate positions of the computational blocks (values were output separately from the parallel processes, heat flux was computed only in cell centres, hence the gap of 1 cell size between neighbouring blocks).

The turbulent nature of the solution in the three dimensional case is evident with three dimensional effects more obvious on the downstream fin close to the shear layer impingement zone. The maximum local heat flux occurs on the downstream fin in both cases. High heat transfer rates also occurs at the cavity base. However, in terms of the surface area the cavity base is a lesser area than the side walls, hence the integral heat flux from the cavity base can be smaller than that from the side walls.

At the end of the computations the thermal boundary layer started to develop and in the cavity there is an entrainment of the hot fluid from the near wall region at the boundary between the counter rotating vortices.

The total heat flux for each of the cases is presented in Figure [5.39]. It is clear to see that the third order medium Re=18000 case demonstrates an unsteadiness which is

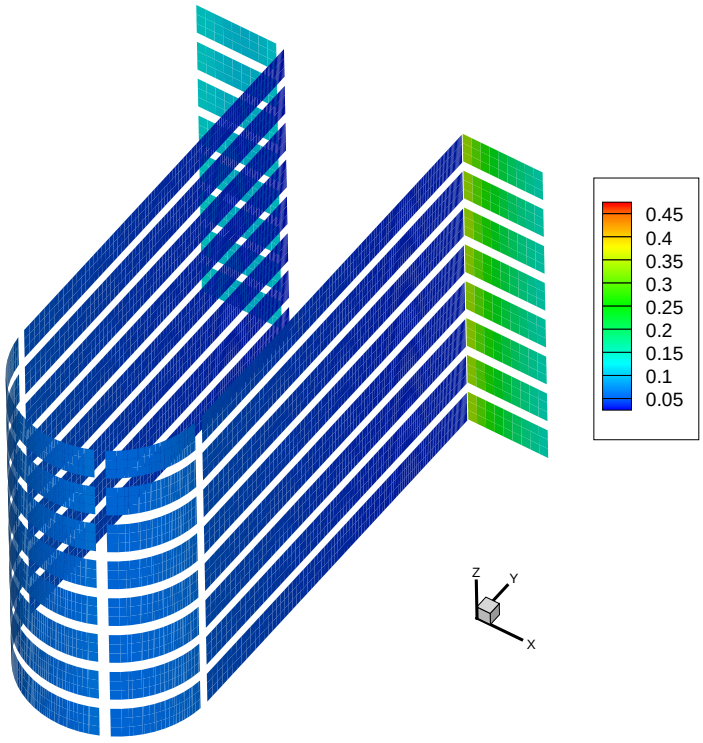

(a) First order reconstruction.

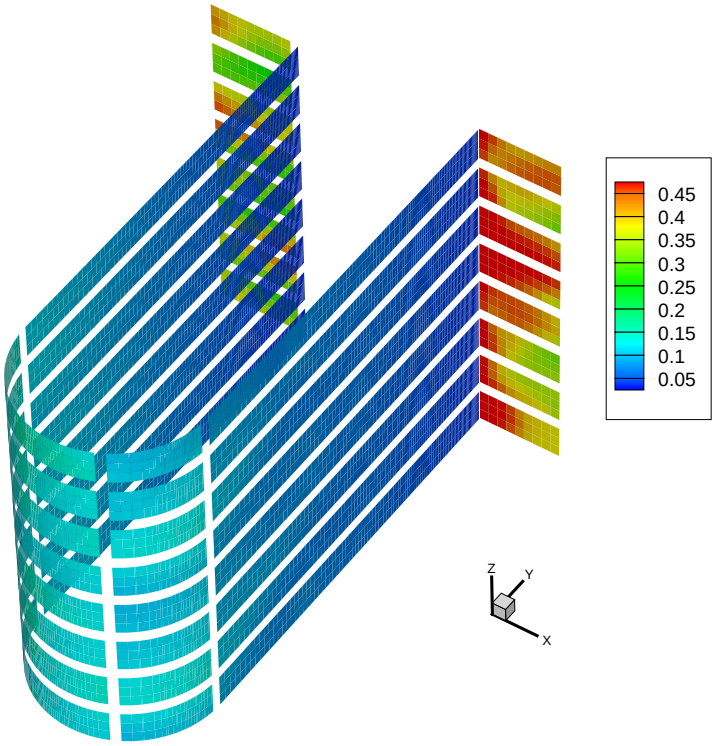

(b) Third order reconstruction.

Figure 5.38: Heat flux distribution at the end of computations for Re=12000 on the coarse grid.

not apparent in the Re=12000 first order case. This is due to the flow experiencing excessive dissipation due to the numerical scheme.

Since the run time for the Re=12000 (temperature sampling) was significantly shorter than the rest of the cases shown here it is possible that the total heat flux may have developed a similar level of unsteadiness seen in the Re=18000 case.

The heat flux was decomposed into separate regions corresponding to the entire cavity, left and right cavity walls, cavity base and fin walls (up and downstream of the cavity mouth). The magnitude and relative comparison to the total heat flux is shown here and one may notice that the cavity is responsible for the majority of the heat transfer in the geometry.

The unsteadiness exhibited by the total heat flux is due to the impact of the finned surface. Here it is suspected that the heat flux varies due to the periodic occurence of the vortex shedding that occurs downstream from the cavity mouth.

The left and right walls in the cavity provide similar levels of heat transfer in comparison, see Figure [5.40]. The surface that provides the minimum of heat transfer is the cavity base. This is contrary to the intended design of the geometry, however this is due to the lack of modelling of nucleate boiling which is suspected to occur at the base of the cavity. The result of such phenomena would provide thermobuoyancy and further enhance vortex shedding within the flow field.

The Figure [5.41] shows only the decomposed heat flux contributions from the cavity walls in comparison with the fins in the domain. The data shows that only a small contribution occurs from the fins however it is highly unsteady in its nature.

The left and right walls also seem to demonstrate an unsteadiness although the magnitude and frequency of the fluctuations are significantly lower in comparison with the fins, see Figures [5.41] and [5.42].

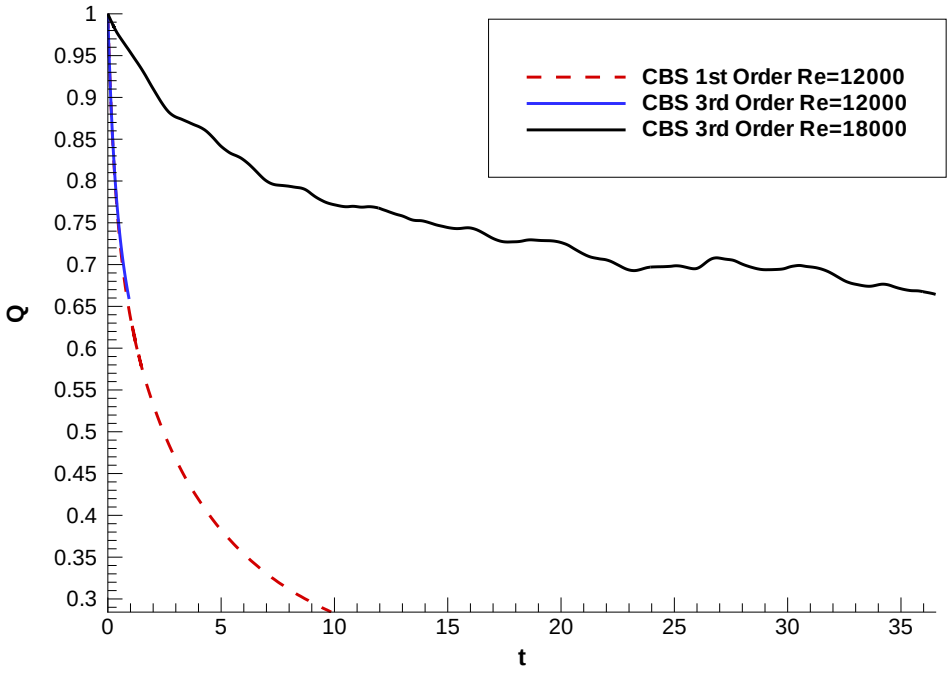

Figure 5.39: Total heat flux for all single cavity cases on medium grids.

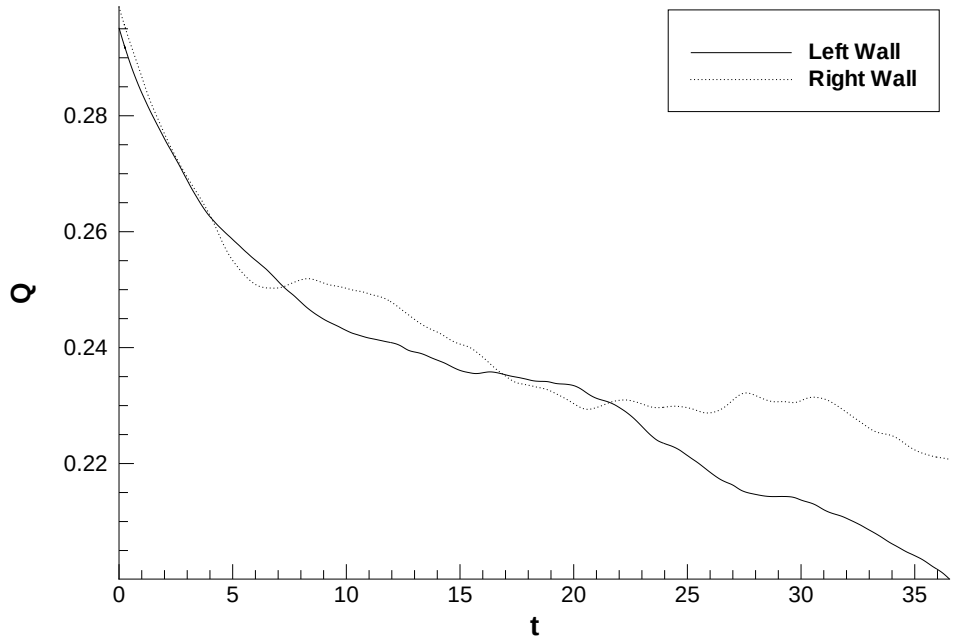

Figure 5.40: Single cavity left and right walls heat flux contribution for Re=18000 on the medium grid with third order variable reconstruction.

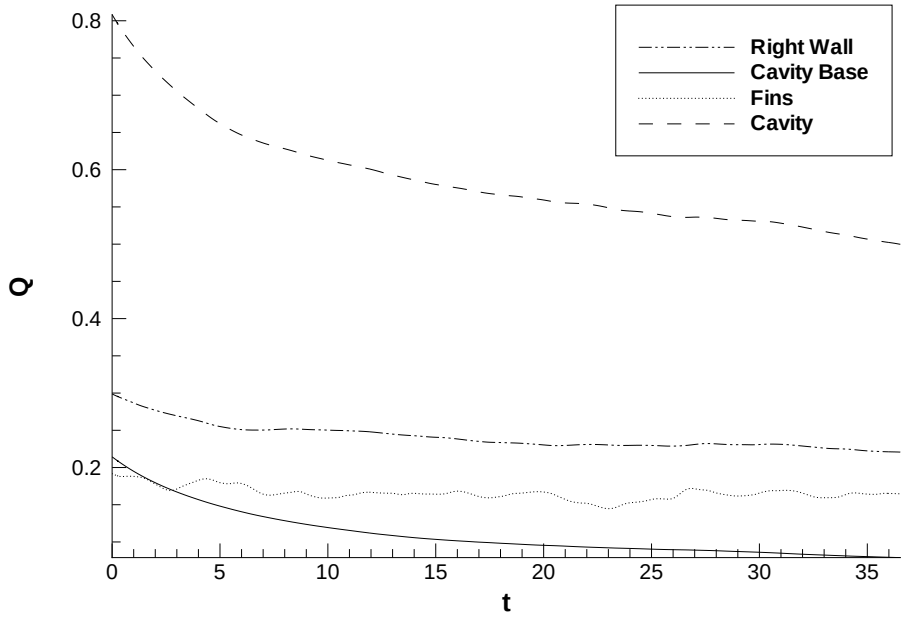

Figure 5.41: Single cavity left and right walls, cavities and fins heat flux contributions comparison for Re=18000 on the medium grid with third order variable reconstruction.

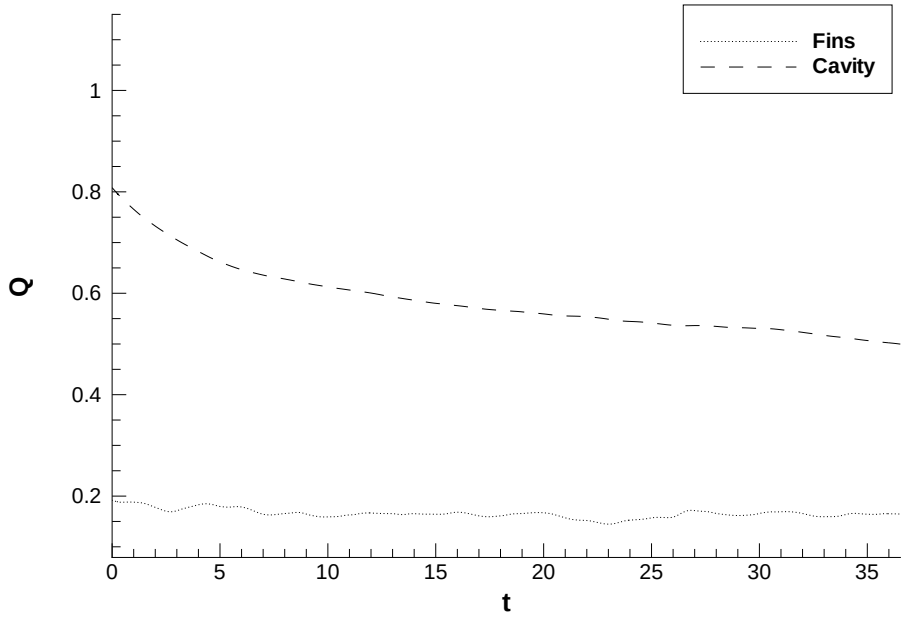

Figure 5.42: Single cavity fins and cavity walls heat flux contributions comparison for Re=18000 on the medium grid with third order variable reconstruction.

5.6.2 Three Cavity Array

The origin of the domain is at the upper left corner of the first cavity. The reporting lines for the ensemble properties are defined below by coordinates that locate the line passing through the spanwise centre symmetry plane, as in the single cavity case. The results presented are based on the shear layer, upstream, downstream, cavity and channel profiles. This structure is repeated in the streamwise direction over the additional cavities. The definition of all the reporting lines presented is detailed below:

- X-Lines
    1. Line X1: Y=0.0001, Z=1.
- Y-Lines
    1. Line Y1: X=-0.25, Z=1.
    2. Line Y2: X=0.5, Z=1.
    3. Line Y3: X=1.25, Z=1.
    4. Line Y4: X=1.75, Z=1.
    5. Line Y5: X=2.5, Z=1.
    6. Line Y6: X=3.25, Z=1.
    7. Line Y7: X=3.75, Z=1.
    8. Line Y8: X=4.5, Z=1.
    9. Line Y9: X=5.25, Z=1.

The analysis of the three cavity array with heat transfer focuses on the coarse grid only for Re=12000. For this case the sampling interval corresponded to the non-dimensional time of 10.

The markers in the shear layer and the mass flux in the sampling interval are shown in Figure [5.44]. The results are similar to the single cavity cases however one may notice the run time is relatively short.

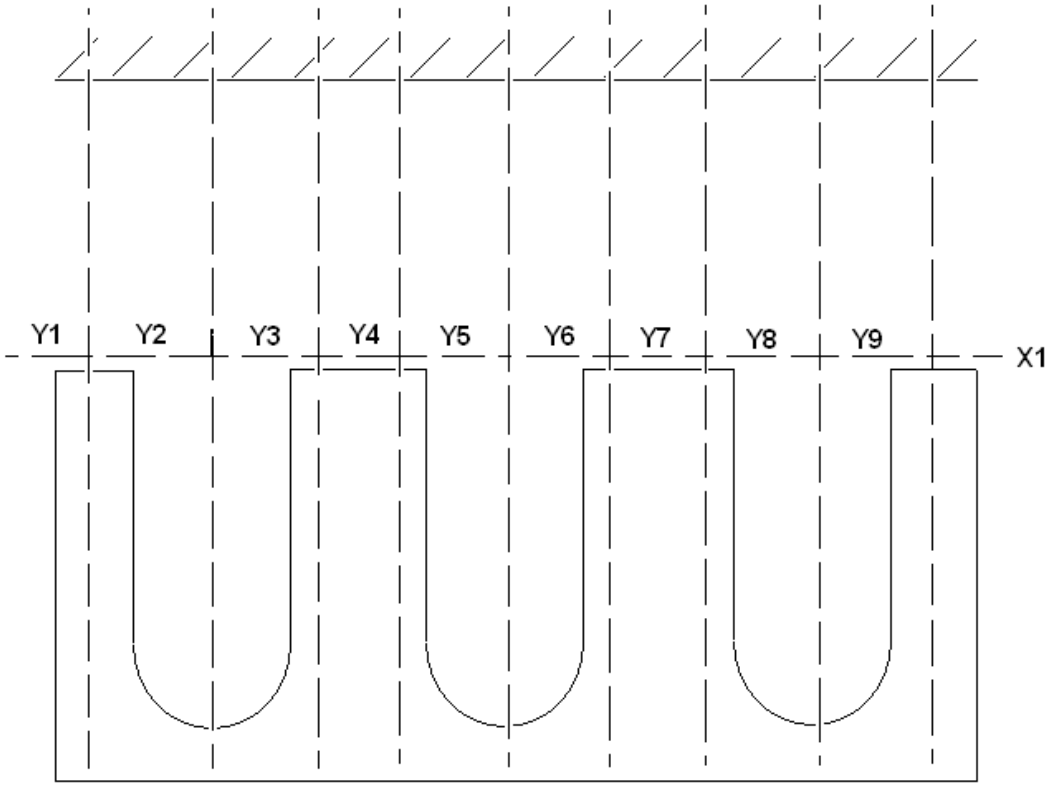

Figure 5.43: Schematic for reporting lines locations in three cavity array cases.

The adequacy of the time window was established by comparisons of the average velocity on Line Y2 at the end of the sampling window and 100 time steps before that point. Figure [5.45] shows the streamwise velocity profiles, the data shows that the flow averages have established sufficently.

Another question to be addressed is whether the additional two repeating units in the streamwise direction affect the periodicity of the solution. To illustrate that a single repeating unit is sufficient, but bearing in mind the flow data on the lines symmetrically offset from the cavity corners and should not necessarily be the same.

Let us group the Y Lines as follows:

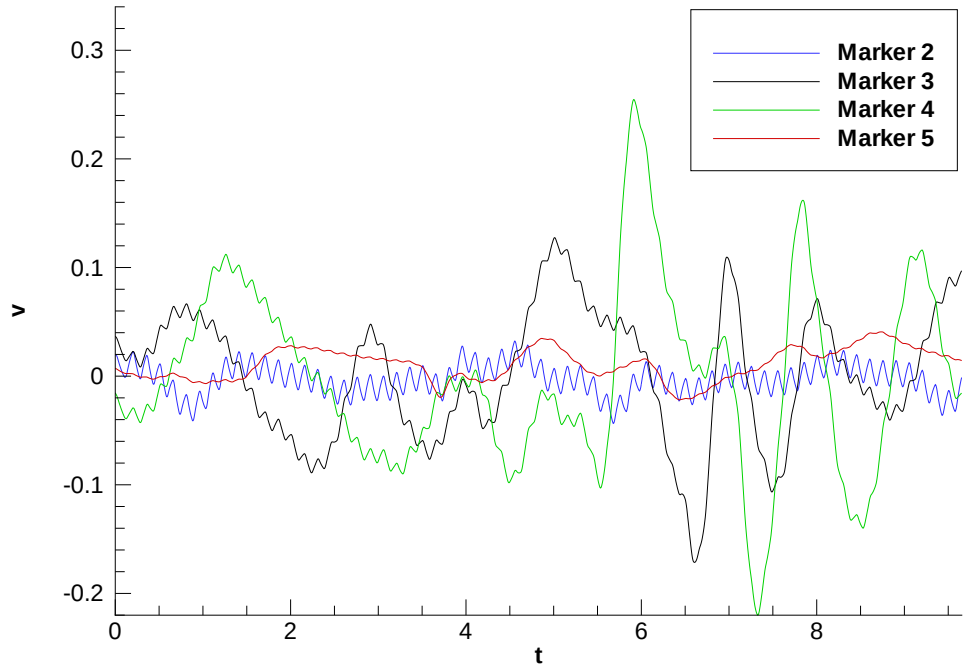

(a) Marker in the shear layer

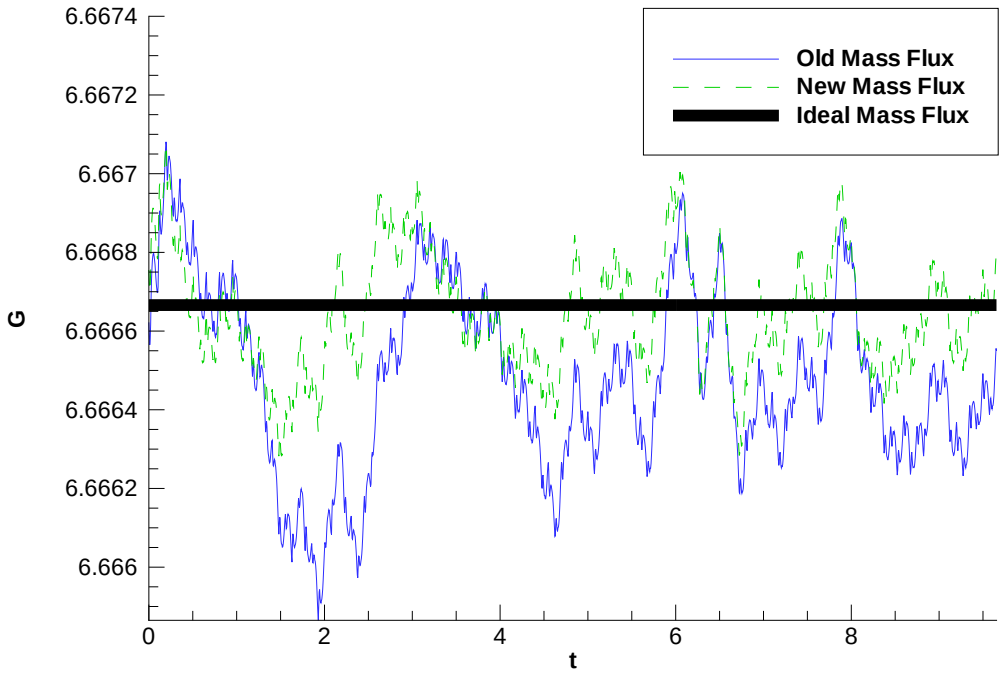

(b) Mass flux.

Figure 5.44: Flow markers and mass flux in the sampling window for Re=12000 with third order reconstruction on the coarse grid.

- 1st group: Lines Y1,Y4,Y7 - these are located upstream of each cavity separated by a distance of -0.25 from the upstream cavity corner.
- 2nd group: Lines Y3,Y6,Y9 - these are located downstream of each cavity separated by a distance of +0.25 from the downstream cavity corner.
- 3rd group: Lines Y2,Y5,Y8 - these are located in the middle of each cavity and also pass through the channel.

Figure [5.46] shows the time-space averaged flow in a single cavity of the three cavity array. The topology is the same as for a single cavity with some differences observed due to the coarser grid employed in the three cavity array to be able to include the solid.

Figure [5.47]-[5.49] presents the results for $< u >$, u^2_{RMS} and v^2_{RMS} on the first and second group of lines.

It is clear that while within each group the results are almost identical, there is a slight difference between the groups which is more pronounced on the Reynolds stresses plots. The same effect was observed for the single cavity computations. It is therefore sufficient to consider only one repeating unit in the analysis, however, we should bear in mind that the repeating unit does not have the symmetry between the upstream and downstream plate.

The corresponding solution for the distribution of flow and turbulent properties in the cavity is given in Figures [5.50] and [5.51].

Analysis based on the variation for the number of repeating units has shown that significant differences are not observed in the averaged quantities and the comparison of the stresses suggests that any difference is well within the order of the simulation accuracy.

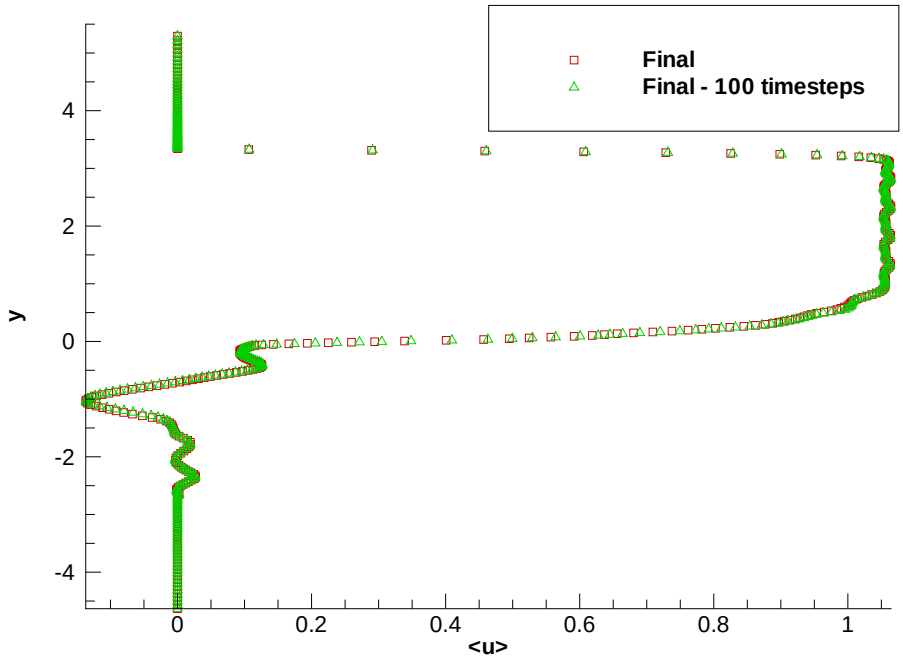

Figure 5.45: Convergence of flow statistics for three cavity array case with Re=12000 and third order reconstruction on the coarse grid.

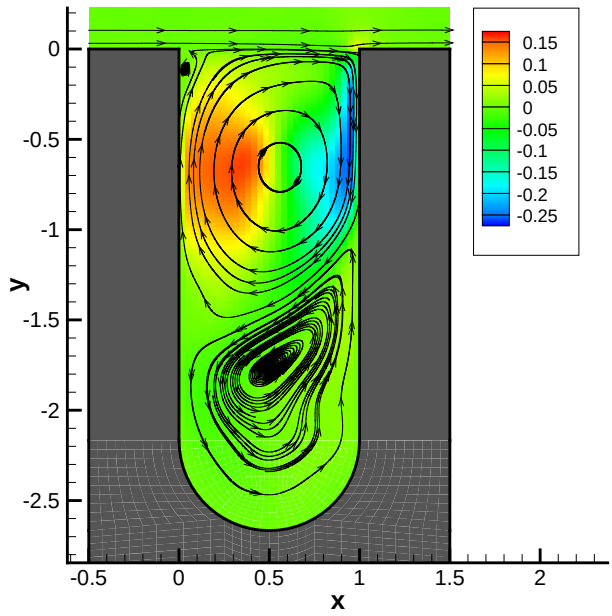

Figure 5.46: Streamlines and velocity contours for time-space averaged flow a single cavity in the three cavity array for Re=12000 with third order reconstruction on a coarse grid.

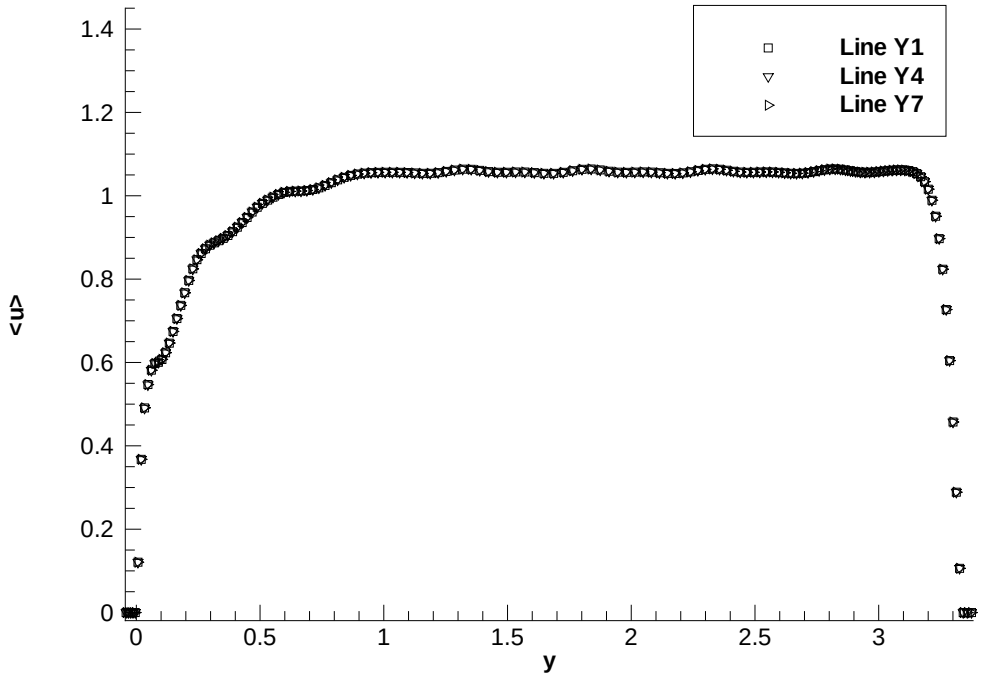

(a) 1st group.

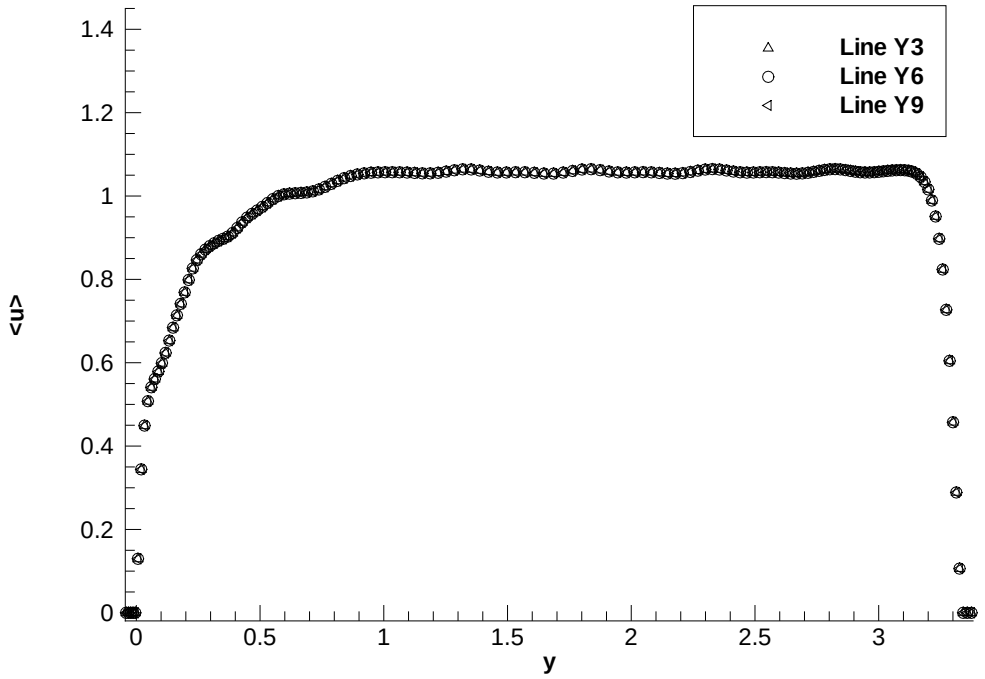

(b) 2nd group.

Figure 5.47: Ensemble component of $< u >$ velocity for the 1st and 2nd group of Y Lines in three cavity simulations for Re=12000 with third order reconstruction on the coarse grid.

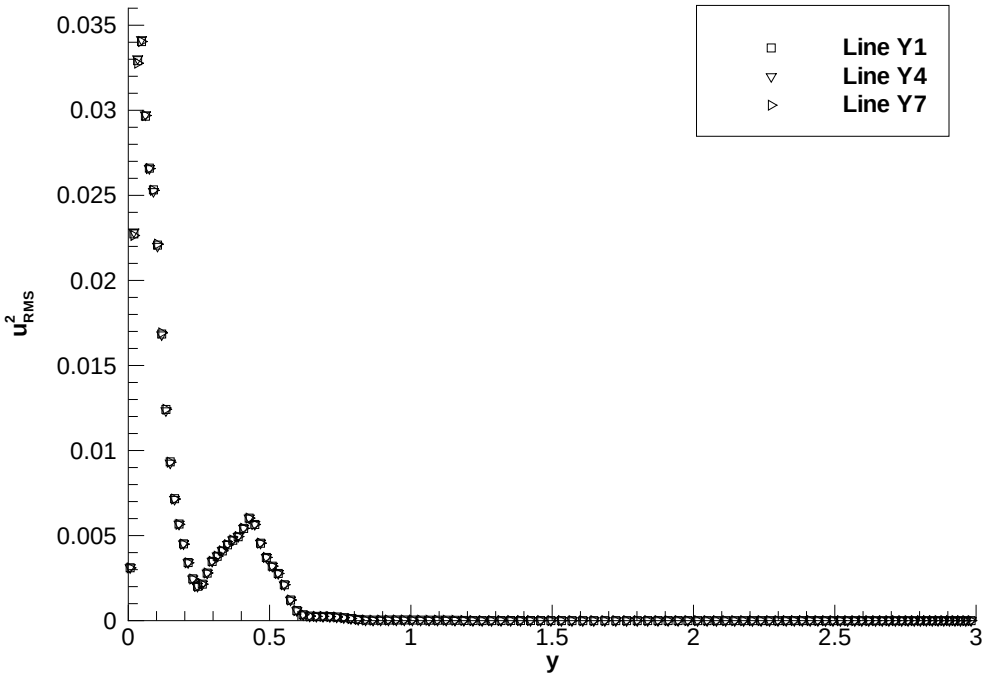

(a) 1st group.

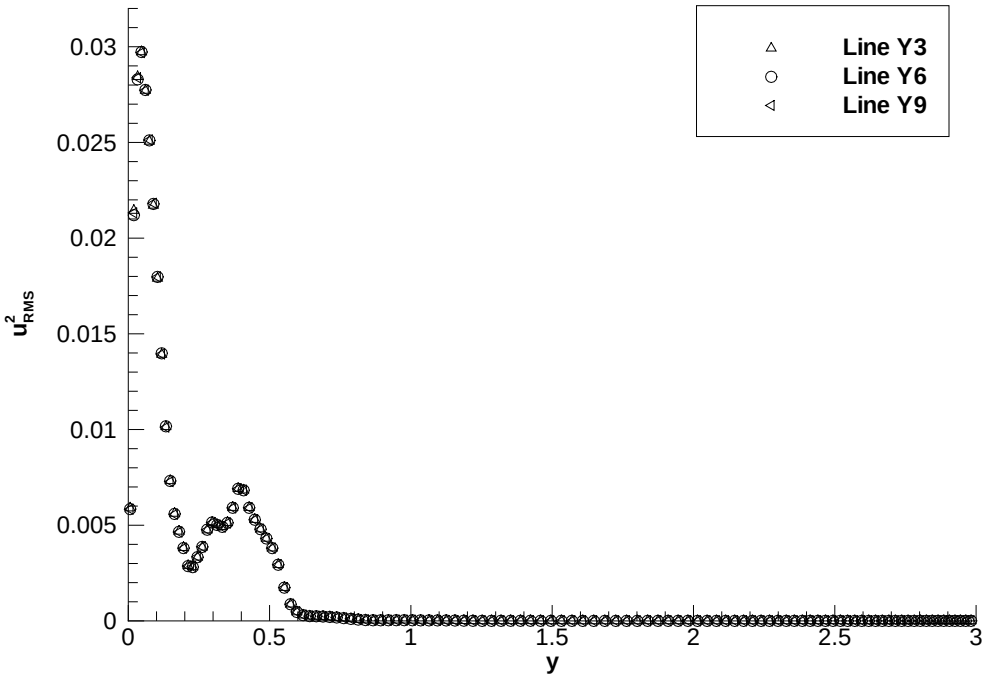

(b) 2nd group.

Figure 5.48: u^2_{RMS} components of velocity for 1st and 2nd group of Y Lines in three cavity simulations for Re=12000 with third order reconstruction on the coarse grid.

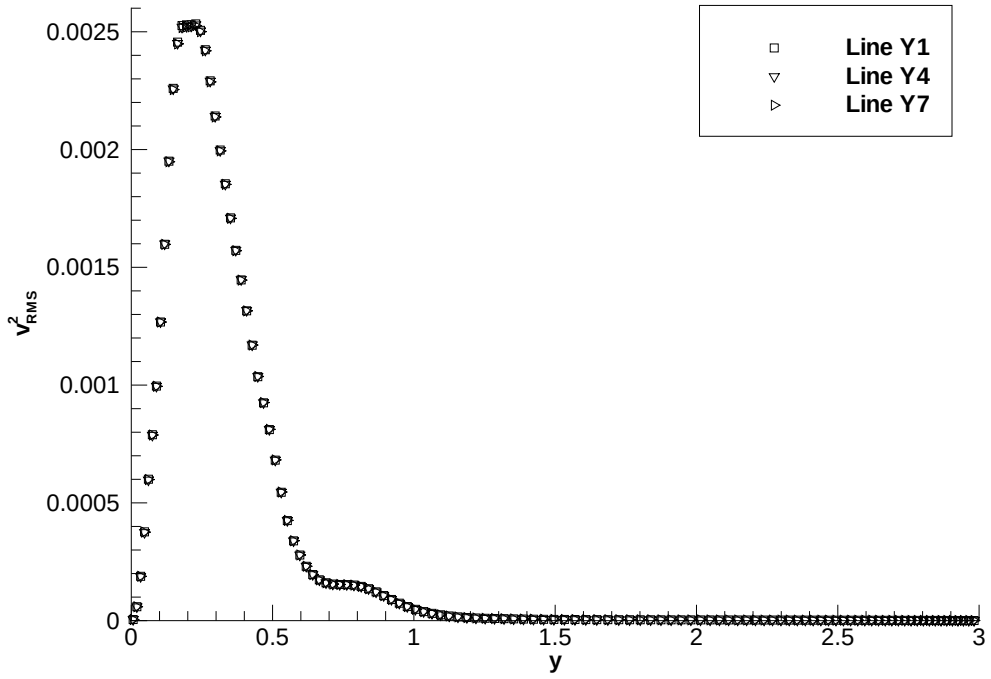

(a) 1st group.

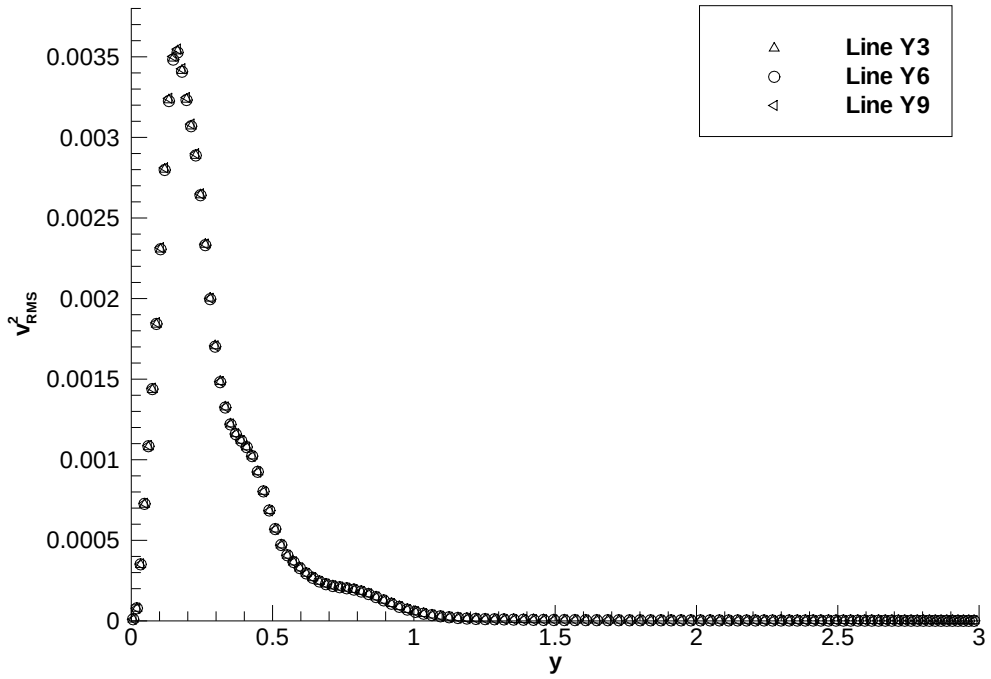

(b) 2nd group.

Figure 5.49: v^2_{RMS} components of velocity for 1st and 2nd group of Y Lines in three cavity simulations for Re=12000 with third order reconstruction on the coarse grid.

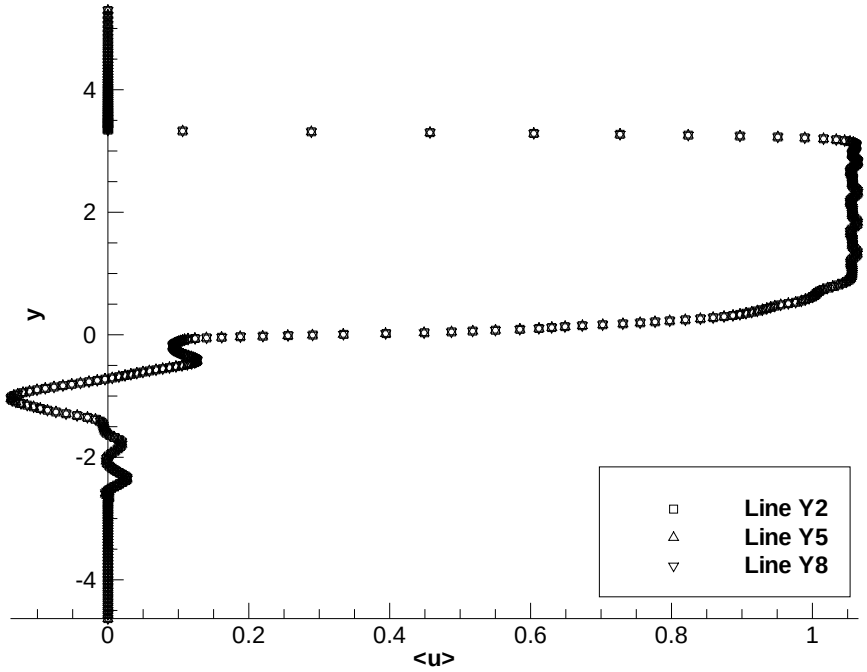

(a) Ensemble $< u >$ component on the Y2 Line in the cavities.

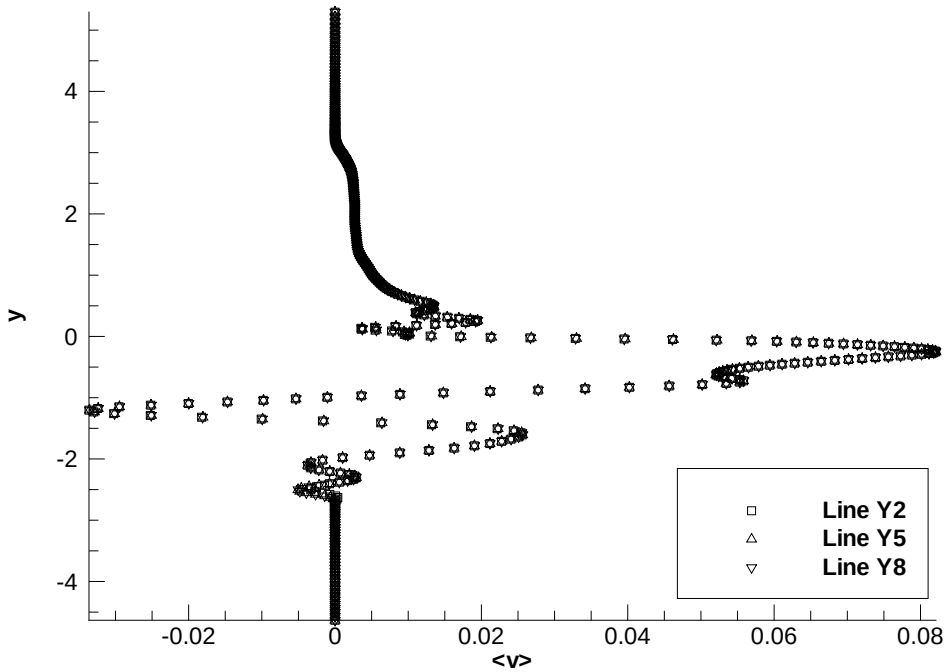

(b) Ensemble $< v >$ component on the Y2 Line in the cavities.

Figure 5.50: Ensemble components of velocity for 3rd group of Y Lines in three cavity simulations for Re=12000 with third order reconstruction on the coarse grid.

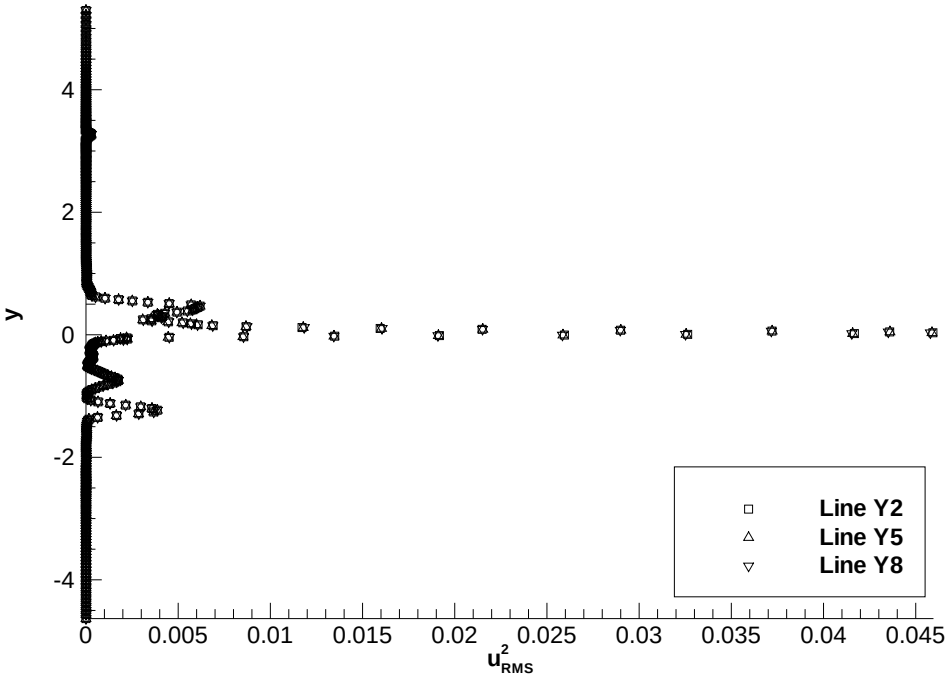

(a) u^2_{RMS} component on the Y2 Line in the cavities.

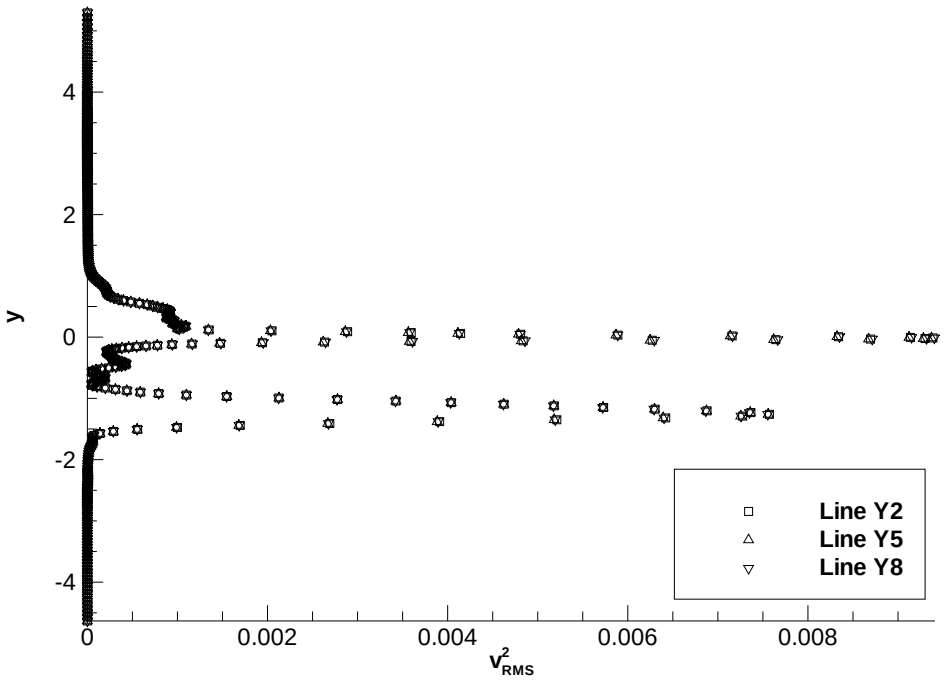

(b) v^2_{RMS} component on the Y2 Line in the cavities.

Figure 5.51: Fluctuating components of velocity for 3rd group of Y Lines in three cavity simulations for Re=12000 with third order reconstruction on the coarse grid.

Heat Transfer

After the flow field solution was established, the temperature in solid was initialised to 1 and 0 in the fluid. The transient heat transfer problem was computed for a further 20 non-dimensional time units. The data here is presented only for the first cavity as the results for the rest of the cavities are the same.

Figures [5.52] and [5.53] illustrates the development of the temperature in the solid and cavity over that interval using temperature contours averaged over z-direction.

The scales of the local fluid temperature and global temperature are well separated and the Figure [5.52] presents the global temperature scale relevant most to the solid region and the Figure [5.53] shows the local fluid temperature contours within the cavity and channel region.

Initially, the thermal boundary layer develops uniformly across the solid-fluid interface with hot entrainment occuring at the upstream cavity corner (see Figures [5.52a] and [5.53a]). The solution continues with the fins being cooled faster from the top rather than from the sides in line with the heat flux distribution highlighted for the single cavity cases. At the same time the hot boundary layer from the upstream plate is convected across the top of the cavity and entrainment of the hot fluid from the downstream wall of the cavity occurs due to the counter rotating vortex motion (see Figures [5.52b], [5.53b], [5.52c] and [5.53c]).

By the end of the run at t=20, the fluid in the cavity starts to heat up with the temperature contours being influenced by vortex boundaries. However, the hot spot at the bottom of the cavity remains, see Figures [5.52d] and [5.53d].

These results show clearly the development of the solid-fluid interface boundary solution which is heavily influenced by the local flow field surrounding the lower interior wall.

The distribution of temperature on reporting lines at the end of the run is shown in Figure [5.54]. The lines show the instantaneous temperature T along lines Y1-Y3. The developing thermal boundary layer may be observed in Lines Y1 and Y3 (Figure [5.54a]). The Line Y2 (see Figure [5.54b],) shows the two local maxima corresponding to the cavity top and the contact line between counter rotating vortices.

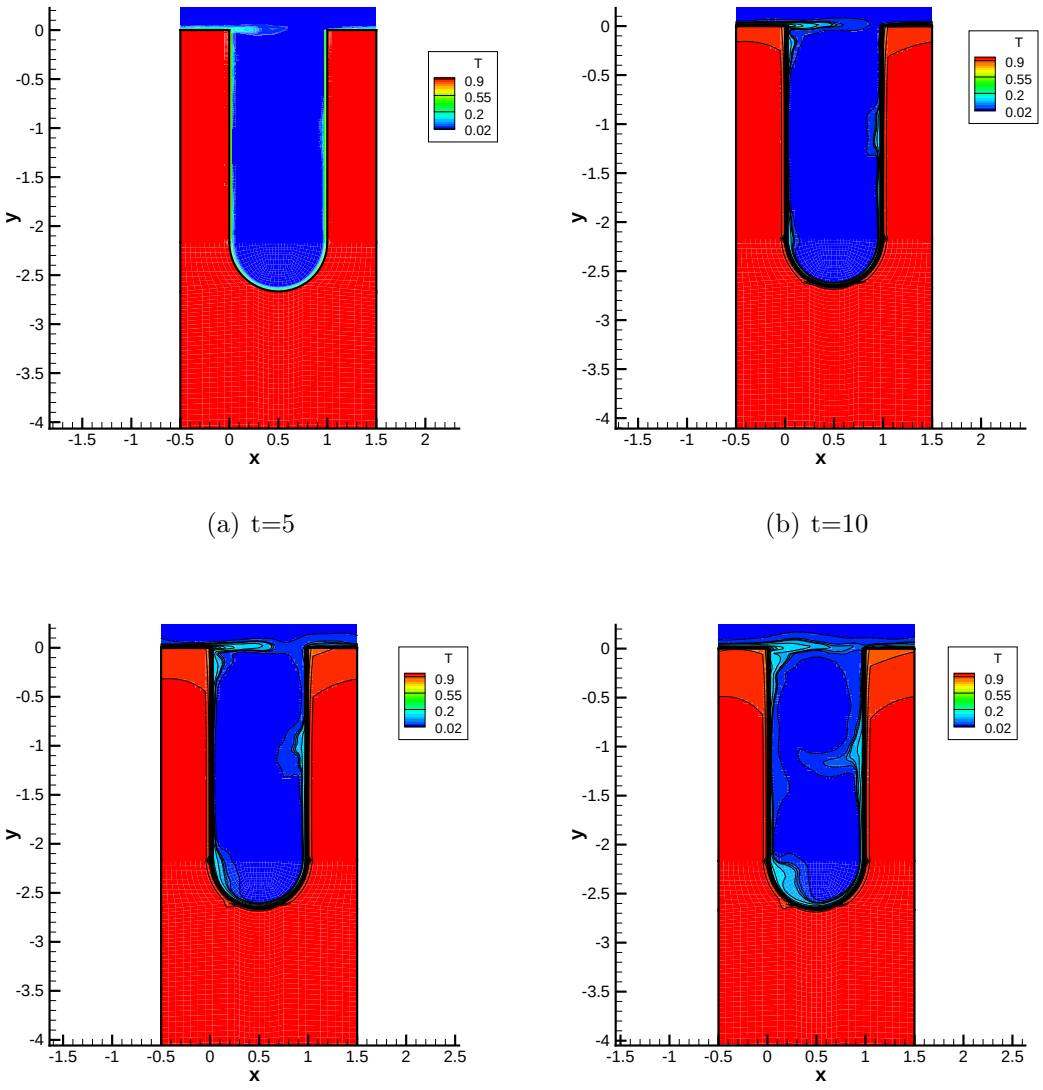

(a) t=5

(b) t=10

(c) t=15

(d) t=20

Figure 5.52: Temperature field development within solid time for Re=12000 with third order reconstruction on the coarse grid.

The local maximum at the top of the cavity is due to the hot shear layer developing from the heated boundary layer on the upstream plate. The local maximum in the middle of the cavity is due to the entrainment of the hot fluid from the right wall of the cavity by the counter rotating vortices. The heat flux comparisons, Figures [5.55] and [5.56], are similar to the single cavity case, Re=18000. However, the greater heat flux occurs on the left wall which may be considered non-intuitive.

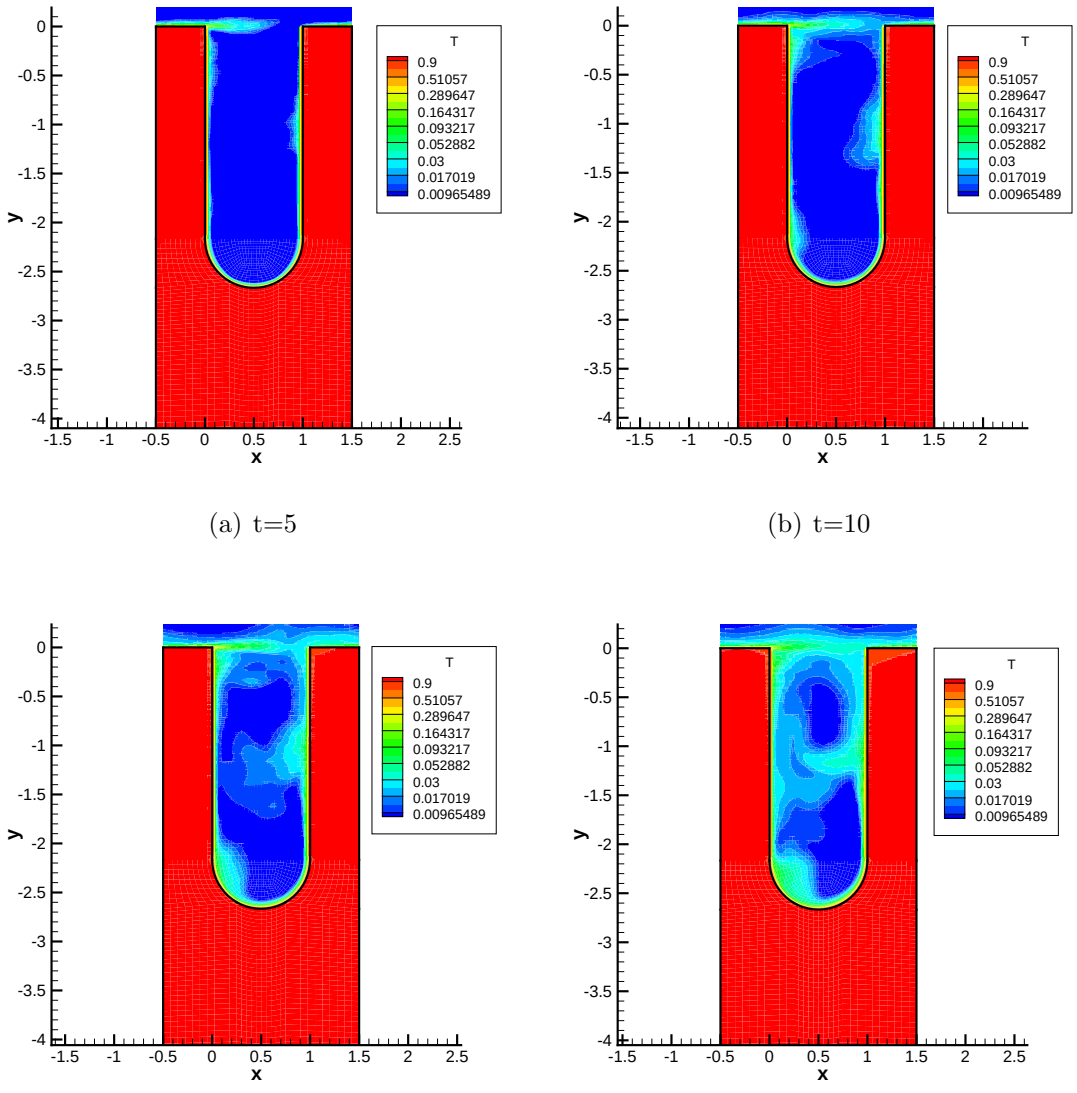

(a) t=5

(b) t=10

(c) t=15

(d) t=20

Figure 5.53: Temperature field development within fluid for Re=12000 with third order reconstruction on the coarse grid.

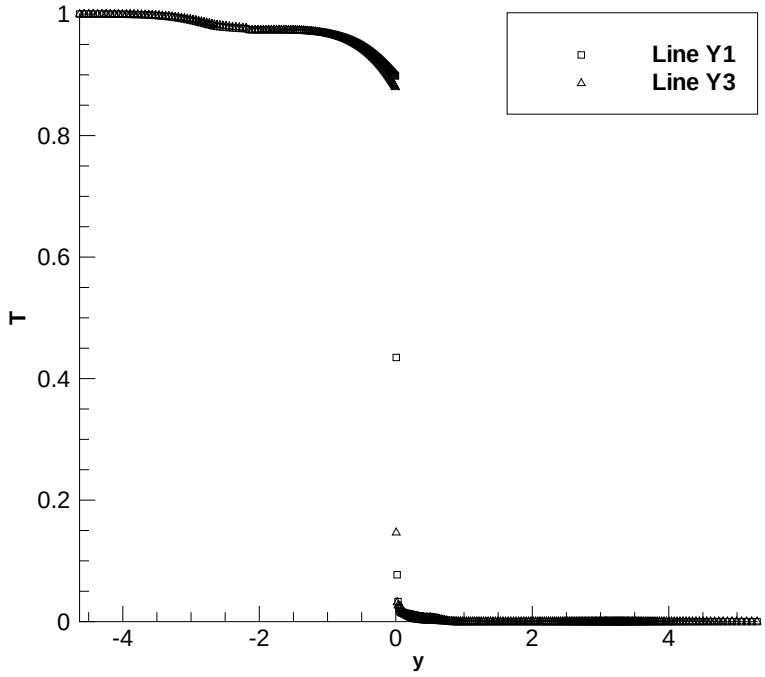

(a) Lines Y1 and Y3.

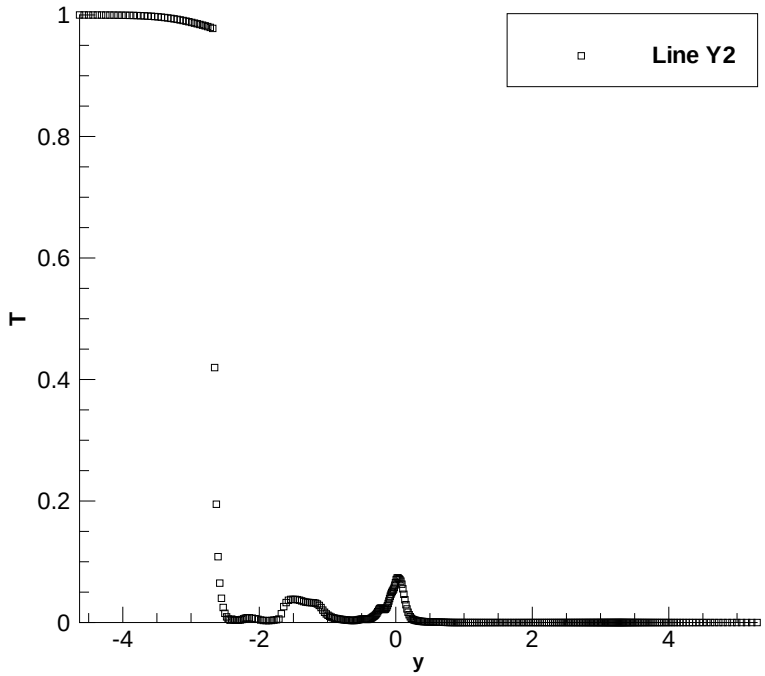

(b) Line Y2.

Figure 5.54: Temperature distribution at the end of the run with temperature for Re=12000 with third order reconstruction on the coarse grid.

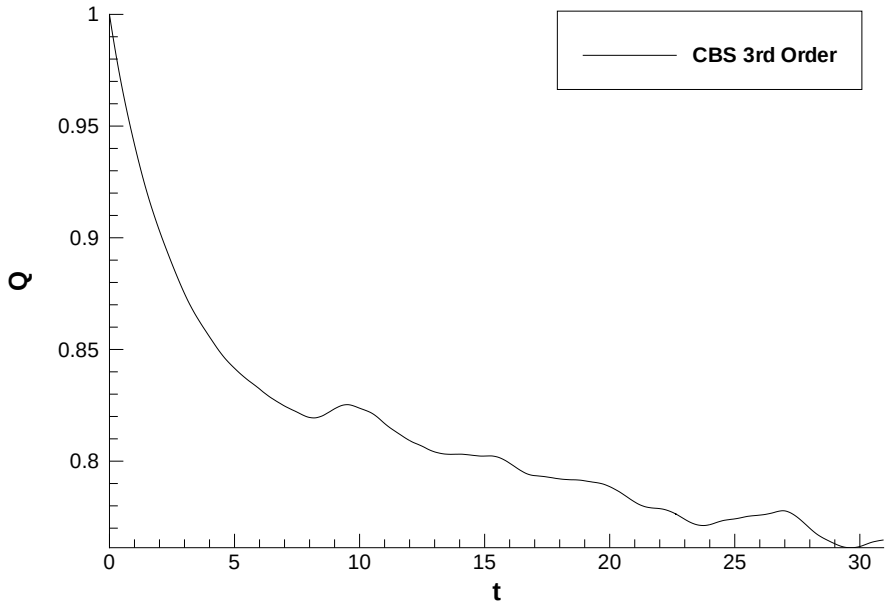

Figure 5.55: Three cavity array total heat flux for Re=12000 on the coarse grid with third order reconstruction.

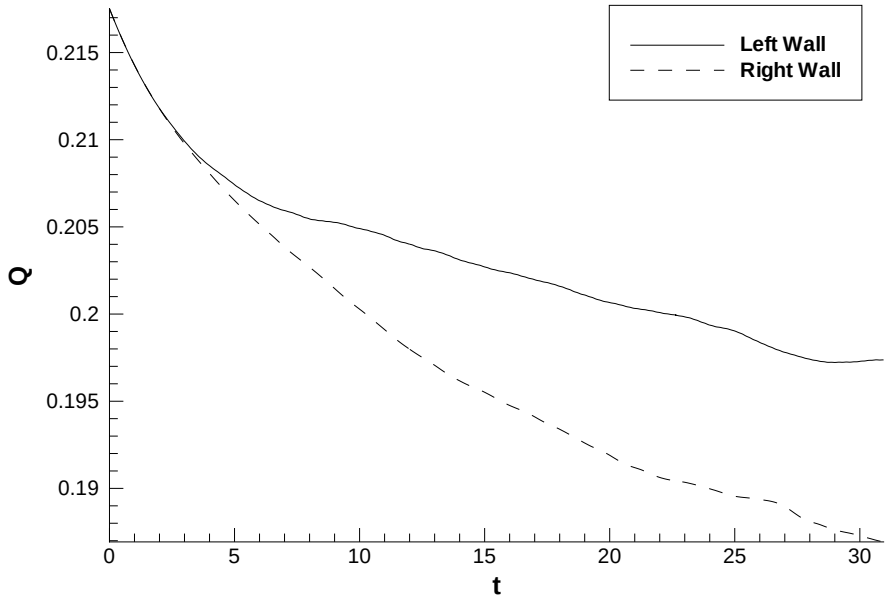

Figure 5.56: Three cavity array left and right walls heat flux contribution for Re=12000 on the coarse grid with third order reconstruction.

Chapter 6

Conclusions and Future Aspirations

Initially the focus of this PhD was to recover the flow structure for the Hypervapotrons and to provide specific design guidelines for improved performance. The performance of the device is measured by its ability to dissipate heat.

Since limited experimental and numerical studies of the Hypervapotrons exist a validation strategy was developed during the course of the PhD.

Attempts were made to decouple key features of the phenomena expected to exist within the Hypervapotron main section. Therefore, different cavity and channel flow cases were considered to develop a rigorous validation of the numerical formulations used.

The lid driven case was the cornerstone of this exercise. The case introduced several flow features seen between the fins in the Hypervapotron main section. This investigation considered the suitability of ILES in wall bounded flow throughout this study.

Currently this is a common area where almost all numerical approaches struggle. In particular (explicit) LES is famously prone to this, therefore, impact on accuracy for variants of high-resolution (more specifically high-order) schemes in the ILES framework has been conducted.

The flow validation of the three dimensional lid driven cavity has been simulated with accuracy here on relatively coarse grids. As expected the grid resolution has great impact on the quality of results obtained from the simulations. It has been noted that the most efficient grid is the 64^3 with third order reconstruction.

From achieving such a close comparison using the lid driven case, confidence has been established on employing similar grid resolutions for the simulation of the Hypervapotrons, on both single and three cavity arrangements.

It is suggested that the periodic case serves to illustrate the optimal design. This assumption requires that the spanwise dimension is sufficient to induce a large primary two dimensional element to the flow. The implications of this assumption when approximately 250 Standard (design) units (exist in a network) suggests this approach, when used to optimise the design, provides a significant contribution to the overall heat transfer coefficient of the ion dumps.

However, this approach may only be suitable for subtle design changes such as finned surface dimensions, cavity aspect ratios, channel heights and material options.

The computational model (for the Hypervapotrons,) presented here, neglects the effect of end walls on the problem. It was desired to model the end walls; however the computational requirements would case result in a very large computing resource which was unavailable to the author.

The topology of the flow resulting from different reconstruction schemes for the Hypervapotron cases, is provided within the analysis, and the impact of grid resolution is also discussed. The impact of grid density has been investigated and it

has been noted that the increase required in grid resolution results in an excessive computational requirement.

The difference in flow structure topology is noted as the first order solutions lead to a single recirculation zone in the cavity. However, the third order case results in two separate counter rotating vortices.

Analysis based on the variation for the number of repeating units has shown that significant differences are not observed in the averaged quantities and the comparison of the stresses suggests that any difference is well within the order of the simulation accuracy.

The viscous boundary layer is developed in all cases and flow structure is shown for both Re=12000 and Re=18000 modelled on medium grids. It is suggested that the attributes of the key flow structure have been established and the findings presented here provide a significant advancement in the understanding of the flow structure topology.

Important findings of the heat transfer were found by employing an additional scalar for temperature since this was deemed a tractable method of obtaining the location and development of hot spots, which correspond to the regions where incipient boiling would initially occur.

In all cases with heat transfer the development of the thermal boundary layer is observed but further computational time is required in order to see an established thermal boundary layer (in addition to temperature forcing). Such studies would only provide accurate data at sub boiling temperatures when voidage at the wall surface is negligible.

Since the impact of boiling is not incorporated into the model, the current formulation relies on any gaseous phase present, to be a small percentage of the working fluid. However, in reality the thermobuoyancy produced by nucleation sites (within

the cavity) is thought to be responsible for enhanced vortex shedding out of the cavity mouth and may promote enhanced heat transfer.

Therefore, it is proposed that future studies should include attempts to model the voidage occurring at the wall surface during the (entire) transient. Also, similar investigations may be used to compare the MAST geometry.

There are several other possibilities excluding geometry changes that may optimise the performance of the Hypervapotrons. In particular pressurised flow circuit may be useful in order to increase the heat flux capacity of the devices efficiently using such a method the boiling regime may be controlled and forced to be nucleate.

Further information regarding the turbulent flow structure may be obatined by considering the grid independent solutions.

In general the flow solutions presented within were solved using coarse grids that were far from the required grid resolutions necessary to obtain grid independace. This was due to the excessive computational requirement for the Hypervapotron cases. However, since the code is now parallel the possibility of obtaining the grid independent solutions is upon us.

Recently RANS results obtained on similar grids (for Re=18000) have become available courtesy of the UKAEA. The analysis of the heat transfer compares well with data provided by the UKAEA using RANS, (on similar grids) in conjunction with eddy viscosity based turbulence models.

The total normalised heat flux is shown in Figure [6.1]. The RANS results were obtained with ANSYS CFX using the standard $k-\epsilon$ model and SST $k-\omega$ models. The ILES simulation compares best with the SST $k-\omega$ data.

The results used in the comparison only recently became available and is preliminary, therefore it is also suggested that future work on this topic may be useful to draw

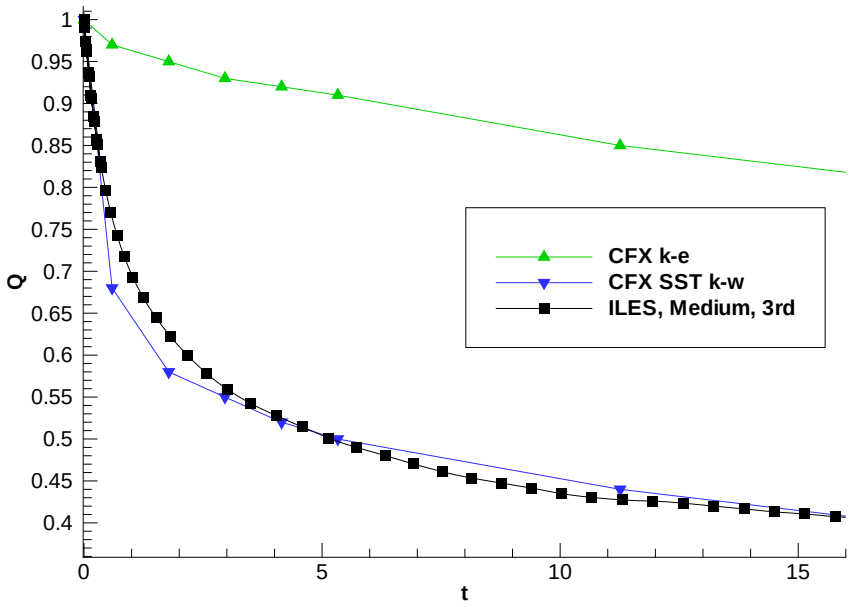

Figure 6.1: Total heat flux comparison of ILES and RANS.

comparison between the numerical tendencies and accuracy of ILES and RANS. In order to support the proposed analysis, it is also recommended that the lid driven case is considered for the RANS simulations, in conjuction with the experimental results of Prasad & Koseff (1989).

Finally, with regard to the entrance and exit regions of the Hypervapotrons, these may be used to provide a large increase in the cooling capacity of the heat flux devices. The shape of the entrance and exit regions is suspected to effect the heat transfer rates significantly since large regions of the flow field can be manipulated by these.

Due to the coupled nature of the flow and temperature fields, different heat transfer rates to that in the developed flow region will be present. Further, since a significant number of the features reside within NBH systems, one can suggest that the design of the entrance and exit geometries (which also provide bulk flow losses) becomes more important as the number of (Hypervapotron) devices is increased.

References

Acharya, S., Dutta, S., Myrum, T.A., & Baker, R.S. 1993. Periodically developed flow and heat transfer in a ribbed duct. *International Journal of Heat and Mass Transfer*, **36**, 2069–2082.

Baker, A.J. 1983. *Finite element computational fluid mechanics.* McGraw-Hill.

Barragy, E., & Carey, G.F. 1997. Stream function vorticity driven cavity solution using p finite elements. *Computers and Fluids*, **26**(5), 453–468.

Baxi, C.B. 2004. Comparison of swirl tube and hypervapotron for cooling of ITER divertor. *General Atomics Publication.*

Betts, P.L., & Bokhari, I.H. 2000. Experiments on turbulent natural convection in an enclosed tall cavity. *Internatinal Journal of Heat and Fluid Flow*, **21**, 675–683.

Billy, F., Pineau, G., David, L., & Arghir, M. 2003. Experimental study of incompressible flow in grooved channels. *Pacific Symposium on Flow Visualization and Image Processing*, **10**, 1–6.

Boris, J.P., & Book, D.L. 1976. Solution of continuity equations by the method of flux-corrected transport. *Academic Press*, **16**, 85–129.

Boyd, R. D. 1985. Subcooled flow boiling critical heat flux (CHF) and its application to fusion energy components. Parts 1 & 2. *Fusion Technology*, **7**, 7–52.

Brown, N.M., & Lai, F.C. 2002. Combined heat and mass transfer in a horizontal channel with an open cavity. *8th AIAA/ASME Joint Thermophysics and Heat Transfer Conference Proceedings*, **2**, 8–15.

Bruneau, C-H., & Jouron, C. 1990. An efficient scheme for solving steady incompressible navier-stokes equations. *Journal of Computational Physics*, **89**, 389–413.

Burggraf, O.R. 1966. Analytical and numerical studies of the structure of steady separated flow. *Journal of Fluid Mechanics*, **24**, 113–134.

Cattadori, G., Gaspari, G.P., Celata, G.P., Cumo, M., Mariani, A., & Zummo, G. 1993a. Hypervapotron technique in subcooled flow boiling CHF. *Experimental Thermal and Fluid Science*, **7**, 230–240.

Cattadori, G., Gaspari, G.P., Celata, G.P., Cumo, M., Mariani, A., & Zummo, G. 1993b. Hypervapotron technique in subcooled flow boiling critical heat flux. *Experimental Thermal and Fluid Science*, **7**, 230–240.

Chang, J.L.C, & Kwak, D. 1984. On the method of pseduocompressibilty for numerically solving incompressible flows. *AIAA*, **84**, 252.

Chang, S.H., & Baek, W-P. 2003. Understanding, predicting and enhancing critical heat flux.

Chatellier, L., Laumonier, J., & Gervais, Y. 2004. Theoretical and experimental investigations of low mach number turbulent cavity flows. *Experiments in Fluids*, **36**, 728 – 740.

Chen, P., Newell, T. A., & Jones, B. G. 2008. Heat transfer characteristics in subcooled flow boiling hypervapotron. *Annals of Nuclear Energy*, **35**, 11591166.

Chen, P.H. 1996. Effect of the aspect ratio on the transient mass/heat transfer in an open cavity. *Journal of the Chinese Institute of Engineers*, **19**, 273–285.

Chorin, A.J. 1967. A numerical method for solving incompressible viscous flow problems. *Journal of Computational Physics*, **2**, 12–26.

Ciofalo, M., & Collins, M.W. 1992. Large-eddy simulation of turbulent flow and heat transfer in plane and rib-roughened channels. *International Journal of Numerical Methods in Fluids*, **15**, 453–489.

Cui, J., Patel, V.C., & Lin, C.L. 2003. Large-eddy simulation of turbulent flow in a channel with rib roughness. *International Journal of Heat and Fluid Flow*, **24**, 372–388.

Dahlgren, F., Wright, K., Kamperschroer, J., Grisham, L., Lontai, L., Peters, C., & VonHalle, A. 1994. TPX/TFTR neutral beam energy absorbers. *IEEE*, 455–461.

Deschamps, V. 1988. *Simulation numerique de la turbulence inhomogene incompressible dans un ecoulement de canal plan.* Ph.D. thesis, ONERA.

Deshpande, M.D., & Milton, S.G. 1998. Kolmogorov scales in a driven cavity. *Fluid Dynamics Research*, **22**, 359–381.

Deville, M., Le, T.H., & Morchoisne, Y. 1992. Numerical simulation of 3-D incompressible unsteady viscous laminar flows. *Notes on Numerical Fluid Mechanics*, **36**, 1–149.

Drikakis, D. 2003. Advances in turbulent flow computations using high-resolution methods. *Progress in Aerospace Sciences*, **39**, 405–424.

Drikakis, D., & Durst, F. 1994. Investigation of flux formulae in shock wave turbulent boundary layer interaction. *International Journal for Numerical Methods in Fluids*, **18**, 385–413.

Drikakis, D., & Rider, W. 2005. *High-resolution methods for incompressible and low-speed flows.* Computational Fluid and Solid Mechanics. Springer.

Drikakis, D., Govatsos, P.A., & Papantonis, D.E. 1994. A characteristic-based method for incompressible flows. *International Journal for Numerical Methods in Fluids*, **19**, 667–685.

Eiseman, P.R. 1979. *Journal of Computational Physics*, **33**, 118–150.

Engquist, B., & Osher, S. 1981. One-sided difference approximations for nonlinear conservation laws. *Mathematics of Computation*, **36**, 321–351.

Ezato, K., Suzuki, S., Sato, K., Taniguchi, M., Hanada, M., Araki, M., & Akiba, M. 2001. Critical heat flux test on saw-toothed fin duct under one-sided heating conditions. *Fusion Engineering and Design*, **56-57**, 291–295.

Falter, D.H., & Baxi, C. 1992. A model for analytical performance prediction of hypervapotron. *General Atomics (JET)*, August.

Falter, D.H., & Thompson, E. 1995. Performance of hypervapotron beam stopping elements at JET. *Fusion Technology*, **29**(July), 584–594.

Fureby, C., & Grinstein, F. 2002. Large eddy simulation of high Re number free and wall bounded flows. *Journal of Computational Physics*, **181**, 68–97.

Fureby, C., & Grinstein, F.F. 1999. Monotonically integrated large eddy simulation of free shear flows. *AIAA*, **37**, 544–557.

Fureby, C., & Tabor, G. 1997. Mathematical and physical constraints on large-eddy simulations. *Theoretical and Computational Fluid Dynamics*, **9**, 85–102.

Ghia, U., Ghia, K.N., & Shin, C.T. 1982. High-Re solutions for incompressible flow using the navier-stokes equations and a multigrid method. *Journal of Computational Physics*, **48**, 387–411.

Ghosal, S., & Moin, P. 1995. The basic equations for the large eddy simulation of turbulent flows in complex geometry. *Journal of Computational Physics*, **118**, 24–37.

Grinstein, F.F., & Fureby, C. 2004. From canonical to complex flows: Recent progress on monotonically integrated LES. *Computations in Science and Engineering*, **6**, 36–49.

Grinstein, F.F., Margolin, L.G., & Rider, W.J. 2007. *Implicit large eddy simulation: Computing turbulent fluid dynamics*. Cambridge University Press.

Habisreuting, M.A., Bouffanais, R., Leriche, E., & Deville, M.O. 2007. A coupled approximate deconvolution and dynamic mixed scale model for large-eddy simulation. *Journal of Computational Physics*, **224**, 241–266.

Hahn, M., & Drikakis, D. 2005. Implict large eddy simulation of turbulent flows using high resolution methods. *Proccedings of 43rd AIAA Aerospace Sciences Meeting and Exhibit, Reno, Nevada, Jan. 10-13, 2005* , 1–5.

Jordan, S.A., & Ragab, S.A. 1994a. A large-eddy simulation of the shear-driven cavity flow using dynamic modeling. *International Journal of Computational Fluid Dynamics*, **6**(4), 321–336.

Jordan, S.A., & Ragab, S.A. 1994b. On the unsteady and turbulent characterisitcs of the three-dimensional shear-driven cavity flow. *Journal of Fluids Engineering*, **116**, 439–449.

Kyung-Soo, Y. 2000. Large eddy simulation of turbulent flows in periodically grooved channel. *Journal of Wind Engineering and Industrial Aerodynamics*, **84**, 47–64.

Lenormand, E., & Sagaut, P. 2000. Subgrid-scale models for large-eddy simulations of compressible wall bounded flows. *AIAA*, **38**(8), 1340–1350.

Leong, J.C., & Lai, F.C. 1997. Mixed convection from a bottom heated open cavity in a horizontal channel. *AIAA 32nd Thermophysics Conference Proceedings*, 1997–2515.

Leriche, E. 2006. Direct numerical simulation in a lid-driven cavity at high reynolds number. *Conference on Turbulence and Interactions*.

Leriche, E., & Gavrilakis, S. 2000. Direct numerical simulation of the flow in a lid-driven cubical cavity. *Physics of Fluids*, **12**(6), 1363–1376.

Leschziner, M.A. 2000. Turbulence modelling for seperated flows with anisotropy-resolving closures. *Philosophical Transactions of the Royal Society of London*, **358**, 3247–3277.

Leschziner, M.A., & Drikakis, D. 2002. Turbulence and turbulent-flow computation in aeronautics. *The Aeronautical Journal*, **106**, 349–384.

Lohsz, M.M., Rambaud, P., & Benocci, C. 2005. Flow features in a fully developed ribbed duct flow as a result of LES. *Engineering Turbulence Modelling and Experimentation*, **6**, 267–276.

Manca, O., Pitzolu, R., Nardini, S., & Vafai, K. 2006. Experimental investigation on mixed convection in a channel with an open cavity below. *ASME summer heat transfer conference*, **19**(1), 53–68.

Margolin, L.G., & Rider, W.J. 2002. A rationale for implicit turbulence modelling. *International Journal of Numerical Methods*, **39**, 821.

Merkle, C.L., & Athavale, M. 1987. Time accurate unsteady incompressible flow algorithms based on atrifical compressibility. *AIAA*, **87-1137**.

Milnes, J., & Drikakis, D. 2009. Qualitative assessment of RANS models for hyper-vapotron flow and heat transfer. *Fusion Engineering and Design*, **84**, 1305–1312.

Milnes, J., Ciric, D., Fornera, M, Gee, S., Martin, D., Nightingale, M., & Sauerb, M. 2005. Hypervapotron design for the long pulse upgrades on MAST NBI. *MAST Technical Report*.

Miyake, Y., Tsujimoto, K., & Nakaji, M. 2001. Direct numerical simulation of rough-wall heat transfer in a turbulent channel flow. *International Journal of Heat and Fluid Flow*, **22**, 237–244.

Moin, P., & Kim, J. 1997. Tackling turbulence with supercomputers. *Scientific American*, **276**, 62–68.

Moser, R.D., Kim, J., & Mansour, N.N. 1999. Direct numerical simulation of turbulent channel flow up to Re=590. *Physics of Fluids*, **11**(4), 943–945.

Nightingale, M.P.S., Crawford, G.W., Gee, S.J., Hurford, D.J., Martin, D., Simmonds, M.R., Smith, R.T.C., Tsai, C.C., & Warder, S.E.V. 2001. The mast neutral beam injection system. *Fusion Engineering and Design*, **56-57**, 529–532.

O. Coceal, T.G. Thomas, I.P. Castro, & Belcher, S.E. 2006. Mean flow and turbulent statistics over groups of urban-like cubical obstacles. *Boundary layer meteorology*, **121**, 491–519.

Orszag, S.A. 1971. Accurate solution of the orr-somerfield stability equation. *Journal of Fluid Mechanics*, **50**, 689–703.

Özişik, N. M. 1985. *Heat Transfer - A basic approach.* McGraw-Hill, Inc.

Pascal-Ribot, S., Seiler-Marie, N., & Grandotto, M. 2005. First step in simulations of hypervapotron cooling concept for fusion applications. *The 11th International Topical Meeting on Nuclear Thermal-Hydraulics.*

Pascal-Ribot, S., Saroli, A. F., Grandotto, M., Spitz, P., & Escourbiac, F. 2007. First step in simulations of hypervapotron cooling concept for fusion applications. *Fusion Engineering and Design*, 1781–1785.

Patankar, S.V., Liu, C.H., & Sparrow, E.M. 1977a. Fully developed flow and heat transfer in ducts having streamwise-periodic variations of cross-sectional area. *Journal of Heat Transfer*, **99**, 180–186.

Patankar, S.V., Liu, C.H., & Sparrow, E.M. 1977b. The periodic thermally developed regime in ducts with streamwise periodic wall temperature or heat flux. *Journal of Heat and Mass Transfer*, **21**, 557–566.

Pope, S.B. 2000. *Turbulent flows*. Cambridge University Press.

Poujol, F.T. 2000. Natural convection of a high Prandtl number fluid in a cavity. *International Committee of Heat and Mass Transfer*, **27**, 109 – 118.

Prasad, A., & Koseff, J. 1996. Combined forced and natural convection heat transfer in a deep lid-driven cavity flow. *International Journal of Heat and Fluid Flow*, **17**, 460–467.

Prasad, A.K., & Koseff, J.R. 1989. Reynolds number and end-wall effects on a lid-driven cavity flow. *Physics of Fluids*, **1**, 208–218.

Ramanan, N., & Homsy, G.M. 1994. Linear stabilty of a lid-driven cavity flow. *Physics of Fluids*, **6**, 2690–2701.

Richards, R.F., Young, M.F., & Haiad, J.C. 1987. Turbulent forced convection heat transfer from a bottom heated surface cavity. *International Journal of Heat and Mass Transfer*, **30**, 2281–2287.

Roache, P.J. 1998. *Fundamentals of computational fluid dynamics*. Hermosa Publishers.

Roberts, G.O. 1971. *Lecture notes in physics*. 8 edn.

Roe, P. L. 1997. Approximate riemann solvers, parameter vectors and difference schemes. *Journal of Computational Physics*, **135**, 250–258.

Rohsenow, W. M., Hartnett, J.P., & Cho, Y.I. 1998. *Handbook of heat transfer*. McGraw-Hill.

Shapiro, E., & Drikakis, D. 2005. Artificial compressiblity, characteristics-based schemes for variable-density, incompressible, multispecies flows, Part 1. *Journal of Computational Physics*, **210**, 584–607.

Speth, E. 1989. Neutral beam heating of fusion plasmas. *Reports on Progress in Physics*, **52**, 57–121.

Stalio, E., & Nobile, E. 2003. Direct numerical simulation of heat transfer over riblets. *International Journal of Heat and Fluid Flow*, **24**, 356–371.

Tincani, A., Maio, P.A. Di, DellOrco, G., Ricapito, I., Riccardi, B., & Vella, G. 2008. Steady state and transient thermal-hydraulic characterization of full-scale ITER divertor plasma facing components. *Fusion Engineering and Design*, **83**, 1034–1037.

Tivey, R.B., Falter, H.D., Haange, R., Hemsworth, R.S., Massman, P., & Stabler, A. 1987. Testing of beam stopping elements using hypervapotron cooling. *JET and Atomic Fusion*, 1122–1125.

Toro, E. F. 1999. *Riemann solvers and numerical methods for fluid dynamics*. Springer-Verlag.

Toro, E. F., Spruce, M., & Speares, W. 2001. Restoration of the contact surface in the hll-riemann solver. *Shock Waves*, **4**, 25–34.

Vasilyev, O.V., Lund, T.S., & Moin, P. 1998. A general class of commutative filters for LES in complex geometries. *Journal of Computational Physics*, **146**, 82–104.

Ven, H. Van Der. 1995. A family of large eddy simulation filters with non-uniform filter widths. *Physics of Fluids*, **7**, 1171–1172.

Verstappen, R., Wissink, J.G., Cazemier, W., & Veldman, A.E.P. 1994. Direct numerical simulations of turbulent flow in a driven cavity. *Future Generation Computer Systems*, **10**(2-3), 345–350.

Wilcox, D. 1998. *Turbulence modelling for CFD.* D C W Industries.

Woodward, P.R. 1986. Piecewise-parabolic methods for astrophysical fluid dynamics. *Astrophysical Radiation Hydrodynamics*, 245–326.

Yao, H., Cooper, R.K., & Raghunthan, S.R. 2001. Large-eddy simulation of laminar to turbulent transition in incompressible flow past a 3-D rectangular cavity. *AIAA 31st Fluid Dynamics Conference and Exhibit Proceedings.*

Zang, Y., Street, R.L., & Koseff, J.R. 1993. A dynamic mixed subgrid-scale model and its application to turbulent recirculating flows. *Physics of Fluids*, **5**, 3186–3199.

Hypervapotron General Configurations

The two geometries used by the UKAEA are the Standard and MAST designs. Within this study only the Standard geometry is considered. However, various designs of Hypervapotrons exist, all involving different characteristic dimensions with regard the the cavity and channel design. All fins and channels are 3mm wide along the direction of the flow.

In Figure [A.1] a three dimensional schematic showing key the dimensions is presented. All geometric details to the Hypervapotrons were obtained from the UKAEA.

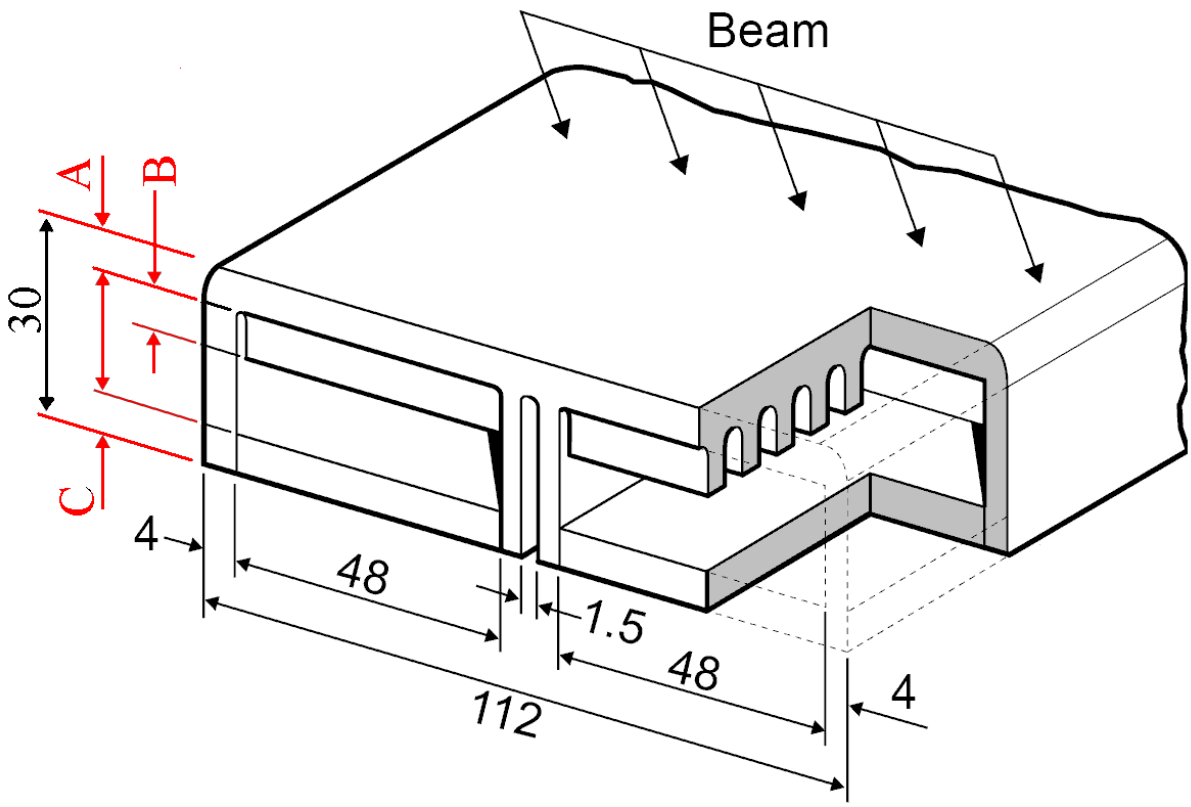

Figure A.1: Three dimensional Hypervapotron geometry schematic, image provided by the UKAEA.